Dissertation zur Erlangung des Doktorgrades

an der Fakultät für Chemie und Pharmazie

der Ludwig-Maximilians-Universität München

Targeting glutamine metabolism and mitochondria via natural compounds in cancer – novel therapeutic strategies

Florian Thomas Lengauer

aus München, Deutschland

2023

Erklärung

Diese Dissertation wurde im Sinne von §7 der Promotionsordnung vom 28. November 2011 von Frau Prof. Dr. Angelika M. Vollmar betreut.

Eidesstattliche Versicherung

Diese Dissertation wurde eigenständig und ohne unerlaubte Hilfe erarbeitet.

München, den 20.02.2023

F. Lengauer

(Florian Thomas Lengauer)

Dissertation eingereicht am:	23.02.2023
1. Gutachterin:	Prof. Dr. Angelika M. Vollmar
2. Gutachter:	Prof. Dr. Stefan Zahler
Mündliche Prüfung am:	03.04.2023

Meiner Familie

Table of contents

ABSTRACT

1 Abstract

Despite great efforts undertaken in investigating and establishing tumor therapies, cancer still represents one of the most prevalent causes of death worldwide. Natural products have traditionally emerged as a promising source of active biomolecules that contribute to the identification of drug candidates. Furthermore, due to their chemical diversity and high target specificity they display interesting tools in pharmaceutical research. Over the past decade targeting metabolic pathways is considered as auspicious strategy to address the increased reliance of cancer cells on specific nutrient fuels. Especially enhanced glutamine metabolism has been described for many different tumor entities, what makes glutaminolysis an interesting target in cancer medicine. Hence, glutamine deprivation has been intensively studied in recent research, however, with limited success caused by cellular adaption mechanisms. Addressing these adaptive processes together with concomitant glutamine deprivation is an interesting approach to enhance therapeutic effectiveness. Therefore, in this study we aimed to investigate novel therapeutic strategies to target glutamine metabolism and concomitantly levering the associated adaptive mechanisms. We showed that glutamine deprivation led to lysosomal acidification and induced pro-survival autophagy, which can be reversed by treatment with V-ATPase inhibitor Archazolid. Interestingly, a combination treatment of V-ATPase inhibition and glutamine deprivation did not lead to a synergistic effect in reducing proliferation and apoptosis induction. Elucidating the underlying mechanisms revealed that metabolic reprogramming mediated by SLC transporter family or glutamine metabolism related enzymes as well as the restoration of intracellular glutamine pool by accessing alternative fuel routes mediated by SLC38A7 does not account for the missing therapeutic benefit. Therefore, we analyzed other metabolic pathways and unraveled an increased glycolytic rate upon glutamine deprivation and concomitant V-ATPase inhibition, which further supported by an elevated glycolytic capacity as well as -reserve. Additionally, we found an elevated activity of the glycolytic enzyme hexokinase upon combination treatment. Thus, we revealed that inhibiting the V-ATPase prevents cellular adaption mechanisms triggered by glutamine deprivation. This study provides evidence of a metabolic shift of cancer cells towards glycolysis to evade growth inhibition and apoptosis induction upon combination therapy of V-ATPase inhibitor Archazolid and glutamine deprivation.

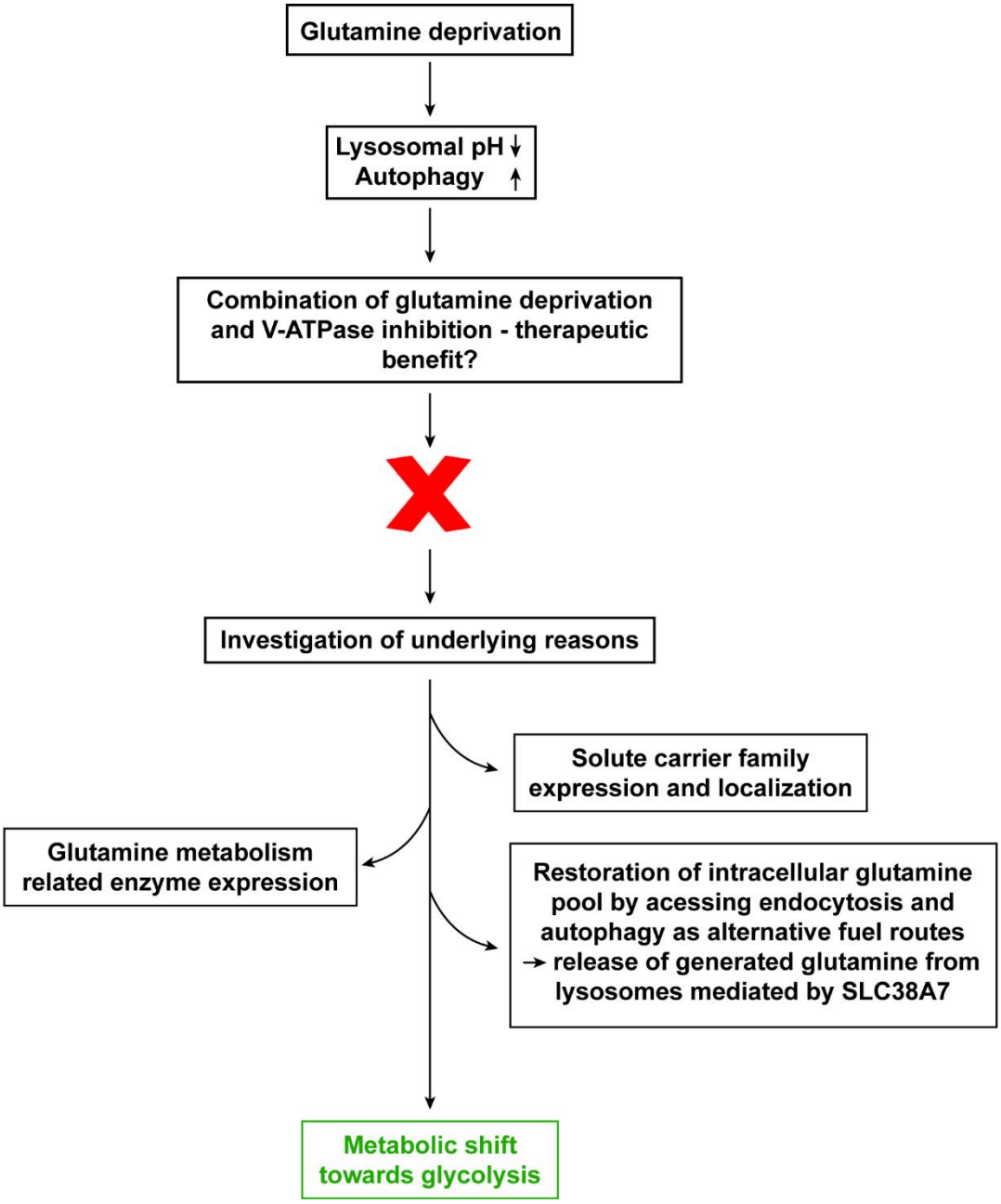

Figure 1: Targeting glutamine metabolism via V-ATPase inhibitor Archazolid – the project at a glance.

In the second part of this study, we investigated the potential of a novel compound derived from *Zephyranthes candida* named Zephycandidine A and its chemical analogs as anti-cancer drug precursors. Hence, we aimed to functionally characterize the parental structure and its analogs in the regard to growth inhibition and apoptosis induction. Thereby, we observed antiproliferative and cell death inducing properties of Zephycandidine A, which are even enhanced for hit analogs THK-99 and THK-121. Besides that, Zephycandidine A analogs displayed a broadened therapeutic window compared to its parental counterpart, implying cancer specificity. Since mitochondria are not merely involved in energy production but also play a crucial role in mediating cell death, we further unraveled the impact of Zephycandidine A and its analogs on mitochondria. We showed that Zephycandidine A and its related analogs trigger the intrinsic apoptotic pathway by affecting the mitochondria via abrogation of the mitochondrial membrane potential, generation of mitochondrial superoxides, increase of mitochondrial mass, and alterations in morphology. Therefore, this study provides evidence that Zephycandidine A displays an interesting chemical structure for drug development.

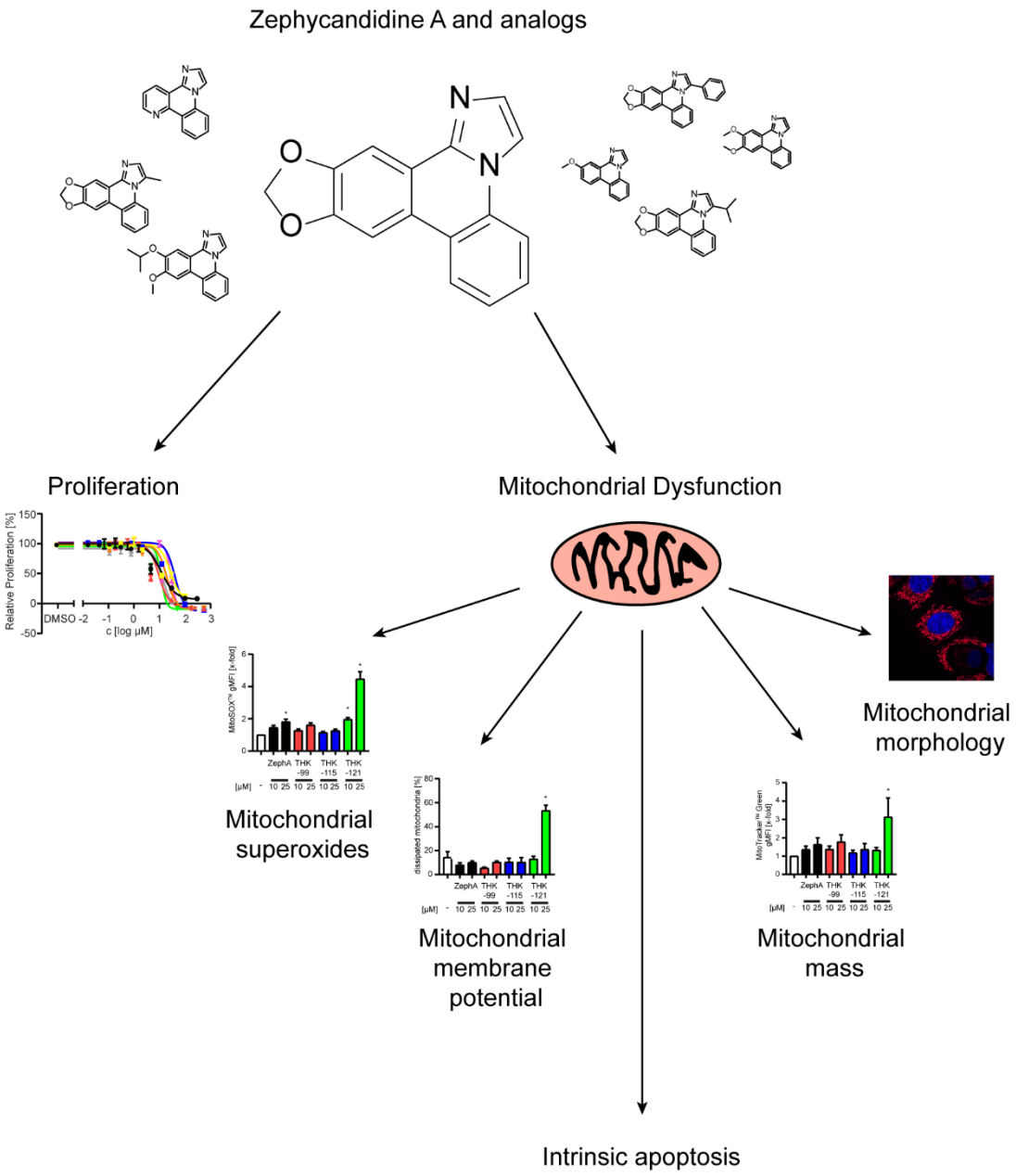

Figure 2: Zephycandidine A – the project at a glance.

INTRODUCTION

2 Introduction

2.1 Natural compounds – game changers in tumor medicine

2.1.1 The urgent need for therapeutic approaches in fighting cancer

Despite the ongoing covid-19 pandemic, which had claimed several millions of fatalities worldwide over the past three years, cancer-related mortality still represents one of the most frequent causes of death with almost 10 million death cases in 2020 [1]. Over the last decades, enormous efforts have been undertaken for early diagnosis, at best complete cure and especially treatment of cancer to fight the rising tumor burden. In this context, naturally occurring compounds with their exceptional diversity of bioactive molecules display an auspicious source for not only drug leads but also biological tools in the research area. Accordingly, about 50% of all approved drugs over the last four decades are natural products or have been developed on their basis [2], highlighting its great relevance and potential for drug development. Unlike synthetic and combinatoric libraries, natural product structures are characterized by high chemical diversity and biochemical specificity, which gives them ideal prerequisites for drug discovery. As a consequence of evolutionary pressure, natural products evolved as a population of privileged structures that interact selectively with a wide variety of proteins and other biological targets making them particularly precious not only for drug candidates but rather also as research tools [3]. Especially the outstandingly high target specificity compared to conventional combinatory chemical structures emphazises the enormous potential of natural products in tumor medicine and thus attributing to them the status as game changers in tumor medicine.

2.1.2 Plants and myxobacteria – accessible sources for natural products

Plants exist in every habitable environment on earth, on land as well as under water. Through selection pressure, plants have developed a multifaceted spectrum of molecules over time to effectively combat potential threats to their existence such as parasites and animals but also other competing plants [4]. Since the dawn of mankind, plants have been used intensively in naturopathic medicine to treat pathological states of both human and animals. These medicals are applied as mixtures, extracts, triturations and inhalants to name just a few, however, meanwhile more and more isolated active ingredients are finding their way into pharmaceutical applications. One of the first natural anti-tumor agents individually used in clinics is Paclitaxel, which is derived from *Taxus brevifolia* and

was first isolated and characterized in 1971 [5]. Paclitaxel is still used in chemotherapeutic medicine to treat several types of cancers today and thus, following the detailed investigation of the mode of action, illustrates a role model for plant-based compounds in tumor medicine.

Beyond plants, compounds isolated from myxobacteria also display an excellent source of natural products. Myxobacteria belong to the class of δ-proteobacteria (order *Myxococcales*) and are unicellular, rod-shaped, gram-negative soil-dwellers with habitats ranging from tundra to hot deserts and from acidic to alkaline environment preferably in places that are rich in microbial life and organic matter [6-8]. Untypically, myxobacteria move through a cellular motion known as gliding and are characterized by their species-explicit “social behaviour” through forming dynamic, multicellular fruiting bodies upon scare nutrient supply [9]. Since their secondary metabolites feature an outstandingly chemical diversity, biological activity and unique structure, metabolites from myxobacteria differ decisively from conventional compound libraries, which addresses them a special position not only as drugs in clinical aspects but also as pharmacological tools in research areas [10-12]. Accordingly, several derivates of the myxobacterial molecule Epothilone, which act in the exact same way as paclitaxel and presumably share a common binding site [13], have entered clinical trials as anti-cancer chemotherapeutic agents in a variety of cancer entities, with Ixabepilone reaching FDA approval in 2007 [14-18].

2.1.3 *Zephyranthes candida* – mother of Zephycandidine A

In 1990, Pettit et al. firstly described a cytostatic component in extracts of *Zephyranthes candida*, an amaryllidaceous bulbous herb that is native to South America and has been naturalized in the Asian region [19]. Meanwhile, several alkaloids have been isolated from whole plants of *Zephyranthes candida* and were evaluated for their anti-acetylcholinesterase (AChE) activity due to the previously described AChE inhibiting properties of amaryllidaceae alkaloids [20]. In 2012, 15 alkaloids were isolated from *Zephyranthes candida* with four of them exhibiting extraordinary cytotoxicity against several cancer cell lines [21]. Four years later, the same group re-collected plant material from the same plants and isolated an alkaloid with a rare imidazo[1,2-*f*]phenanthridine framework and named it Zephycandidine A (**Figure 3**) [22]. Furthermore, in this study the authors unveiled a significant cytotoxicity of Zephycandidine A against cancer cells accompanied by the induction of apoptosis, however, despite its promising anti-cancer potential the cellular mode of action still remains to be elucidated.

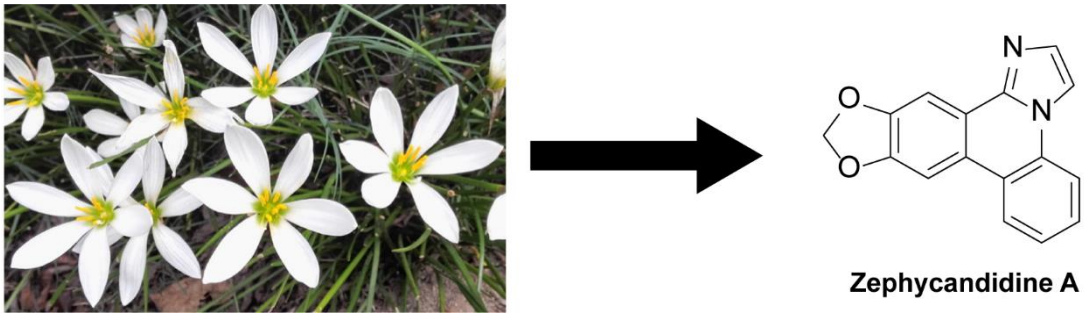

Figure 3: Chemical structure of Zephycandidine A.
Zephycandidine A was isolated from the plant *Zephyranthes candida*. The figure was adapted from Zhan et al. [23].

2.1.4 Archazolid A - a myxobacterial compound

Derived from the myxobacterial strains *Archangium gephyra* and *Cystobacter violaceus*, in 1993, Höfle et al. described a novel natural compound class of highly potent antiproliferative agents called Archazolids [24]. Its main structure is characterized by a 24-membered polyunsaturated macrolactone ring and a thiazole side chain terminating in a leucine-derived carbamate moiety [25]. Since Archazolids occur only in very small quantities in nature, the absolute necessity of sufficient quantities for research on the mechanism of action led to the first fully synthetic production of Archazolid A in 2007 (**Figure 4**) [26, 27]. Due to the very complex total synthesis, a modular synthesis was developed in 2009, which was accomplished by late-stage diversification of joint intermediates [28]. Already four years earlier, Sasse et al. identified the vacuolar-type H^+ ATPase (V-ATPase) as the molecular target of Archazolid [29]. Inhibition of the V-ATPase by Archazolid exhibits remarkable anti-cancer effects, which makes both – Archazolid and the V-ATPase - a promising anti-cancer drug and target, respectively [30-33].

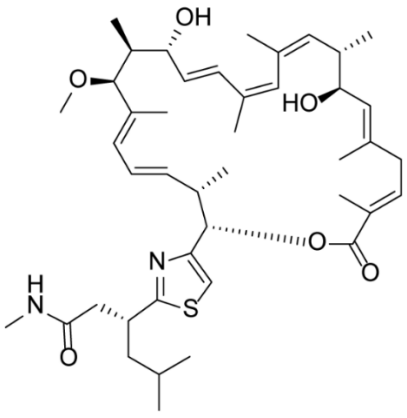

Figure 4: Chemical structure of Archazolid A.

2.2 The role of the V-ATPase in cancer and autophagy

2.2.1 Structure and physiological function of V-ATPases

V-ATPases are complex multi-subunit proton pumps mainly situated at cellular membranes of the endolysosomal system that primarily facilitate intraorganellar pH homeostasis via luminal acidification. V-ATPases are organized into two functional domains: a peripheral ATP-hydrolytic domain (V_1), which is located at the cytosolic site, and a proton-translocating domain (V_0) integrated into the membrane. While the V_1 domain is composed of eight subunits (A-H), the membrane-domain V_0 contains six subunits: a, c, c', c'', d and e (**Figure 5**). The two subunits A and B create the catalytic site for ATP hydrolysis leading to a rotation of a central stalk composed of subunits C-H that are attached to subunit d of domain V_0. Subunit d is coupled to circular c-subunits, which are proteolipid subunits that contain an essential glutamate residue, which undergoes reversible protonation during proton transport [34]. Following energy conversion, the V_0 domain moves in a rotatory fashion and bound protons can be released to the luminal side [35, 36]. This finally enables the fundamental property of an internal acidic pH (4.5-5.0) of endolysosomal vesicles that provides optimal working conditions for characteristic hydrolytic enzymes, which are the main players in the catabolic processing of biological substrates [37]. Of note, Archazolid inhibits the V-ATPase through binding to the equatorial region of its c-ring and thereby interrupts proton translocation [38].

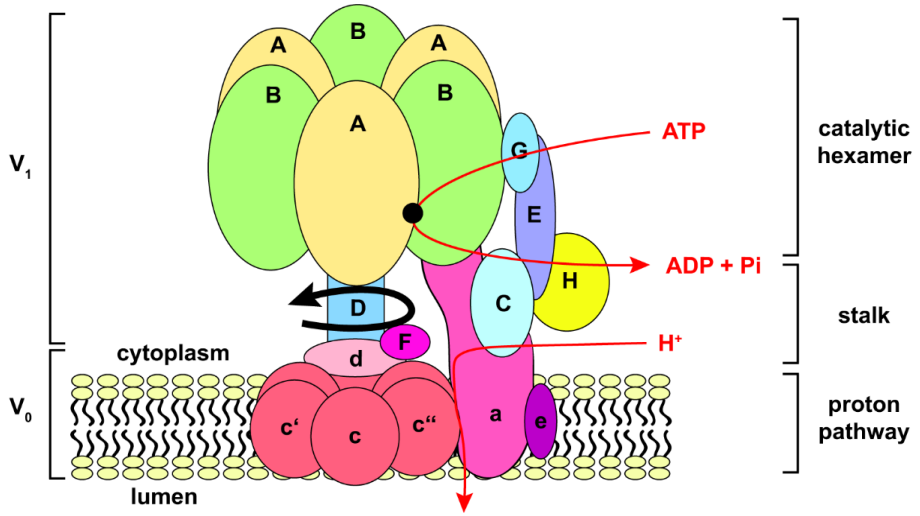

Figure 5: Schematic illustration of the V-ATPase with its subunits.
Schematic illustration of V-ATPase with its two domains: the peripheral V_1 domain, composed of 8 subunits (A-H) is responsible for ATP hydrolysis at the catalytic site (black dot) and the membrane V_0 domain consisting of subunits a, d, e, and 4 copies of c, enables proton release to the luminal side. Catalysis and proton transport is indicated with red arrows. Black arrow indicates the rotary direction of the V_0 domain. Illustration according to the model of Sub-Wada et al. [39].

2.2.2 V-ATPase in nutrient sensing and autophagy

Due to their function as proton pumps, V-ATPases are critically involved in essential physiological processes such as cellular nutrient sensing and the mediation of autophagy. In the regard to nutrient sensing, the V-ATPase is a part of the so-called lysosomal nutrient sensing (LYNUS) machinery (**Figure 6**). The LYNUS machinery is composed of several protein complexes, which interact with each other on the lysosomal surface, and mediates activation of the mechanistic target of rapamycin complex 1 (mTORC1) kinase signaling pathway in response to the nutrient availability in the extracellular environment [40, 41]. More precisely, the mTORC1 complex physically interacts with Rag GTPases and with the small GTPase RAS homolog enriched in brain (Rheb) [42, 43], which activate mTORC1 [44]. The activation and docking of Rag GTPases to the lysosomal membrane is regulated by a complex known as Ragulator [45], whose own activation in turn depends on the level of intralysosomal amino acids. The level of these amino acids is sensed through an inside-out mechanism that requires the V-ATPase, which conveys the amino acid-sensitive activation of Ragulator [46].

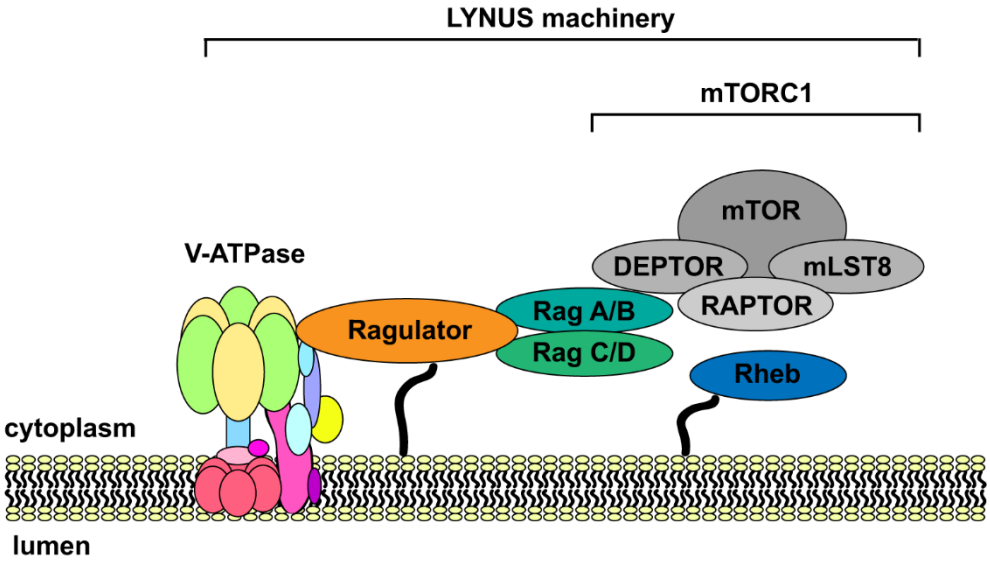

Figure 6: Schematic illustration of the LYNUS machinery.
The LYNUS machinery located at the lysosomal surface. It includes regulatory proteins associated with mTOR, such as RAPTOR (regulatory-associated protein of mTOR), mLST8 (mammalian lethal with SEC13 protein), and DEPTOR (DEP domain-containing mTOR-interacting protein) together with Rag GTPases (RagA/B and RagC/D), which activate mTORC1. Ragulator conveys activation and docking of Rag GTPases to the lysosomal membrane. The small GTPase Ras homolog enriched in brain (Rheb) is also involved in the growth factor-mediated activation of mTORC1. The V-ATPase facilitates amino acid sensing and mediates amino acid-sensitive interactions between Rag GTPases and Ragulator. Illustration according to Settembre et al. [40].

Emerging from this, sufficient nutrient supply facilitates mTORC1 activation followed by the direct phosphorylation of transcription factors such as S6 kinase 1 (S6K1) or eukaryotic translation initiation factor 4E (eIF4E), finally leading into the promotion of anabolic cellular processes for cell growth and proliferation [47, 48]. Especially in cancer, this signaling pathway plays a crucial role, since it is often over-activated not only by mutations or amplifications of mTOR itself but also through overexpression of other oncogenic drivers such as PI3K or Akt [49]. However, when amino acids in contrast are scarce in the cellular environment, mTORC1 becomes inactivated and thereby autophagy is induced due to the missing direct phosphorylation of factors and complexes that suppress autophagy [47]. The process of autophagy involves the degradation of cellular material by lysosomes, which allows basal turnover of cell components as well as the generation of energy and macromolecular building blocks. In principle, autophagic processes contribute to suppression of tumor formation via preservation of genomic instability, elimination of reactive oxygen species (ROS) and degradation of oncogenic proteins, among others. However, once cancer is already established, autophagy supports cancer progression by generating energy, adaption to cellular stress and supplying nutrients, especially amino acids [50], although persistent autophagy may eventually lead to cell death [51]. Thus, autophagy is a crucial cellular mechanism by which cancer cells adapt to environmental incidents and which essentially requires the function of the V-ATPase. Particularly, in response to autophagic stimuli, the V-ATPase gets activated and increases the capacity for rapid re-acidification following autophagosome-lysosome fusion, which enhances digestion rates and protein recycling by lysosomes after an elevated substrate influx derived from upregulated autophagy [52]. Consequently, through its participation in autophagic processes and amino acid sensing, the V-ATPase favors cellular homeostasis and is therefore able to enhance tumor cell survival. In turn, its inhibition results in dysfunctional autophagic signaling eventually leading to missing cellular adjustment to alterations in nutrient supply and finally to apoptosis.

2.3 Glutamine in cancer – metabolism and beyond

In the context of V-ATPase mediated amino acid sensing and subsequent mTOR activation, one specific amino acid appears again and again: glutamine. Glutamine is the most abundant amino acid in the human body with an about tenfold higher concentration compared to any other amino acid in both tissue and plasma [53]. Although glutamine belongs to the non-essential amino acids (NEAAs), which mammalian cells can synthesize endogenously no matter if they are cancerous or not, the exceptionally rapid proliferation

rate in tumor cells leads to the phenomenon that glutamine becomes “conditionally essential”. This means the capacity of endogenous synthesis does not meet the increased demands and glutamine needs to be obtained from external sources. In particular, the crucial role of glutamine in tumor-selective metabolic pathways created the widespread term “glutamine addiction” in cancer biology [54]. Given the excessive amount of glutamine required in many tumor entities for maintaining their intracellular glutamine pool, cancer cells frequently fall into a state where they utilize autophagy mediated through the inhibition of mTORC1 to obtain nutrients and energy. Vice versa, activation of mTORC1 by glutaminolysis explains why glutamine metabolism in tumor cells exceeds the requirement for glutamine as a biosynthetic precursor, emphasizing its outstanding position in cancer metabolism [55]. Glutamine is particularly important for tumor cells since it serves as a kind of “swiss army knife” by its extremely versatile contributions to various cancer favoring systems. Firstly, to ensure the maintenance of cancer growth, tumor cells require nucleotides and NEAAs during cell division. Glutamine is an obligate nitrogen donor for nucleotides and donates its amide group in three enzymatic steps in purine and two in pyrimidine synthesis, respectively (**Figure 7,** ①). Glutamine is then converted to glutamate, which transfers its amine group to α-ketoacids for generation of NEAAs (**Figure 7,** ③) [56, 57]. Additionally, glutamine is implicated in redox homeostasis. Due to the rapid proliferation rates, cancer cells typically undergo massive oxidative stress manifested by increased intracellular ROS levels, which can damage nucleotides, lipids and proteins [58]. To prevent damage of these macromolecules, cancer cells utilize glutathione as scavenger of ROS. Glutathione is a tripeptide consisting of glutamate, cystein and glycin, with glutamate being the rate-limiting factor for synthesis indicating its importance in redox homeostasis (**Figure 7,** ②) [59]. Moreover, glutamate indirectly regulates the uptake of cystine via SLC7A11 antiporter, which imports cystine in the exchange of glutamate [60]. Lastly, glutamine does not only act as a precursor for biosynthesis but also as mitochondrial substrate. Once imported to the inner mitochondrial space, glutamine is deamidated by the enzyme glutaminase (GLS) and forms glutamate, which then is converted to α-ketoglutarate by losing its amine group through either glutamate-oxaloacetate transaminase (GOT), glutamate-pyruvate transaminase (GPT) or glutamate dehydrogenase (GDH) (**Figure 7,** ④). Finally, α-ketoglutarate (α-KG) is fed into the tricarboxylic acid (TCA) cycle for facilitating anaplerosis [56]. Precisely, generated α-KG is implemented into the TCA-cycle and can be processed further via two ways: “clockwise” or “counterclockwise”. Glutamine derived α-KG provides a shortcut of the TCA cycle by replenishing its intramitochondrial pool and is then further metabolized in multiple

steps to malate in a “clockwise” manner. Interestingly, malic enzyme oxidatively decarboxylates malate and produces carbon dioxide, pyruvate and NADPH, the latter being then further utilized for redox balance. Additionally, through the “counterclockwise” mechanism of reductive carboxylation, α-KG replenishes the citrate pool that is required for lipid synthesis via the intermediate of acetyl-Coenzym A (acetyl-CoA) [61]. Summarized, glutamine contributes to tumor cells growth in multiple different ways. Together with the role in inducing autophagy upon its absence, targeting glutamine metabolism represents an attractive anti-tumor strategy.

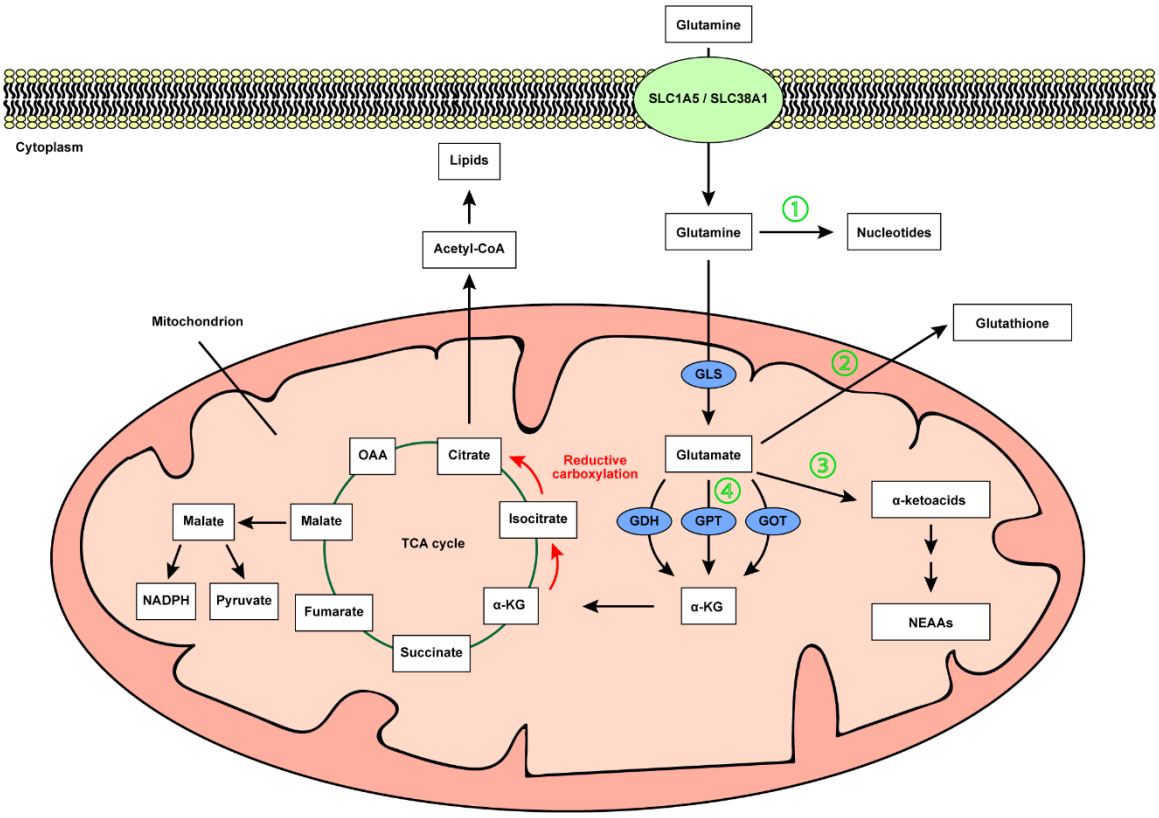

Figure 7: Schematic illustration of metabolism and major biosynthetic fates of glutamine.
Glutamine is imported across the cell membrane through transporters such as SLC1A5 or SLC38A1 [54]. Glutamine can either contribute to nucleotide biosynthesis (①) or is converted to glutamate by glutaminase (GLS). Metabolic fates of glutamate: ② it can contribute to the synthesis of glutathione. ③ It can transfer its amino group to α-ketoacids from which NEAAs are generated. ④ It can be converted to α-ketoglutarate (α-KG) through glutamate-oxaloacetate transaminase (GOT), glutamate-pyruvate transaminase (GPT) or glutamate dehydrogenase (GDH). Generated α-KG enters the tricarboxylic acid (TCA) cycle and can provide cellular energy in a shortcut manner. Malate exiting the TCA cycle can produce pyruvate and NADPH for reducing equivalents. Alternatively, α-KG can proceed backwards through the TCA cycle via reductive carboxylation to produce citrate, which supports synthesis of acetyl-CoA and lipids. Illustration according to Altman et al. [61].

2.4 Mitochondria - cell death mediators

In addition to their essential role as a hub for glutamine metabolism, mitochondria are involved in multiple physiological and pathological processes. They are not only the main players for ATP production due to harboring the respiratory chain but also implicated in ROS production and regulation of the intrinsic apoptotic pathway, which is governed by Bcl-2 (B-cell lymphoma 2) family members [62]. More precisely, apoptotic stimuli like DNA damage, excessive oxidative stress or lacking growth factors lead to an activation of B-cell lymphoma 2 (Bcl-2) homology 3 (BH3)-only proteins. These proteins again facilitate the recruitment of pro-apoptotic protein Bax (Bcl-2-associated X protein) or Bak (Bcl-2 homologous antagonist killer) to the mitochondrial outer membrane leading to its permeabilization (MOMP), a crucial process that is considered as the point of no return. Of note, anti-apoptotic Bcl-2 family members like Bcl-2, Bcl-xl or Mcl-1 (induced myeloid leukemia cell differentiation protein) prevent MOMP by binding to BH3-only proteins and inactivation of Bax or Bak, respectively. However, once MOMP is initiated, various proteins from the mitochondrial inner space are translocated to the cytosol, where they promote caspase activation finally leading to mitochondrial dysfunction and the execution of programmed cell death [63].

Furthermore, it is well documented that mitochondrial dysfunction also influences the mitochondrial network structure and it has been postulated that morphological changes act as an adaptive cellular response to mitochondrial stress [64]. Under normal conditions, mitochondria continually divide and fuse to form elongated tubules that build a dynamic interconnecting network. However, during apoptosis this network is disintegrated at the time of cytochrome *c* release and prior to caspase activation [65]. Along this line, upon mitochondrial dysfunction cells typically upregulate mitochondrial biogenesis as a compensatory mechanism to restore a functional mitochondria pool [66]. Therefore, investigation of mitochondrial network structure and mitochondrial mass displays an interesting approach to explore mitochondrial dysfunction as response to apoptotic stimuli. This evidently attributes mitochondria a key role in mediating intrinsic apoptosis making them highly interestingly objects of research.

2.5 Aim of the study

In this study, we aim to investigate novel therapeutic strategies by using natural compounds to effectively target glutamine metabolism and mitochondria, respectively.

Part I: Targeting glutamine metabolism via V-ATPase inhibition

In previous studies, our group already established V-ATPase inhibitor Archazolid as a high-potency and effective anti-tumor agent together with its mode of action [30, 31, 67]. In our most recent work, we observed an elevated glutamine dependency upon V-ATPase inhibition via Archazolid treatment in cancer cells providing the basis of the present study, in which we aimed to investigate the role of the V-ATPase in glutamine metabolism [68]. The overall aims of this study can be summarized as follows:

- Elucidation of the effects of glutamine deprivation and concomitant V-ATPase inhibition on nutrient sensing and autophagy, respectively
- Investigation of a potential therapeutic benefit of combining V-ATPase inhibition and glutamine deprivation
- Unraveling the underlying mechanisms

Part II: Zephycandidine A analogs as novel anti-cancer drugs

Zephycandidine displays a very interesting natural compound that has been described to exert anti-cancer activity together with tumor specific effects, which makes it a promising candidate for drug development. However, there is still room for improvement in terms of efficacy and tumor specificity, thus, Zephycandidine analogs were synthesized (Bracher Group, Ludwig-Maximilians-University, Munich, Germany). Additionally, the mode of action has not been unraveled yet, therefore we aimed to reveal underlying mechanisms of action to determine the potential of Zephycandidine A and its analogs as future anti-cancer drugs. The overall aims of this study can be summarized as follows:

- Identification of biologically active Zephycandidine A analogs
- Functional characterization of Zephycandidine A and analogs concerning proliferation and apoptosis induction
- Revealing the mechanism of cell death induction
- Analysis of the impact on mitochondria

MATERIALS AND METHODS

3 Materials and Methods

3.1 Materials

3.1.1 Compounds

Compound	Producer/source
2-Deoxy-D-glucose	Carl Roth GmbH, Karlsruhe, Germany
Archazolid A	Prof. Dr. Rolf Müller, Helmholtz-Institut Saarland
BPTES [bis-2-(5-phenylacetamido-1,3,4-thiadiazol-2-yl)ethyl sulfide]	Merck Millipore kGaA, Darmstadt, Germany
CB-839	Biomol GmbH, Hamburg, Germany
D-Glucose	Carl Roth GmbH, Karlsruhe, Germany
Elacridar	Selleck Chemical GmbH, Houston, USA
Oligomycin A	Merck Millipore kGaA, Darmstadt, Germany
THK compounds	Thomas Klaßmüller (Prof. Bracher, Ludwig-Maximilians-University Munich)
Verapamil	Selleck Chemical GmbH, Houston, USA

Table 1: Compounds

3.1.2 Consumables

Consumables	Producer/source
Cell culture flasks: 25 cm^2, 75 cm^2	Sarstedt AG & Co. KG, Nümbrecht, Germany
Cell culture plates and tubes	Sarstedt AG & Co. KG, Nümbrecht, Germany
Disposbale pipettes: 5 mL, 10 mL, 25 mL	Sarstedt AG & Co. KG, Nümbrecht, Germany
FACS tubes (5 mL)	Sarstedt AG & Co. KG, Nümbrecht, Germany
Falcon tubes: 15 mL, 50 mL	Sarstedt AG & Co. KG, Nümbrecht, Germany
ibiTreat µ-slides	Ibidi GmbH, Munich, Germany
Microtiter plates: 6 well, 24 well, 96 well	Sarstedt AG & Co. KG, Nümbrecht, Germany
Petri dishes: 100 mm, 40 mm	Sarstedt AG & Co. KG, Nümbrecht, Germany
Pipette tips: 10 µL, 100 µL, 1000 µL	Sarstedt AG & Co. KG, Nümbrecht, Germany

Table 2: Consumables

3.1.3 Reagents: Biochemicals, kits, dyes, and cell culture reagents

Reagent	Producer
5x siRNA buffer	Dharmacon™, GE Healthcare, Lafayette, USA
2,2,2 Trichlorethanol (TCE)	Merck Millipore kGaA, Darmstadt, Germany
Ammonium persulfate (APS)	Merck Millipore kGaA, Darmstadt, Germany
Amphotericin B	PAN Biotech GmbH, Aidenbach, Germany
Bovine serum albumin (BSA)	Merck Millipore kGaA, Darmstadt, Germany
Bradford reagent Roti® Quant	Bio-Rad Laboratories Inc., Hercules, USA
Calcein-AM	Biomol GmbH, Hamburg, Germany
CellTak™ cell and adhesive solution	Corning Inc., New York, USA
CellTiter-Blue® reagent	Promega Corporation, Fitchburg, USA
CellTiter-Glo® reagent	Promega Corporation, Fitchburg, USA
Collagen G	Matrix Bioscience GmbH, Mörlenbach, Germany
Complete™	Roche Holding AG, Basel, Switzerland
Coumaric acid	Merck Millipore kGaA, Darmstadt, Germany
Crystal violet	Carl Roth GmbH, Karlsruhe, Germany
DharmaFECT™ transfection reagent	Dharmacon™, GE Healthcare, Lafayette, USA
Dimethylsulfoxide (DMSO)	Merck Millipore kGaA, Darmstadt, Germany
Dithiothreitol (DTT)	Merck Millipore kGaA, Darmstadt, Germany
Dulbecco's Modified Eagle Medium (DMEM)	PAN Biotech GmbH, Aidenbach, Germany
Dulbecco's Modified Eagle Medium (DMEM) base	Merck Millipore kGaA, Darmstadt, Germany
Endothelial Cell Growth Medium (ECGM) kit enhanced	Pelobiotech GmbH, Martinsried
Ethylendiaminetetraacetic acid (EDTA)	Merck Millipore kGaA, Darmstadt, Germany
FACS Flow	Becton Dickinson GmbH, Heidelberg, Germany
FACS Shutdown solution	Becton Dickinson GmbH, Heidelberg, Germany
FACS Rinse	Becton Dickinson GmbH, Heidelberg, Germany
Fetal calf serum (FCS)	PAN Biotech GmbH, Aidenbach, Germany
FluorSave® reagent	Merck Millipore kGaA, Darmstadt, Germany
Glycerol	Carl Roth GmbH, Karlsruhe, Germany
β-Glycerophosphate	Carl Roth GmbH, Karlsruhe, Germany

Reagent	Producer
High-Capacity cDNA Reverse Transcription Kit	Applied Biosystems Corporation, Waltham, USA
Hoechst 33342	Merck Millipore kGaA, Darmstadt, Germany
Human recombinant insulin	Merck Millipore kGaA, Darmstadt, Germany
JC-1 (Tetraethylbenzimidazolylcarbocyanine iodide)	Thermo Fisher Scientific Inc., Waltham, USA
L-Glutamine	Merck Millipore kGaA, Darmstadt, Germany
L-Glutamic acid	Merck Millipore kGaA, Darmstadt, Germany
Luminol	AppliChem GmbH, Darmstadt, Germany
LysoTracker™ Green DND-26	Thermo Fisher Scientific Inc., Waltham, USA
Methanol	Thermo Fisher Scientific Inc., Waltham, USA
MitoTracker™ Green FM	Thermo Fisher Scientific Inc., Waltham, USA
MitoTracker™ Red CMXRos	Thermo Fisher Scientific Inc., Waltham, USA
MitoSOX™ Red mitochondrial superoxide indicator	Thermo Fisher Scientific Inc., Waltham, USA
Non-essential amino acids	PAN Biotech GmbH, Aidenbach, Germany
Page Ruler™ Prestained Protein Ladder	Thermo Fisher Scientific Inc., Waltham, USA
Paraformaldehyde	Thermo Fisher Scientific Inc., Waltham, USA
Phenylmethylsulfonyl fluoride (PMSF)	Merck Millipore kGaA, Darmstadt, Germany
Penicillin/Streptomycin 100x	PAN Biotech GmbH, Aidenbach, Germany
Rhodamine/PhalloidinRed	Thermo Fisher Scientific Inc., Waltham, USA
Polyacrylamide	Carl Roth GmbH, Karlsruhe, Germany
PowerUp™ SYBR® Green Master Mix	Applied Biosystems Corporation, Waltham, USA
Primers	Metabion GmbH, Planegg, Germany
Propidium iodide	Merck Millipore kGaA, Darmstadt, Germany
Pyronin Y	Merck Millipore kGaA, Darmstadt, Germany
Pyruvate	Merck Millipore kGaA, Darmstadt, Germany
RNeasy® Mini Kit (250)	QIAGEN GmbH, Hilden, Germany

Reagent	Producer
Roswell Park Memorial Institute Medium (RPMI-1640)	PAN Biotech GmbH, Aidenbach, Germany
Rotiphorese Gel 30	Carl Roth GmbH, Karlsruhe, Germany
Seahorse XFe96 FluxPaks	Agilent Technologies Inc., Santa Clara, USA
Seahorse XF base medium	Agilent Technologies Inc., Santa Clara, USA
Seahorse XF calibrant	Agilent Technologies Inc., Santa Clara, USA
Sodium chloride	Carl Roth GmbH, Karlsruhe, Germany
Sodium fluoride (NaF)	Merck Millipore kGaA, Darmstadt, Germany
Sodium orthovanadate (Na_3VO4)	Carl Roth GmbH, Karlsruhe, Germany
Sodium pyrophosphate (Na_4PO_7)	Carl Roth GmbH, Karlsruhe, Germany
Sodiumdodecylsulfate (SDS)	Carl Roth GmbH, Karlsruhe, Germany
Tetramethylethylendiamide (TEMED)	VWR International, Radnor, USA
Tris Base	Merck Millipore kGaA, Darmstadt, Germany
Triton X-100	Merck Millipore kGaA, Darmstadt, Germany
Trypsin	PAN Biotech GmbH, Aidenbach, Germany
Tween 20	Merck Millipore kGaA, Darmstadt, Germany

Table 3: Reagents

3.1.4 Technical equipment

Device	Producer
ChemiDoc™ Touch Imaging System	Bio-Rad Laboratories Inc., Hercules, USA
CYRIS® flox	INCYTON GmbH, Martinsried, Germany
Cytation 1 Multimode Reader	Agilent Technologies Inc., Santa Clara, USA
FACS Canto™ II	Becton Dickinson GmbH, Heidelberg, Germany
HeraCell incubator	Heraeus GmbH & Co. KG, Hanau, Germany
Leica TCS SP8 confocal laser scanning microscope	Leica Microsystems GmbH, Wetzlar, Germany
MicroAmp® Fast Optical 96-Well Reaction Plate, 0.1 mL	Applied Biosystems Corporation, Waltham, USA
MicroAmp® Optical Adhesive Film	Applied Biosystems Corporation, Waltham, USA
Millipore Express® PLUS membrane filter (0.22 µM)	Merck Millipore kGaA, Darmstadt, Germany
Mini PROTEAN 3 chamber	Bio-Rad Laboratories Inc., Hercules, USA
Nanodrop® Spectrophotometer	VWR International, Radnor, USA
Olympus CK30 inverted microscope	Olympus Life and Material Science GmbH, Tokyo, Japan
Orion II microplate Luminometer	Berthold Detection Systems GmbH, Pforzheim, Germany
Polyvinylidene difluoride (PVDF) membrane (0.2 µM)	Hybond-ECL™, Amersham Bioscience Europe GmbH, Freiburg, Germany
PowerPac HC, Tank Blotting System	Bio-Rad Laboratories Inc., Hercules, USA
Primus 25 advanced® Thermocycler	VWR International, Radnor, USA
QuantStudio™ 3 Real-Time PCR System	Thermo Fisher Scientific Inc., Waltham, USA
Seahorse XF^{e}96 Analyzer	Agilent Technologies Inc., Santa Clara, USA
SpectraFluor Plus™ Microplate Reader	Tecan AG, Männedorf, Switzerland
Vi-Cell™ XR	Beckmann Coulter Inc., Brea, USA

Table 4: Technical equipment

3.1.5 Software

Software	Producer
FACSDiva™ software	Becton Dickinson GmbH, Heidelberg, Germany
FlowJo 10.8.1	Becton Dickinson GmbH, Heidelberg, Germany
GraphPad Prism 8	GraphPad Software Inc., San Diego, USA
ImageJ	National Institutes of Health, Behtesda, USA
Image Lab 6.0	Bio-Rad Laboratories Inc., Hercules, USA
Leica LAS core X	Leica Microsystems GmbH, Wetzlar, Germany
Microsoft Office 2010	Microsoft Corporation, Redmond, USA
Seahorse Wave 2.6.1	Agilent Technologies Inc., Santa Clara, USA

Table 5: Software

3.2 Cell culture

3.2.1 Cell culture buffers and solutions

PBS (pH 7.4)	
NaCl	132.2 mM
Na_2HPO_4	10.4 mM
KH_2PO_4	3.2 mM
H_2O	

Trypsin/EDTA (T/E)	
Trypsin	0.05%
EDTA	0.02%
PBS	

PBS+Ca^{2+}/Mg^{2+} (pH 7.4)	
NaCl	137 mM
KCl	2.68 mM
Na_2HPO_4	8.10 mM
KH_2PO_4	1.47 mM
$MgCl_2$	0.25 mM
H_2O	

Growth medium	
DMEM/RPMI 1640	500 mL
FCS	50 mL

Freezing medium	
DMEM/RPMI-1640	70%
FCS	20%
DMSO	10%

Collagen G	
Collagen G	0.001%
PBS	

Table 6: Cell culture buffers and solutions

3.2.2 Cell lines

Cell line	Producer
BxPC-3	ATCC, Manassas, USA
CCRF-CEM	ATCC, Manassas, USA
HCT-15	ATCC, Manassas, USA
HeLa	DSMZ, Braunschweig, Germany
HL-60	DSMZ, Braunschweig, Germany
HUH7	ATCC, Manassas, USA
HUVEC	PromoCell GmbH, Heidelberg, Germany
Jurkat	DSMZ, Braunschweig, Germany
MCF-7	DSMZ, Braunschweig, Germany
MDA-MB-231	ATCC, Manassas, USA
Panc 03.27	ATCC, Manassas, USA
T24	DSMZ, Braunschweig, Germany

Table 7: Cell lines

HCT-15, BxPC-3, HeLa, HUH7, Panc 03.27, T24 and MDA-MB-231 cells were cultured in DMEM supplemented with fetal calf serum (FCS, 10%). CCRF-CEM and HL-60 cells were cultured in RPMI-1640 medium, supplemented with fetal calf serum (FCS, 10%). MCF-7 cells were grown in RPMI-1640 medium supplemented with 10% FCS, 1% pyruvate, 1% non-essential amino acids and 0.85 µM human insulin. Jurkat cells were grown in RPMI-1640 medium supplemented with 10% fetal calf serum (FCS) and 1% Pyruvate.

Human umbilical vein endothelial cells (HUVECs) were cultivated with ECGM kit enhanced supplemented with 10% FCS and 1% penicillin/streptomycin/amphotericin B. HUVECs were cultured for a maximum of six passages. All cells were cultured at 37 °C at constant humidity with 5% CO_2. Short tandem repeat (STR) analysis and testing for mycoplasma contamination was performed on a regular basis.

3.2.3 Passaging

When cells nearly reached confluency, they were split 1:2-1:10 and sub-cultured in 75 cm^2 culture flasks or seeded in multiwell plates or dishes for further experimental use. For passaging, culture medium was aspirated, cells were washed with pre-warmed PBS and detached by incubation with pre-warmed trypsin/ethylenediaminetetraacetic acid (EDTA) (T/E) solution for 3-5 min at 37 °C. Thereafter, culture medium was added to stop tryptic digestion and T/E solution was removed by centrifugation (600g, 5 min, 20 °C) followed by addition of new culture medium.

3.2.4 Freezing and thawing

Before freezing cells were cultured to reach confluency in a 75 cm^2 flask. Washing and cell detachment was conducted as described in **3.2.3**. After centrifugation (600g, 5 min, 20 °C), cells were re-suspended in ice-cold freezing medium and transferred into cryovials at a cell density of 3×10^6 cells per 1.5 mL aliquot. Following an initial storage at - 80 °C for at least 24 h, cryovials were transferred into liquid nitrogen tanks (- 196 °C) for long-term storage.
For thawing, the cryovial content was mixed with pre-warmed culture medium. After DMSO removal by centrifugation (600 g, 5 min, 20 °C), the cell pellet was re-suspended in culture medium and initially transferred into a 25 cm^2 flask for 24 h before cells were cultured in a 75 cm^2 flask.

3.2.5 Stimulation with compounds

Adherent cell lines were seeded the day before treatment to ensure complete attachment. Suspension cells were treated after 4 h incubation. DMSO stock solutions of test compounds were thawed and pre-diluted in complete growth medium. DMSO concentration did not exceed 0.1% (v/v) in all experiments.

3.2.6 Transfection with siRNA

For knockdown experiments, cells were transfected according to the DharmaFECT™ Transfection Reagents siRNA transfection protocol. Cells were seeded the day before transfection. siRNA (final concentration = 5 µM) and DharmaFECT 1 reagent were diluted in serum-free medium separately and incubated for 5 min at room temperature. The content of the two tubes was gently mixed by carefully pipetting up and down, incubated for 20 min at room temperature and subsequently transferred to the culture plate.

3.3 Flow Cytometry

For all experiments, cells were analyzed by flow cytometry using a FACSCanto™ II and FACSDiva™ software. For data evaluation the flow cytometry analysis software FlowJo 10.8.1 was employed.

3.3.1 Apoptosis assessment

70 × 10^3 cells per well (HCT-15, MCF-7, MDA-MB-231) or 100 × 10^3 cells per well (BxPC-3) were seeded into 24-well plates and incubated for 24 h at 37 °C. Treatment was performed at the indicated concentrations for 48 h. Subsequently, cells were detached and cell suspensions were transferred into pre-cooled FACS tubes. After that, cells were centrifuged for 5 min at 600 g at 4 °C, washed with an equal volume of ice-cold PBS, centrifuged again for 5 min at 600 g at 4 °C, and resuspended in 250 µL ice-cold hypotonic fluorochrome solution (**Table 8**). After 30 min incubation at 4 °C in the dark, cells were analyzed. Apoptosis was determined by propidium iodide staining as described before [69]. The fluorescence intensity indicates the DNA content. In apoptotic cells, DNA is fragmented, which leads to a relatively low fluorescence (subG1 population).

Hypotonic fluorochrome solution (HFS)	
Propidium iodide	50 µg/mL
Sodium citrate	0.1% (w/v)
Triton X-100	0.1% (v/v)
H_2O	

Table 8: Composition of hypotonic fluorochrome solution

3.3.2 Calcein-AM retention assay

Calcein-AM is a P-glycoprotein (P-gp) substrate and can be actively transported from the plasma membrane by P-gp. Once it has entered the cytosol, it is cleaved by cellular esterases and becomes fluorescent. Thus, calcein-AM can be used to monitor P-gp activity. The protocol was adapted from Robey and coworkers [70]. HCT-15 cells were seeded at a density of 120 × 10^3 cells per well into 24-well plates and incubated for 24 h at 37 °C. Subsequently, calcein-AM (200 nM) and the potential P-gp inhibitor BPTES were added (elacridar and verapamil served as positive controls) and incubated for 30 min at 37 °C. After incubation, cells were centrifuged for 5 min at 600 g at room temperature, washed with PBS and resuspended in 0.5 mL DMEM without phenol red containing the

respective concentration of the P-gp inhibitor. Following a 60 min incubation time at 37 °C, calcein-AM fluorescence was analyzed. Fluorescence intensities were normalized to the DMSO control.

3.3.3 Cell death assessment

125 × 10^3 cells per well (CCRF-CEM, HL-60, Jurkat) were seeded into 24-well plates and incubated for 4 h at 37 °C. Treatment was performed at the indicated concentrations for 48 h. Subsequently, cells were collected and cell suspensions were transferred into pre-cooled FACS tubes. After that, cells were centrifuged for 5 min at 600 g at 4 °C, washed with an equal volume of ice-cold PBS and centrifuged again for 5 min at 600 g at 4 °C. Then, cells were resuspended in 250 µL ice-cold PBS and analyzed. Dead cells were determined by forward versus sideward scatter (FSC vs. SSC) gating as described previously [71, 72] (**Figure 8**).

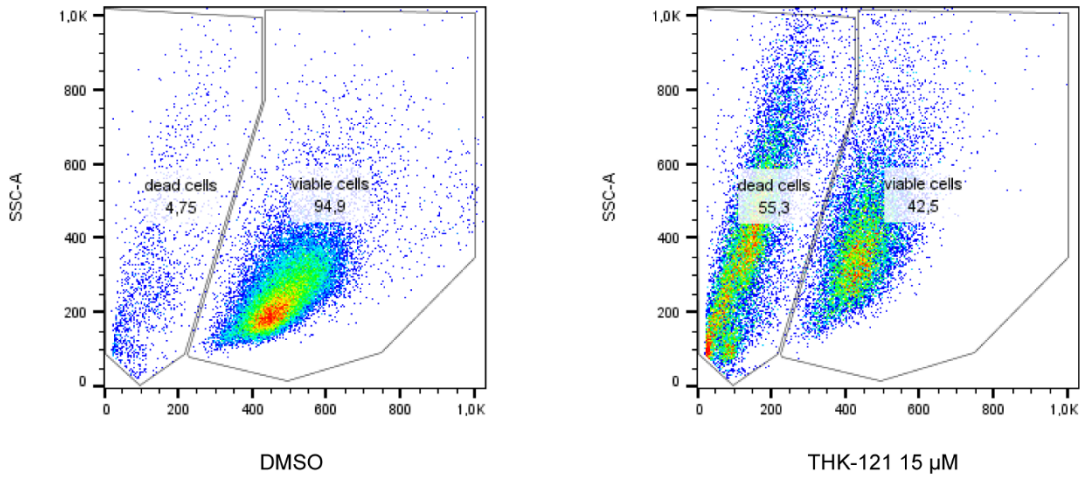

Figure 8: Gating of viable and dead cells using the forward versus sideward scatter (FSC vs. SSC) method.
Representative FSC vs. SSC dot plots of Jurkat cells with DMSO control versus THK-121 15 µM are shown.

3.3.4 Mitochondrial mass

To determine mitochondrial mass, Jurkat cells were seeded at a density of 250 × 10^3 cells per well into 24-well plates and incubated for 4 h at 37 °C. MCF-7 cells were seeded at a density of 125 × 10^3 cells per well into 24-well and incubated for 24 h at 37 °C. Cells were treated for 24 h at the indicated concentrations. Subsequently, cells were detached (if applicable), collected, washed with PBS and incubated with MitoTracker™ Green FM (100 nM) in RPMI-1640 medium without supplements for 30 min at 37 °C protected from light. Then, dye solution was discarded, cells were washed with PBS, followed by resuspending

in 250 µL PBS and analysis via flow cytometry. Forward versus side scatter (FSC vs SSC) gating was used to exclude cell debris using FlowJo 10.8.1. MitoTracker™ Green FM fluorescence was analyzed in the Alexa Fluor 488-A channel.

3.3.5 Mitochondrial membrane potential

JC-1 staining was used to determine the mitochondrial membrane potential (ΔΨm). Tetraethylbenzimidazolylcarbocyanine iodide (JC-1) is a cationic dye that accumulates in mitochondria. When mitochondrial membrane potential is intact, JC-1 aggregates in mitochondria, yielding a red fluorescence. Upon loss of mitochondrial membrane potential, the dye predominantly exists as a monomer in the cytosol emitting green fluorescence.

Jurkat cells were seeded at a density of 250 × 10^3 cells per well into 24-well plates and incubated for 4 h at 37 °C. MCF-7 cells were seeded at a density of 125 × 10^3 cells per well into 24-well and incubated for 24 h at 37 °C. Cells were treated for 24 h at the indicated concentrations. Subsequently, cells were detached (if applicable), collected, washed with PBS and incubated with 250 µL JC-1 (1 µg/mL) in medium for 30 min at 37 °C protected from light. Simultaneously, compensation samples were prepared using Anti-Mouse Ig, κ/Negative Control (FCS) Compensation Particles Set (Becton Dickinson GmbH, Heidelberg, Germany) and a PE Mouse IgG1, κ/Isotype Control (#555749; Becton Dickinson GmbH, Heidelberg, Germany) and a BD Alexa Fluor® 488 Mouse IgG1 κ Isotype Control (#557721; Becton Dickinson GmbH, Heidelberg, Germany) as described by the manufacturer. Prior to analysis of cellular samples, compensation of spectral overlap was performed. The percentage of Alexa-Fluor-488-A positive populations was determined as shown in **Figure 9**.

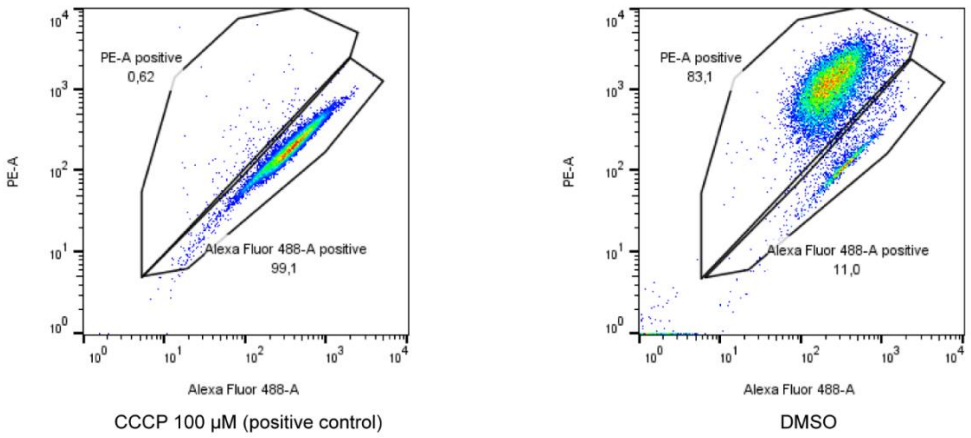

Figure 9: Gating for PE-A positive and Alexa-Fluor-488-A positive populations after staining with JC-1.

3.3.6 Mitochondrial Superoxide

Jurkat cells were seeded at a density of 250 × 10^3 cells per well into 24-well plates and incubated for 4 h at 37 °C. MCF-7 cells were seeded at a density of 125 × 10^3 cells per well into 24-well and incubated for 24 h at 37 °C. Cells were treated for 24 h at the indicated concentrations. Subsequently, cells were detached (if applicable), collected, washed with PBS and incubated with 250µL MitoSOX™ Red Superoxide Indicator (5 µM) in Hank´s balanced salt solution (HBSS) (**Table 9**) for 30 min at 37 °C protected from light. Then, dye solution was discarded, cells were washed with PBS, followed by resuspending in 250 µL PBS and analysis via flow cytometry. MitoSOX™ Red Superoxide Indicator fluorescence was analyzed in the PE-A channel.

Hank´s balanced salt solution (HBSS)	
$CaCl_2$	1.26 mM
D-glucose	5.56 mM
KCl	5.33 mM
KH_2PO_4	0.44 mM
$MgCl_2$ x 6 H_2O	0.49 mM
$MgSO_4$ x 7 H_2O	0.41 mM
NaCl	137.9 mM
$NaHCO_3$	4.17 mM
Na_2HPO_4	0.34 mM
H_2O	

Table 9: Composition of Hank´s balanced salt solution

3.4 Proliferation assays

3.4.1 CellTiter-Blue® cell viability assay

5.0×10^3 cells per well (MCF-7, MDA-MB-231) or 2.5×10^3 cells per well (HUVEC) were seeded into 96-well plates and incubated for 24 h at 37 °C. 20×10^3 cells per well (Jurkat, HL-60, CCRF-CEM) were seeded into 96-well plates and incubated for 4 h at 37 °C. Treatment was performed at the indicated concentrations for 72 h. Initial metabolic activity was determined 2 h after seeding and used as zero value for all cell lines. 2 h before the end of stimulation time, 20 µL CellTiter-Blue® reagent was added to each well and fluorescence at 550 nm was detected with a Tecan SpectraFluor Plus™ microplate reader. Proliferation [%] was determined relative to DMSO control. Half-maximal inhibitory concentrations (IC_{50}-values) were calculated by nonlinear regression using GraphPad Prism 8.2.1 software.

3.4.2 Crystal violet proliferation assay

3.0×10^3 cells per well (HCT-15) or 5.0×10^3 cells per well (BxPC-3) were seeded into 96-well plates and incubated for 24 h at 37 °C. Treatment was performed at the indicated concentrations for 72 h. Subsequently, cells were stained with crystal violet/methanol solution (**Table 10**) for 10 min, washed with distilled water and dried, before crystal violet was re-dissolved in sodium citrate solution (**Table 11**) for 10 min. Absorbance was measured at 550 nm using the Tecan SpectraFluor Plus™ microplate reader. Proliferation [%] was determined relative to DMSO control. Half-maximal inhibitory concentrations (IC_{50}-values) were calculated by nonlinear regression using GraphPad Prism 8.2.1 software.

Crystal violet solution	
Crystal violet	0.5% (w/v)
Methanol	50% (v/v)
H_2O	

Table 10: Crystal violet solution

Sodium citrate solution	
Sodium citrate	0.1 M
Ethanol	50% (v/v)
H_2O	

Table 11: Sodium citrate solution

3.5 Western blot analysis

3.5.1 Cell lysis

Cellular protein levels were analyzed by Western blot. For lysis of adherent cell types, medium was removed and cells were washed with ice-cold PBS before adding RIPA lysis buffer (Fehler! Verweisquelle konnte nicht gefunden werden.). Subsequently, cells were scraped off with a cell scraper and transferred into Eppendorf tubes. Suspensions cells were collected, centrifuged (600 g, 5min, 4 °C), washed with ice-cold PBS and resuspended in RIPA lysis buffer.

Then, cell lysates were frozen for at least 30 minutes at -80 °C, followed by thawing at 4 °C under gentle agitation. In order to remove cell debris, lysates were centrifuged (6.000 g, 15 min, 4 °C), followed by storage at -20 °C, if not immediately processed further.

RIPA lysis buffer	
NaCl	150 mM
Nonidet NP-40	1% (w/v)
Tris/HCl	50 mM
SDS	0.10% (w/v)
Sodium deoxycholate	0.25% (w/v)
H_2O	
added before use:	
Complete®EDTAfree	4 mM
NaF	1 mM
$Na_4P_2O_7$	1 mM
Na_3VO_4	2 mM
PMSF	0.5 mM
ß-Glycerophosphate	1 mM

Table 12: RIPA lysis buffer

3.5.2 Protein quantification and sample preparation

To ensure equal protein loading, protein concentration was determined via Bradford assay as described previously [73]. In detail, 5 µL of cell lysate were diluted in water 1:5 (v/v) and 10 µL of the prepared dilution were transferred to a 96-well plate in triplicates. Concomitantly, bovine serum albumin (BSA) standards (0-500 µg/mL) were transferred to the 96-well plate. Bradford reagent was diluted 1:5 (v/v) in water and added to the samples (190 µL/well), followed by incubation for 5 min at room temperature under gentle agitation.

Bradford assay is an addition of coomassie brilliant blue G-250 to protein solution. The coomassie blue dye associates with basic and aromatic amino acids, thereby causing a shift in absorbance during protein determination. Absorbance of each sample at 592 nm was determined by photometric measurement using a Tecan SpectraFluor Plus™ microplate reader and linear regression was conducted with BSA dilutions as protein standards. Subsequently 5x SDS sample buffer (**Table 13**) was added to the samples and protein concentration was adjusted by adding 1x SDS sample buffer. Afterwards the samples were heated at 95 °C for 5 min and stored at -20 °C before gel electrophoresis.

5x SDS sample buffer	
DTT	2% (w/v)
Glycerol	50% (v/v)
Pyronin Y	0.025% (w/v)
SDS	5% (w/v)
Tris/HCl pH 6.8	3.125 M
H_2O	

Table 13: 5x SDS Sample Buffer

3.5.3 SDS-PAGE and tankblotting

For separation of proteins, discontinuous SDS-polyacrylamide gel electrophoresis (SDS-PAGE) was performed. Equal amounts of protein samples were loaded on discontinuous polyacrylamide gels, consisting of a gradient separation (4-20%) and a stacking gel. The Mini Protean 3 system chamber from Bio-Rad was filled with electrophoresis buffer, followed by electrophoresis at a current of 100 V for 21 min and at 200 V for 45 min for protein stacking and separation, respectively. To determine the molecular weight of detected proteins, a pre-stained protein ladder PageRuler Plus™ was subjected to gel electrophoresis in parallel.

Separation Gel (4-20%)	
APS	0.05% (w/v)
Rotiphorese™ Gel 30	40-80% (v/v)
SDS	0.1% (w/v)
TCE	0.5% (w/v)
TEMED	0.1% (v/v)
Tris-HCl (pH 8.8)	375 mM
H_2O	

Stacking Gel	
APS	0.1% (w/v)
Rotiphorese™ Gel 30	17% (v/v)
SDS	0.1% (w/v)
Tris-HCl (pH 6.8)	125 mM
TEMED	0.2% (v/v)
H_2O	

Electrophoresis buffer	
Glycine	38 mM
SDS	0.1% (w/v)
Tris	4.9 mM
H_2O	

Table 14: Buffers and gel mixtures for gel electrophoresis

Prior to tank blotting, protein load was determined by stainfree detection of trichloroethanol (TCE) supplemented gels using the ChemiDoc Touch Imaging System. Subsequently, proteins were transferred onto a PVDF membrane by tank blotting. PVDF membranes were equilibrated in tank buffer (**Table 15**) for 1 min before a blotting sandwich (fiber pad – blotting paper – separation gel – PVDF membrane – blotting paper – fiber pad) was prepared and put into the Mini Trans-Blot® system that was subsequently filled with tank buffer. Proteins were transferred at 4 °C utilizing a constant current of 100 V for 90 min.

Tank buffer	
Glycine	39 mM
Methanol	20% (v/v)
Tris base	48 mM
H_2O	

Table 15: Tank buffer

3.5.4 Protein detection

After tankblotting, membranes were blocked with a 5% (w/v) solution of BSA in PBS for 2 h at room temperature to avoid unspecific binding of primary antibodies. Subsequently, membranes were incubated with primary antibody solution (**Table 16**) at 4 °C under gentle agitation overnight. Primary antibodies were diluted 1:1000 (v/v) in 1% (w/v) BSA in PBS. On the next day, membranes were washed three times with TBS-T (Tris-buffered saline + Tween 20) (**Table 18**) and incubated with an appropriate HRP-linked secondary antibody [1:3000 in 1% (w/v) BSA in PBS] (**Table 17**) for 2 h at room temperature. After additional three washing steps with TBS-T, enhanced chemiluminescence (ECL) imaging was used to detect antibody signals on membranes. In detail, proteins were detected by HRP-linked oxidation of luminol and chemiluminescence detection by incubating membranes for 1 min in ECL solution (**Table 19**) and developing membranes directly on the ChemiDoc Touch imaging system. Further data evaluation was performed with Image Lab software.

Antigen	Product nr.	Provider
AMPKα	2793	Cell Signaling Technology Inc. (Danvers, USA)
AMPKα phospho (Thr172)	2535	Cell Signaling Technology Inc. (Danvers, USA)
GAPDH	5174	Cell Signaling Technology Inc. (Danvers, USA)
Hexokinase I	2024	Cell Signaling Technology Inc. (Danvers, USA)
Hexokinase II	2867	Cell Signaling Technology Inc. (Danvers, USA)
LC-3 I & II	4108	Cell Signaling Technology Inc. (Danvers, USA)
LDHA	3582	Cell Signaling Technology Inc. (Danvers, USA)
SLC1A5	8057	Cell Signaling Technology Inc. (Danvers, USA)
SLC38A1	MABN502	Merck Millipore kGaA (Darmstadt, Germany)
P70S6K	9202	Cell Signaling Technology Inc. (Danvers, USA)
P70S6K phospho (Thr389)	9205	Cell Signaling Technology Inc. (Danvers, USA)
P62	8025	Cell Signaling Technology Inc. (Danvers, USA)
PFKP	8164	Cell Signaling Technology Inc. (Danvers, USA)
PKM1/2	3190	Cell Signaling Technology Inc. (Danvers, USA)
PKM2	4053	Cell Signaling Technology Inc. (Danvers, USA)
Pyruvate Dehydrogenase	3205	Cell Signaling Technology Inc. (Danvers, USA)

Table 16: Primary antibodies for Western blot analysis

Antigen	Product nr.	Provider
HRP, Goat-Anti-Mouse IgG2b	1090-05	Southern Biotech Assoc. (Birmingham, USA)
HRP, Goat-Anti-Rabbit IgG (H+L)	172-1019	Bio-Rad Laboratories Inc. (Hercules, USA)

Table 17: Secondary antibodies for Western blot analysis

TBS-T (pH 7.6)	
Glycine	190 mM
Tris-base (pH 8.0)	24.8 mM
Tween 20	0.1% (v/v)
H_2O	

Table 18: TBS-T washing buffer

ECL solution	
Coumaric acid	1 mM
H_2O_2	17 µM
Luminol	2.5 mM
Tris (pH 8.5)	100 mM
H_2O	

Table 19: ECL solution

3.6 Confocal Imaging

Confocal images were acquired utilizing a Leica TCS SP8 confocal laser scanning microscope equipped with an HC PL APO CS2 63x/1.4 oil objective and photomultiplier (PMT) or HyD detectors and Las X core software. Following excitation laser lines were applied: 405 nm, 488 nm and 647 nm.

3.6.1 SLC38A1 & SLC1A5 localization

HCT-15 cells were seeded at a density of 15 × 10^3 cells per well into ibiTreat 8-well µ-slides and incubated for 24 h at 37 °C. Cells were treated as indicated for 24 h, washed with PBS, fixed for 10 min with 4% methanol-free paraformaldehyde in PBS followed by permeabilization with 0.5% Triton-X for 10 min. Unspecific binding sites were blocked with 5% BSA in PBS for 1 h. Primary antibodies (**Table 20**) were applied for 2 h at room temperature, followed by 3x washing with 1% BSA in PBS. Appropriate secondary antibodies (**Table 21**) were incubated for 1 h at room temperature in the dark together with Hoechst 33342 (2.5 µg/mL) and Rhodamine/PhalloidinRed. Cells were again washed with

PBS and sealed with FluorSave™ mounting medium before imaging. Brightness and contrast were adjusted to improve visibility.

Antigen	Product nr.	Provider
SLC1A5	8057	Cell Signaling Technology Inc. (Danvers, USA)
SLC38A1	MABN502	Merck Millipore kGaA (Darmstadt, Germany)

Table 20: Primary antibodies for confocal imaging

Antigen	Product nr.	Provider
Goat-anti-mouse IgG (H+L) Alexa-Fluor™ 488	A-11001	Thermo Fisher Scientific Inc., Waltham, USA
Goat-anti-rabbit IgG (H+L) Alexa-Fluor™ 647	A-21245	Thermo Fisher Scientific Inc., Waltham, USA

Table 21: Secondary antibodies for confocal imaging

3.6.2 FITC Dextran staining

For indirect measurement of lysosomal pH via pH sensitive quenching of FITC-dextran fluorescence, 7.5×10^3 cells per well (HCT-15) and 15×10^3 cells per well (BxPC-3) were seeded into ibiTreat 8-well µ-slides and incubated for 24 h at 37 °C. Cells were loaded with 200 µg/mL of FITC-dextran 20 kDa for 24 h, followed by treatment at the indicated concentrations for 1 h before staining with Hoechst 33342 (2.5 µg/mL) (nuclei, blue). Subsequently, cells were washed with PBS and respective medium was added before imaging. Analysis of FITC fluorescence intensity was performed in the cell areas using ImageJ.

3.6.3 Mitochondrial morphology

MCF-7 cells were seeded at a density of 20×10^3 cells per well into ibiTreat 8-well µ-slides and incubated for 24 h at 37 °C. After 24 h of stimulation as indicated, cells were washed with PBS twice, followed by staining with 100 nM of MitoTracker™ Red CMXRos and Hoechst 33342 (2.5 µg/mL) for 30 min at 37 °C protected from light. For quantitative analysis of the mitochondrial network, the MiNA analysis plugin in ImageJ was used. This tool and documentation regarding its usage are available at https://github.com/StuartLab/MiNA. Before running the macro, images were converted to 8-bit. Briefly, the macro MiNA allowed pre-processing of the image to enhance image quality prior to analysis to provide more accurate results (median filter: radius = 1, unsharp

mask: radius (sigma) = 5, mask weight = 0.5). Then, the tool skeletonized the mitochondrial network and calculated the mean branch length (length of each single mitochondrion), the mean branches per network (extent of mitochondrial branching per network) and the mean summed branches length (size of each individual network). Furthermore, an image with an overlay of the binarized mitochondria and the skeletal model was generated. Each Pixel of the skeleton is classified, whereby green pixels represent the length of the mitochondria, blue pixels the connection sites between two mitochondria and yellow pixels the end of a network structure, respectively. In addition, before skeletonizing the area of the image occupied by the mitochondrial signal was analyzed, which is depicted as a purple outline.

3.7 Metabolic profiling

3.7.1 Purpose and measurement principle

In order to investigate differences in glycolysis in HCT-15 cells, a glycolysis stress test was performed with a Seahorse XFe96 device as well as a metabolic stress test with a CYRIS® flox in cooperation with INCYTON® GmbH (Martinsried, Germany).

Both analyzers measure two parameters, Extracellular Acidification Rate (ECAR) in mpH/min and Oxygen Consumption Rate (OCR) in pmol/min, simultaneously in real-time utilizing dual-florescent biosensors for protons and molecular oxygen. For metabolic profiling assessed via glycolysis stress test, cells are glucose-starved first in assay medium without glucose and pyruvate for 1 h. As first injection, a saturating concentration of glucose is injected. Secondly, oligomycin, which inhibits F_1F_0-ATP synthase and thereby impairs mitochondrial ATP production, is injected and forces the cells to shift their energy production towards glycolysis in order to maintain ATP production and thereby energy homeostasis. Thirdly, the hexokinase II inhibitor 2-deoxy-D-glucose (2-DG) is injected to reveal that the increased ECAR was caused by glycolysis and not by other biochemical processes.

Regarding metabolic stress test assessed via CYRIS® flox, cells are equilibrated in measure medium (**Table 22**) containing glucose, loaded into the instrument immediately followed by starting the run. As first injection, oligomycin is injected by an automated fluidic robotic system, followed by 2-DG injection.

In order to compare metabolic activities, a normalization based on cell number has to be conducted as ECAR and OCR reflect both metabolic activity and total cell number.

Measure medium metabolic stress test (pH 7.2, 37 °C)	
Dulbecco's Modified Eagle Medium (DMEM) base powder	1 vial
D-Glucose	4.5 g/mL
FCS	10% (v/v)
L-Glutamine	4 mM

Table 22: Assay medium metabolic stress test

3.7.2 Seahorse XFe96

An overview of the glycolysis stress test, the injected substances and the analyzed parameters is given in **Figure 10**.

3.7.2.1 Hydration of the Seahorse XFe96 sensor cartridge

Each well of the utility plate (Agilent Technologies) was filled with 200 µL sterile H_2O and the sensors of the Seahorse XF^{e}96 cartridge (Agilent Technologies) were submerged into the H_2O. The plate was placed in a non-CO_2 incubator overnight together with an aliquot (20-50 mL) of XF Calibrant (Agilent Technologies). On the next day, H_2O was replaced by XF Calibrant, followed by 45-60 min of incubation in a non-CO_2 incubator prior to the assay.

3.7.2.2 Coating of the Seahorse XFe96 microplate

Each well of the XFe96 microplate was filled with 25 µL of Cell-Tak^{TM} cell and tissue adhesive solution (22.4 µg/mL), followed by 20 min of incubation at room temperature. After incubation, coating solution was discarded and the wells were rinsed twice with sterile H_2O (100 µL per well). The XFe96 microplate was subsequently dried for 2 hours in the laminar flow hood prior to seeding of cells.

3.7.2.3 Seeding and treatment of cells in the XF^{e}96 microplate

HCT-15 cells were seeded at a density of 20×10^3 cells per well into the XFe96 microplate plate and allowed to adhere overnight. Cells were pre-treated for 24 h as indicated prior to the assay.

3.7.2.4 Washing of cells in the XFe96 microplate

After two washing steps with pre-warmed (37 °C) assay medium (100 µL per well), 175 µL of assay medium with or without the respective compounds were added to each well and the XFe96 microplate was placed in a non-CO_2 incubator for 60 min prior to the assay.

3.7.2.5 Loading of the XFe96 sensor cartridge with injection compounds

The hydrated XFe96 sensor cartridge ports were loaded with 25 µL of each injection compound, dissolved in assay medium (**Table 23**).

Port solutions for glycolysis stress test (standard)	
D-Glucose (8X)	80 mM
Oligomycin (9X)	9 µM
2-deoxy-D-glucose (10X)	500 mM
Assay medium (pH 7.35, 37 °C)	

Table 23: Port solutions for glycolysis stress test (standard)

3.7.2.6 Seahorse run

The assay template was designed with Wave 2.6.1 software and the run was performed with a Seahorse XFe96 Analyzer. Following calibration and equilibration, basal measurements of ECAR and OCR in assay medium without glucose and pyruvate were performed. Firstly, D-glucose was injected, followed by oligomycin injection, resulting in final well concentrations of 1 µM. Thirdly, 2-deoxy-D-glucose (2-DG) was injected, giving final well concentrations of 50 mM.

3.7.2.7 Normalization to cell number

Simultaneously with the 2-DG injection, Hoechst 33342 (45 µg/mL) was added to the cells. After the measurement, the Seahorse XFe96 plate was loaded into a Citation 1 multimode reader to determine Hoechst 33342 intensity, which was used as a measure of cell number.

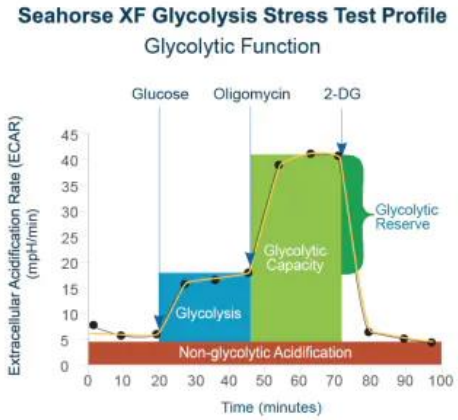

Figure 10: Agilent Seahorse Glycolysis Stress Test profile.
Sequential addition of different inhibitors and measured parameters are shown.

3.7.3 CYRIS flox

3.7.3.1 Seeding and treatment of cells in the sensor plate

HCT-15 cells were seeded at a density of 65×10^3 cells per well into a 24-well sensor plate and allowed to adhere overnight. Cells were pre-treated for 24 h as indicated prior to the assay.

3.7.3.2 Preparation of cells and sensor plate

Directly before the beginning of the automated measurement, cells were washed, the medium was replaced by corresponding measuring medium, the cover lid was put on and the plate was loaded into the instrument. Subsequently, the run was started.

3.7.3.3 Normalization to cell number

After the measurement, cells number was determined with a crystal violet staining as described in **3.4.2**.

3.8 Quantitative real-time PCR analysis

mRNA was isolated from cell samples using the RNeasy® Mini Kit (250) as described by the manufacturer. mRNA concentration was subsequently determined using a Nanodrop® spectrophotometer. Reverse transcription was performed with the High-Capacity cDNA Reverse Transcription Kit according to the manufacturer's instructions. For the quantitative real-time polymerase chain reaction (qPCR), a QuantStudio™ 3 Real-Time PCR System was used. Primers were purchased from metabion (Planegg, Germany). They were designed using the NCBI database or the ThermoFisher Cloud OligoPerfect tool and the corresponding nucleotide codes are listed in **Table 24**. 100 ng of cDNA (2 µL), 6.25 µL PowerUp™ SYBR® Green Master Mix, 3.75 µL RNase-free water and 0.025 mol of each primer (0.25 µL) were used for each well of the MicroAmp® Fast Optical 96-Well Reaction Plate, 0.1 mL. The $\Delta\Delta C_T$ method was used to quantify changes in mRNA levels as described earlier [74] and actin was used as housekeeping gene. Previously, primer efficiency was determined for each primer pair using 500 ng, 50 ng and 5 ng of cDNA per well.

Target Name	FW/RV Primer	Sequence (5'-3')
Actin	FW	CCA ACC GCC AGA AGA TGA
Actin	RV	CCA GAG GCG TAC AGG GAT AG
GDH1	FW	AGG AAT GAC ACC AGG GTT TG
GDH1	RV	TCA GAC TCA CCA ACA GCA ATA C
GDH2	FW	CAC TCT GCC TTG GCA TAC AC
GDH2	RV	CTC AGG TCC AAT CCC AGG TT
GLUL	FW	CCT GCT TGT ATG CTG GAG TC
GLUL	RV	GAT CTC CCA TGC TGA TTC CT
GLS1	FW	GCT GTG CTC CAT TGA AGT GA
GLS1	RV	GCA AAC TGC CCT GAG AAG TC
GLS2	FW	ATC AGA AAG TGG CAT GCT GT
GLS2	RV	GCC TTT AGT GCA GTG GTG AA
GOT1	FW	CAA CTG GGA TTG ACC CAA CT
GOT1	RV	GGA ACA GAA ACC GGT GCT T
GOT2	FW	GTT TGC CTC TGC CAA TCA TAT G
GOT2	RV	GAG GGT TGG AAT ACA TGG GAC
GPT2	FW	GGA GCT AGT GAC GGC ATT TCT ACG A
GPT2	RV	CCC AGG GTT GAT TAT GCA GAG CA
SLC38A1	FW	GCA CCA CAG GGA AGT TCG TA
SLC38A1	RV	ACT ATC ACC ACC AGA ACG CG

Target Name	FW/RV Primer	Sequence (5'-3')
SLC38A2	FW	GCA GTG GAA TCC TTG GGC TT
SLC38A2	RV	ATA AAG ACC CTC CTT CAT TGG CA
SLC38A5	FW	GAG AGG GTG CCC GAA CCT
SLC38A5	RV	CCT CGA AAT CCA TGA ACT GGA C
SLC38A7	FW	CCC CAG GGA GAT TGG TTT CC
SLC38A7	RV	GGT CTT CAC TTC AGG CTG CT
SLC38A8	FW	GAC CTC AGC GAG ATC GTC AG
SLC38A8	RV	AAG ATG AAG GTG CCG ACC AG
SLC38A9	FW	GCC ATC CTG ACA ACA GCT CT
SLC38A9	RV	GGA GGA GGA GCC CTA CAA GA
SLC38A10	FW	ATG ATG TCA GTG GCT GTG GG
SLC38A10	RV	CTG GGA GGA AAG TGC GTT CT
SLC1A5	FW	GAA CTC CCA GCT TTC GGA CA
SLC1A5	RV	CCT TGG AGT CTC GAG GAG GA

Table 24: Primers with nucleotide codes used for qPCR analysis

3.9 Statistical analyses

All the listed experiments were conducted at least three times unless indicated otherwise in the figure legends. The given data are presented as means ± SEM or median values as indicated in the figure legends. Statistical differences between groups were assessed with a t-test (with Welch's correction as indicated) or with an ordinary one-way and two-way ANOVA, respectively, and the indicated multiple comparisons test. Statistical analyses were performed with GraphPad Prism software version 8.2.1. Statistically significant results are indicated in the figures. If no indication of significance is given, data were not statistically significant.

RESULTS

4 Results

4.1 Part I: Concomitant glutamine deprivation and V-ATPase inhibition causes metabolic shift towards glycolysis

4.1.1 The potential of combining V-ATPase inhibition and glutamine deprivation

4.1.1.1 Determination of cell model based on the response to glutamine starvation

In the beginning of this study, we tested several cancer cell lines from different tumor entities for their proliferation capacity in the presence or absence of glutamine, glutamate or both. Of note, we found three cell lines that are rather unaffected (BxPC-3, HUH7, MCF-7) by glutamine deprivation whereas four other cell lines (HCT-15, Panc 03.27, T24, HeLa) showed a decreased proliferation rate (**Figure 11**). Particularly, upon glutamine starvation relative proliferation was significantly decreased to 41.4% in HCT-15 cells, 52.2% in Panc 03.27 cells, 9.15% in T24 cells and 38.9% in HeLa cells. Interestingly, glutamate starvation had no significant effect in any of the tested cell lines, which is why this condition was not included in further experiments. Based on these results, we chose the colorectal adenocarcinoma HCT-15 cell line as well as BxPC-3 pancreatic cancer cells as a cell model in this study.

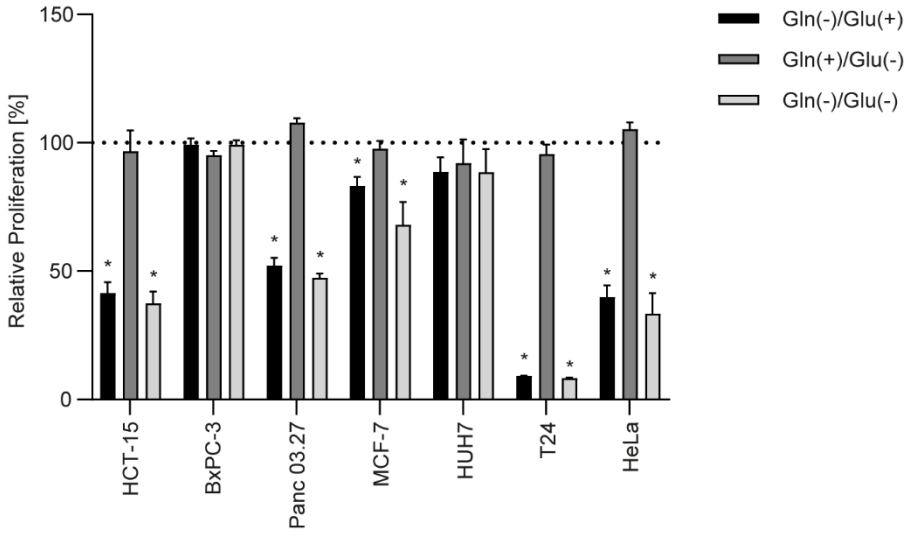

Figure 11: Glutamine dependency in cancer cell lines.
Relative proliferation was determined in HCT-15, BxPC-3, Panc 03.27, MCF-7, HUH7, T24 and HeLa cells by crystal violet staining. Cells were treated as indicated for 72 h. Bar graphs display relative proliferation normalized to full medium control (dotted line), mean ± SEM (n=3), One-way ANOVA followed by Dunnett´s multiple comparison test, *p<0.05.

4.1.1.2 Impact of glutamine deprivation and V-ATPase inhibition on lysosomal volume

Since lysosomes display the main organelles for cellular homeostasis upon scarce nutrient supply, we investigated the homeostatic changes of lysosomes induced by starvation. By utilizing a LysoTracker™ Green dye, which specifically stains cellular lysosomes, we assessed lysosomal volume upon glutamine starvation in combination with V-ATPase inhibitor Archazolid. Interestingly, we did not observe significant alterations in lysosomal volume upon glutamine starvation conditions in both HCT-15 and BxPC-3 cells, as this would result in an increased LysoTracker™ Green intensity (**Figure 12**). However, inhibiting the V-ATPase by Archazolid led to decreased lysosomal volume in both presence and absence of glutamine, from a concentration of 10 nM in HCT-15 as well as BxPC-3 cells (**Figure 12**), indicating lysosomal shrinking in a dose dependent manner. This may be derived from an altered lysosomal pH as LysoTracker™ Green is a weak base that is partially protonated in more acidic environments.

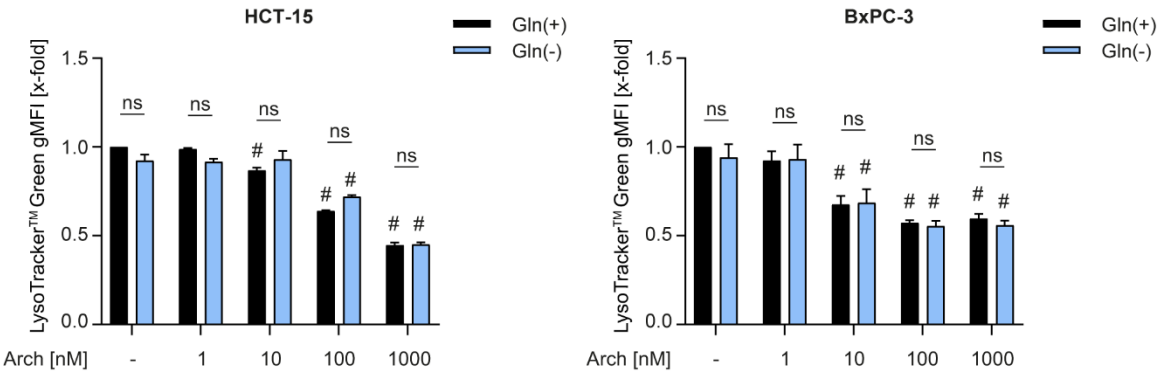

Figure 12: V-ATPase inhibition but not glutamine deprivation alters lysosomal volume.
LysoTracker™ Green fluorescence intensity indicates lysosomal volume. HCT-15 and BxPC-3 cells were treated as indicated for 24 h followed by LysoTracker™ Green FM staining. Geometric means of fluorescence intensity (gMFI) were determined by flow cytometry and normalized to DMSO control. Bar graphs display mean ± SEM (n=3), Two-way ANOVA followed by Tukey´s multiple comparison test, *p<0.05, ns ≙ not significant, #p<0.05 for multiple comparison test of group bars [Gln(+) and Gln(-), respectively] related to their corresponding control.

4.1.1.3 Glutamine deprivation facilitates lysosomal acidification

It has been reported that amino acid starvation causes a rising rate of lysosomal protein degradation through acidification of intracellular vesicles like lysosomes in order to maintain constant intracellular levels of free amino acids mediated through an increased V-ATPase activity [75]. Therefore, we investigated the lysosomal pH after glutamine deprivation together with concomitant V-ATPase inhibition. By assessing the lysosomal pH with semi-quantitative analysis of LysoSensor™ Green fluorescence via flow cytometry, we observed a significantly decreased pH after glutamine starvation as indicated by a more than twofold increase of LysoSensor™ Green signal in both HCT-15 and BxPC-3 cells (**Figure 13A**). Interestingly, a concomitant V-ATPase inhibition reversed this effect and restored the lysosomal pH to a level comparable to full medium conditions in both cell lines. Of note, single treatment of V-ATPase inhibitor Archazolid slightly decreased the LysoSensor™ Green intensity implying an increased lysosomal pH, however, this effect was not statistically significant. For further verification, a FITC-dextran staining was performed and assessed via confocal microscopy. FITC is a pH-sensitive dye that is quenched in the presence of protons. In consequence, a decreased FITC signal indicates a decreased lysosomal pH. After initial loading the cells with a 20 kDa FITC-labeled dextran, glutamine starvation treatment revealed a significantly decreased lysosomal pH in HCT-15 cells confirming the previous results. BxPC-3 cells showed the same trend, but the effect was not statistically significant. As expected, V-ATPase inhibitor Archazolid raised the lysosomal pH in HCT-15 and BxPC-3 cells under full medium and starvation conditions, indicating the prevention of lysosomal acidification when cells are glutamine deprived (**Figure 13B,C**).

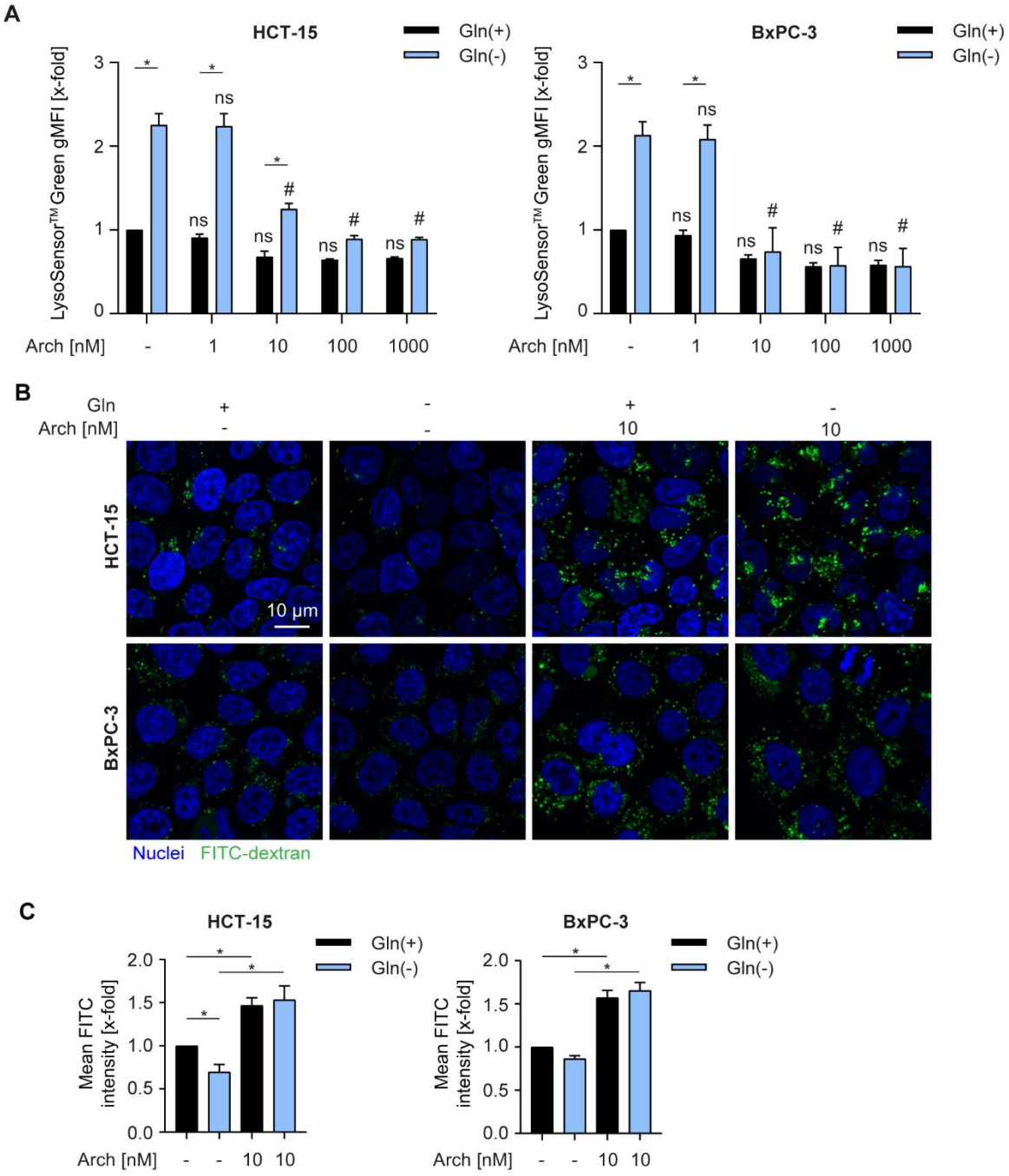

Figure 13: Glutamine deprivation decreases lysosomal pH.
(**A**) LysoTracker™ Sensor fluorescence intensity indicates lysosomal pH. HCT-15 cells and BxPC-3 cells were treated as indicated for 24 h followed by LysoSensor™ Green FM staining. Geometric means of fluorescence intensity (gMFI) were determined by flow cytometry and normalized to DMSO control. Bar graphs display mean ± SEM (n=3), Two-way ANOVA followed by Tukey´s multiple comparison test, *p<0.05, ns ≙ not significant, #p<0.05 for multiple comparison test of group bars [Gln(+) and Gln(-), respectively] related to their corresponding control. (**B**) HCT-15 and BxPC-3 cells were loaded with 200 µg/mL of FITC-dextran 20 kDa (green) for 24 h. Subsequently, cells were treated at the indicated concentrations for 1 h before staining with Hoechst 33342 (nuclei, blue). FITC-dextran intensity was assessed by confocal microscopy. Scale bar: 10 µm. One representative image out of three independent experiments is shown. (**C**) Quantification of mean FITC intensity of five independent images per condition was performed by ImageJ software. Bar graphs display mean ± SEM (n=3), Two-way ANOVA followed by Tukey´s multiple comparison test, *p<0.05.

4.1.1.4 Impact of glutamine starvation and V-ATPase inhibition on autophagy induction

Given that V-ATPase inhibition is generally considered to block autophagy by preventing the recruitment of LC3 (Microtubule-associated protein 1A/1B-light chain 3) to autophagosomes and autophagic acidification [76-78] and that cancer cells urgently rely on autophagy to overcome existential threats during lack of glutamine [79], we investigated the expression of crucial autophagy-related proteins by Western blot. Under autophagic stimuli the cytosolic form of LC3 named LC3 I is conjugated to phosphatidylethanolamine to form a LC3 conjugate named LC3 II. LC3 II in turn is recruited to the autophagosomal membrane and degraded under persistent autophagic signal [80]. Interestingly, we observed a significantly reduced protein level of both LC3 I and II in HCT-15 cells after withdrawal of glutamine, as their expression is decreased to 50% or less (**Figure 14A**). Additionally, V-ATPase inhibition reversed this effect and prohibited the induction of autophagy even under starvation conditions, which is shown by a significant accumulation of LC3 I and II after treatment of 10 nM Archazolid. In regard to p62, which is known to interact with ubiquitin and thereby facilitating degradation of proteins through the autophagosome, protein levels remained unchanged in HCT-15 cells and were slightly upregulated after high dose Archazolid treatment in BxPC-3 (**Figure 14B**). Furthermore, glutamine deprivation resulted in an increased AMP activated protein kinase alpha (AMPKα) phosphorylation in HCT-15 as well as BxPC-3 cells, the total form of AMPKα remained mainly unchanged (**Figure 14C**). Since AMPKα is not only a nutrient sensor that directs cellular metabolism towards metabolic adaptions to restore energy homeostasis [81], but also directly promotes autophagy by phosphorylating autophagy-related proteins [82], enhanced phosphorylation strengthens the observation of autophagy induction if glutamine is absent. Interestingly, V-ATPase inhibition did not affect AMPKα expression (**Figure 14C**). Besides, determination of mTORC1 downstream target p70S6K unraveled a reduced phosphorylation status when cells are deprived off glutamine, suggesting an inactivation of mTORC1 (**Figure 14D**). mTORC1 regulates cell growth and proliferation in response to energy levels and is inactivated under starvation conditions leading to lysosomal biogenesis and autophagy [83]. V-ATPase inhibition, again, did not influence phosphorylation of p70S6K. Summarized, this emphasizes that V-ATPase inhibition is capable of prohibiting alterations in lysosomal pH as well as autophagy induction caused by glutamine deprivation, indicating a great potential of a combination therapy of starvation and V-ATPase inhibitors in treating cancer.

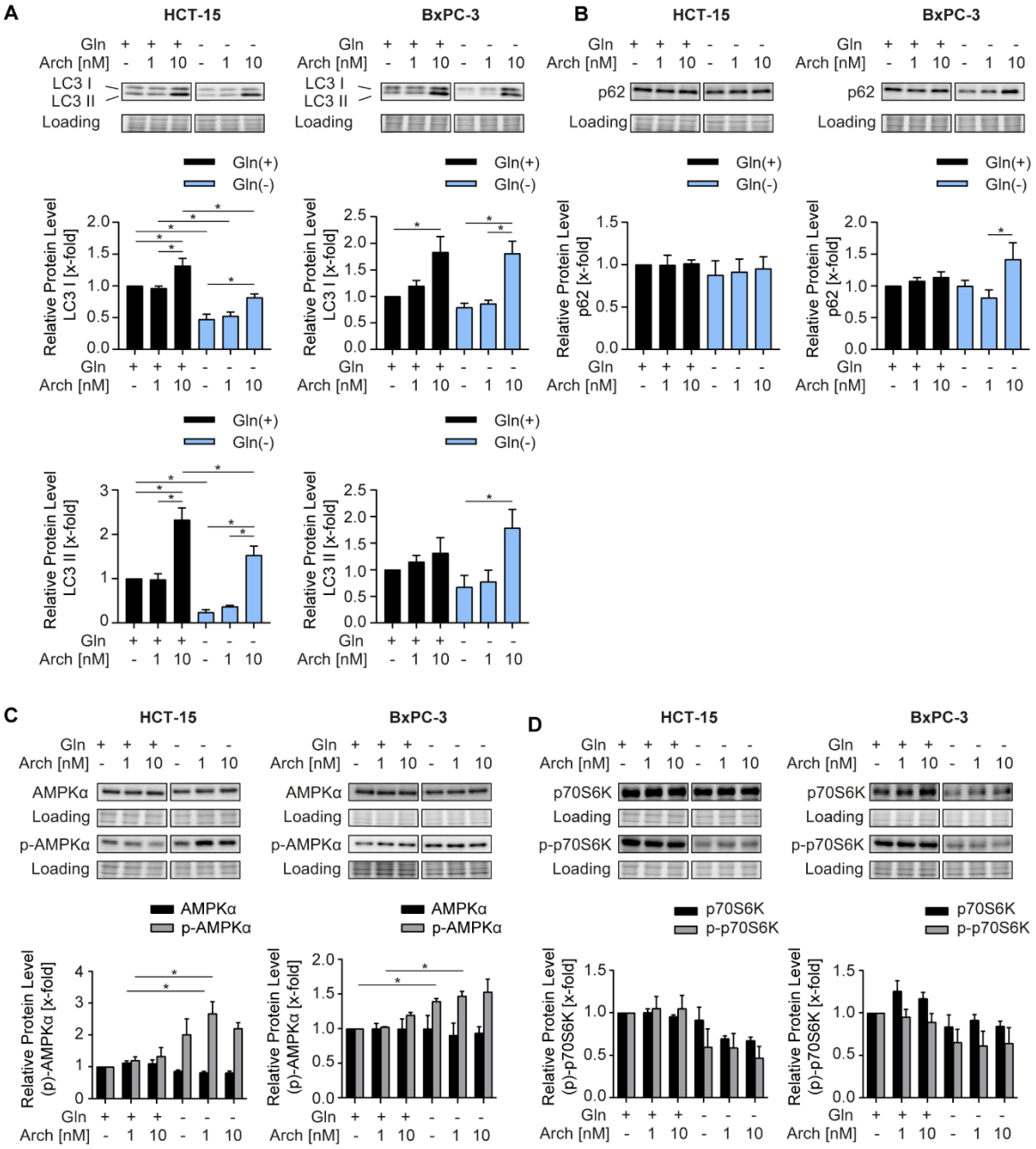

Figure 14: Autophagy is induced by glutamine starvation and blocked by concomitant V-ATPase inhibition.
(**A-D**) LC3 I & II (**A**), p62 (**B**) p70S6K & phosphorylated p70S6K (**C**) and AMPKα & phosphorylated AMPKα (**D**) protein levels were analyzed in HCT-15 and BxPC-3 cells by Western blotting after 24 h of treatment as indicated accompanied by quantification. One representative Western blot out of three independent experiments is shown. Bar graphs display mean ± SEM (n=3), Two-way ANOVA followed by Tukey´s multiple comparison test, *p<0.05.

4.1.2 Evaluating a combination treatment consisting of glutamine deprivation and V-ATPase inhibition

Therefore, we hypothesized that by inhibiting the V-ATPase under glutamine starvation conditions, we potentially could block cellular survival mechanisms, which might be beneficial for anti-cancer therapy. By analyzing cell proliferation and apoptosis induction under glutamine deprivation enabled by either starvation or pharmacological glutaminase inhibitors BPTES and CB-839, respectively, and concomitantly inhibiting the V-ATPase, a therapeutic benefit was investigated in our model cell lines. Surprisingly, crystal violet proliferation assay showed that glutaminase inhibitor CB-839 did not show a curve shift of sensitivity towards V-ATPase inhibitor Archazolid after 72 h treatment in both HCT-15 and BxPC-3 cells as also represented by equal IC_{50}-values (5.19 nM vs. 4.91 nM in HCT-15, 5.00 nM vs. 4.62 nM in BxPC-3) (**Figure 15A**). Moreover, a combination treatment increased the apoptosis rate after 48 h moderately (**Figure 15B**). In addition, another glutaminase inhibitor BPTES was tested in the same setup and displayed a significantly reduced proliferation of a combination treatment compared to Archazolid single treatment in HCT-15 cells (IC_{50}-values: 5.19 nM vs. 1.24 nM) (**Figure 15C**). Considering apoptosis, BPTES led to a significant increase of the capacity of Archazolid to induce apoptosis in both cell lines, however, the effect is most pronounced in HCT-15 cells (**Figure 15D**). Notably, a calcein retention assay revealed BPTES as an inhibitor of the well-known multidrug efflux transporter P-glycoprotein (P-gp), of which Archazolid is known as a substrate as well (**Figure 15G**). Thus, we assume that the additive effect potentially derives from an increased intracellular drug concentration of Archazolid caused by accumulation originating from a competition of P-gp between Archazolid and BPTES. Hence, to eliminate potential pharmacological off-target effects and to exclude inhibitor specificity issues, we tested proliferation and apoptosis under total glutamine starvation again. However, we observed no difference in dose-sensitivity towards Archazolid under glutamine starvation conditions in cell proliferation in both cell lines (IC_{50}-values: 5.19 nM vs. 4.95 nM in HCT-15, 5.00 nM vs. 5.72 nM in BxPC-3) (**Figure 15E**). Furthermore, the percentage of apoptotic cells was slightly increased in HCT-15 cells and moderately increased in BxPC-3 cells upon a combination treatment, however, not synergistically as we hypothesized (**Figure 15F**). Taken together, contrary to our hypothesis, these findings suggest that V-ATPase inhibition does not have a beneficial therapeutic effect in glutamine-deprived cancer cells.

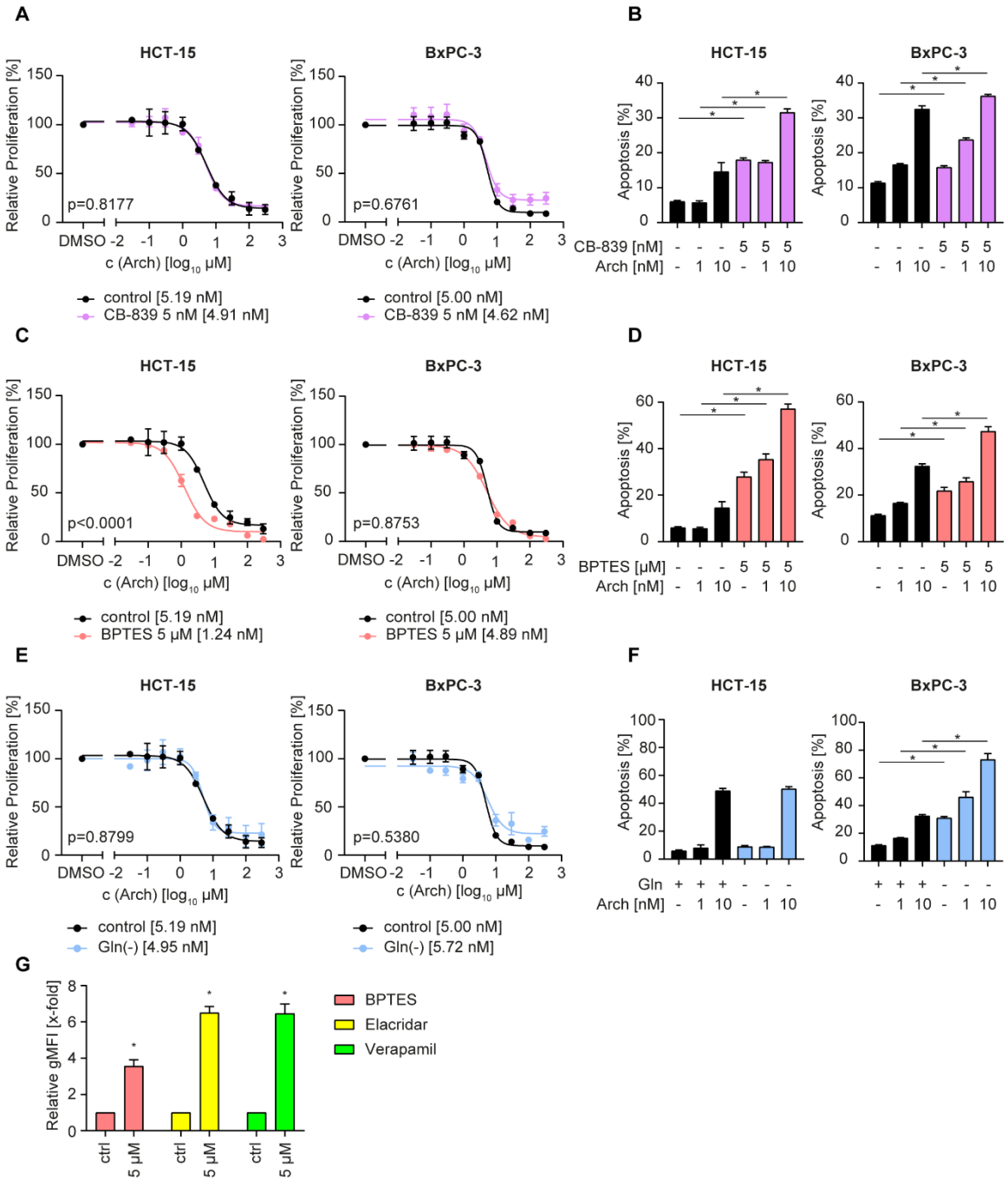

Figure 15: Combination of glutamine deprivation and V-ATPase inhibition does not lead to beneficial therapeutic effect.

(**A, C, E**) Proliferation was determined in HCT-15 and BxPC-3 cells by crystal violet staining. Cells were treated as indicated for 72 h. Data are mean ± SEM (n=3). Statistical significance was analyzed using the comparison of fits function of GraphPad Prism 8, comparing logIC_{50}-values. (**B, D, F**) Apoptosis in HCT-15 and BxPC-3 cells was assessed after 48 h by Nicoletti assay followed by flow cytometry analysis. Bar graphs display mean ± SEM (n=3), Two-way ANOVA followed by Tukey´s multiple comparison test, *p<0.05. (**G**) Retention of the P-gp model substrate calcein-AM in HCT-15 cells was determined by flow cytometry. Cells were incubated with calcein-AM, in presence or absence of BPTES and the positive controls verapamil and elacridar at the indicated concentrations. Bar graph displays mean ± SEM (n=3), unpaired t-test with Welch´s correction, *p<0.05.

4.1.3 Influence of combination treatment on amino acid transporters and glutamine metabolism related enzymes

4.1.3.1 Effects of V-ATPase inhibition and glutamine deprivation on the expression and localization of SLC transporters

Since we did not detect a synergistic effect of concomitantly depriving glutamine and inhibiting the V-ATPase in cancer cells, we were interested in elucidating underlying reasons. We assumed that cancer cells potentially evade negative events in proliferation or apoptosis induction by metabolic reprogramming. Metabolic reprogramming in malignant cells is not only restricted to a metabolic switch in order to obtain energy but also required for the acquisition of cellular material like for instance building blocks for protein synthesis [84]. Therefore, we investigated the expression of solute carrier family transporters (SLC), since they are responsible for the uptake of a broad range of neutral amino acids including glutamine or alanine. As depicted in **Figure 16A**, mRNA expression of SLCs determined by qPCR showed a transcriptional upregulation of SLC38A2, SLC38A8, SLC38A10 and SLC1A5 in HCT-15 cells under glutamine starvation conditions, whereas in contrast BxPC-3 cells showed a significant downregulation in SLC38A5, SLC38A7 and SLC38A10 in comparison to full medium conditions (statistical evaluation shown in **Supplementary Table 1**). However, we did not observe distinct changes in mRNA expression pattern of SLCs that could explain a missing therapeutic benefit of a combination therapy. Therefore, due to its ubiquitous expression, association with several tumors and major role in glutamine uptake [85-87], we focused on SLC1A5 for further studies. Intriguingly, depletion of SLC1A5 is known to assign SLC38A1 a crucial role in sustaining glutaminolysis [88], thus, we investigated this particular transporter in our studies as well. Western blot analysis of SLC1A5 and SLC38A1 disclosed a slightly enhanced expression of SLC1A5 in HCT-15 cells after glutamine starvation, however, the effect was not statistically significant (**Figure 16B**). Otherwise, we did not detect any significant changes in SLC38A1 and SLC1A5 expression. By using confocal microscopy, we elucidated the localization of the transporters, since their expression may be unaffected, yet the localization is crucial to accomplish their purpose of importing amino acids. Interestingly, glutamine starvation did not alter the phenotype compared to full medium control as both transporters are mainly located at the plasma membrane (**Figure 15C**). Treatment with Archazolid, though, led to an intracellular accumulation of both transporters independent from glutamine availability. This indicates a possible impairment of intracellular trafficking in which the V-ATPase is particularly involved [89].

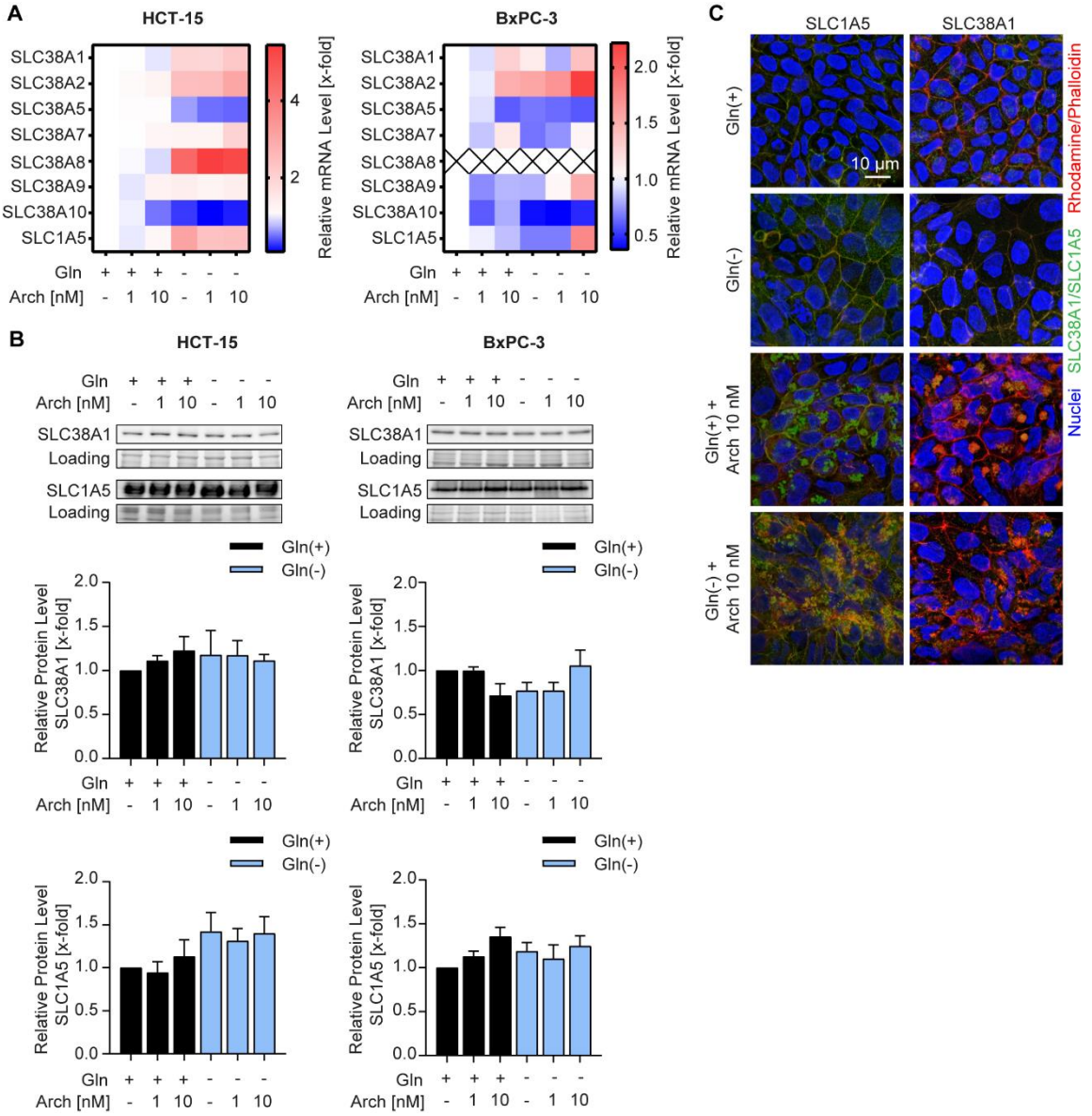

Figure 16: Combination therapy does not affect SLC1A5 and SLC38A1 expression but localization. (**A**) mRNA levels were analyzed by qPCR in HCT-15 and BxPC-3 cells after 24 h of treatment as indicated. Heat maps display median values (n=3). Statistical evaluation is shown in Supplementary Table 1. (**B**) SLC38A1 and SLC1A5 protein levels were analyzed in HCT-15 and BxPC-3 cells by Western blotting after 24 h of treatment as indicated accompanied by quantification. One representative Western blot out of three independent experiments is shown. Bar graphs display mean ± SEM (n=3), Two-way ANOVA followed by Tukey´s multiple comparison test, *p<0.05. (**C**) Cells were treated as indicated for 24 h before staining with Hoechst 33342 (nuclei, blue), Rhodamine/Phalloidin (actin, red) and SLC38A1 or SLC1A5, respectively (green), and analysis by confocal microscopy. Scale bar: 10 µm. One representative image out of three independent experiments is shown.

4.1.3.2 Glutamine deprivation increases endocytic uptake

Besides meeting their glutamine demand by external transporter mediated uptake, it has been evidently reported that cancer cells are also capable to utilize autophagy as well as endocytosis to internalize nutrient material. For instance, proteins are transported into the lysosomes after uptake via endocytosis or mediated through autophagic stimuli. Once in the lysosomes, they are then disassembled into their building blocks via lysosomal breakdown and finally further metabolized [90]. Given that glutamine deprivation causes autophagy, we further disclosed a significantly enhanced endocytic uptake after glutamine starvation by analysis of the intracellular fluorescence of a AlexaFluor™ 488 labeled transferrin conjugate, which was used as a model substrate. As shown in **Figure 17A**, HCT-15 cells displayed an about two times increased fluorescence intensity upon glutamine starvation compared to full medium control. We observed the same effect in BxPC-3 cells only to a lesser extent. With concomitant V-ATPase inhibition, the endocytic uptake was again at the same level as compared to the full medium group. Rising concentration of Archazolid even slightly reduced fluorescence intensity independent from glutamine availability, presumably caused by interfering with intracellular trafficking as mentioned before. Macromolecules, which were either endocytosed or provided via autophagy, are lysed inside the lysosomal lumen and the generated building blocks, in particular glutamine, need to be released to the cytosol for further metabolization. This release is mediated by another member of the SLC family, named SLC38A7, which has been described to be the primary exporter of glutamine from the lysosome in cancer cells [91]. Interestingly, in qPCR experiments an increase in SLC38A7 mRNA expression upon combination treatment was detected in HCT-15 cells, which potentially suggests an SLC38A7-mediated compensation mechanism (**Figure 16A**). Thus, we assumed that when cancer cells are exposed to an environment with scarce glutamine availability, they utilize the alternative pathways of degrading macromolecules followed by lysosomal export to cover the demand of glutamine. In this regard, a knockdown of SLC38A7 was performed (transfection efficiency depicted in **Supplementary Figure 1**) to determine whether SLC38A7 facilitates an escape mechanism by which cancer cells circumvent glutamine starvation. However, genetic silencing did not lead to a reduction of proliferation and apoptosis induction, since both parameters remained on the same level as the non-targeting control (**Figure 17B,C**). This suggests that cancer cells might compensate for a lack of glutamine by endocytosis, however, the release of glutamine from the lysosomes via SLC38A7 seems not to be responsible for sustained cancer cell growth and survival.

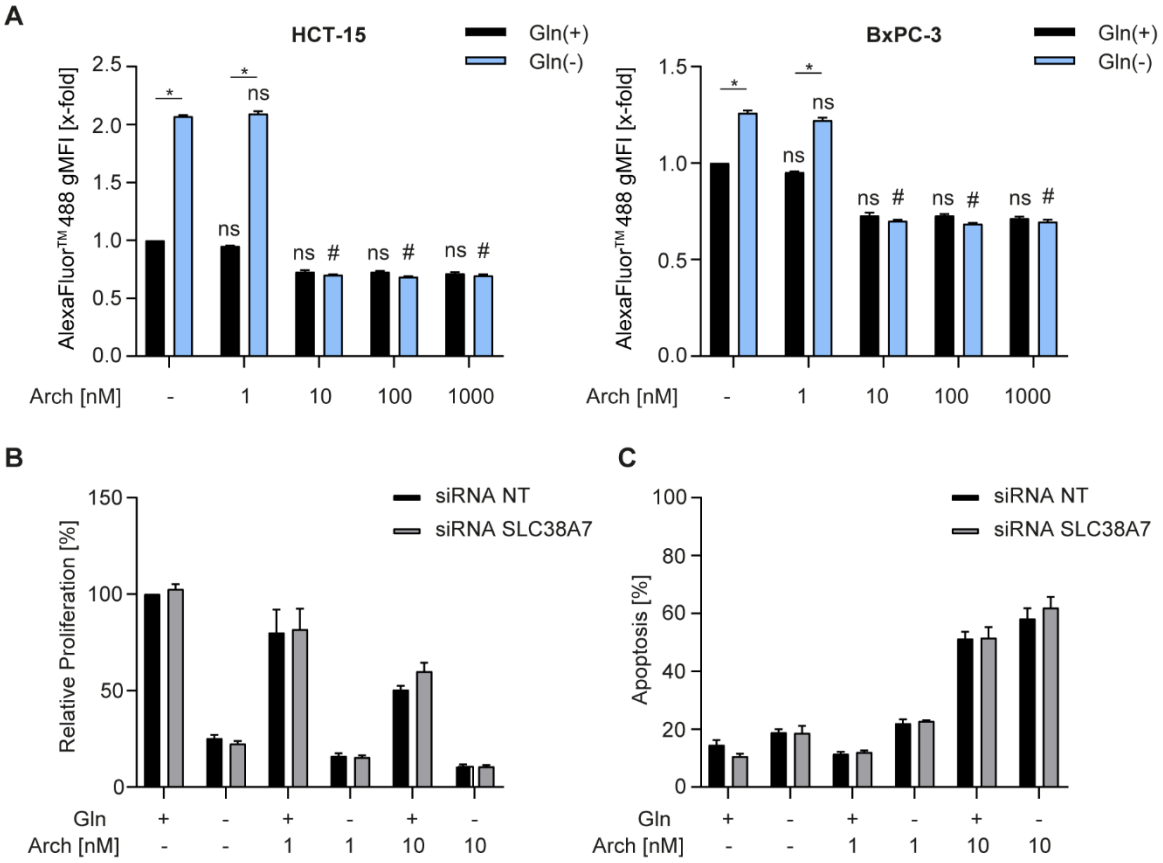

Figure 17: Glutamine starvation enhances endocytic uptake.
(**A**) HCT-15 and BxPC3 cells were stimulated at the indicated concentrations for 24 h. Subsequently, AlexaFluor™ 488-transferrin conjugate (5 µg/mL) was added and incubated for 1 h. AlexaFluor™ 488 intensity was assessed by flow cytometry analysis and displayed as geometric mean of fluorescent intensity (gMFI). Bar graphs display mean ± SEM (n=3), Two-way ANOVA followed by Tukey´s multiple comparison test, *p<0.05, ns ≙ not significant, #p<0.05 for multiple comparison test of group bars [Gln(+) and Gln(-), respectively] related to their corresponding control. (**B**) Proliferation was determined in HCT-15 cells by crystal violet staining. Cells were transfected 24 h prior to stimulation with non-targeting (NT) control siRNA or siRNA targeting SLC38A7 using DharmaFECT™ transfection reagent. Subsequently cells were treated as indicated for 72 h. Bar graphs display mean ± SEM (n=3), Two-way ANOVA followed by Tukey´s multiple comparison test, *p<0.05. (**C**) Apoptosis in HCT-15 and BxPC-3 cells was assessed after 48 h by Nicoletti assay followed by flow cytometry analysis. Cells were transfected 24 h prior to stimulation with non-targeting control siRNA or siRNA targeting SLC38A7 using DharmaFECT™ transfection reagent. Bar graphs display mean ± SEM (n=3), Two-way ANOVA followed by Tukey´s multiple comparison test, *p<0.05.

4.1.3.3 Expression of glutaminolysis related enzymes is altered upon glutamine deprivation

Next, we aimed to further investigate the implication of glutamine metabolism related enzymes as they can contribute to metabolic reprogramming. Therefore, we analyzed the expression of enzymes associated with glutaminolysis, with special attention to glutamine synthetase (GLUL), since its responsibility for de novo glutamine synthesis. Interestingly, GLUL is downregulated on mRNA level after glutamine starvation in HCT-15 as well as BxPC-3 cells, implying that enhanced de novo synthesis of glutamine does not account for a missing therapeutic benefit (**Figure 18**). Furthermore, glutaminases (GLS), which catalyze the conversion of glutamine into glutamate and ammonia, remained mostly unchanged. Glutamate is then metabolized to α-ketoglutarate by either glutamate-oxalacetate transaminase (GOT), glutamatedyhrogenase (GDH) or glutamate-pyruvate transaminase (GPT). Upon glutamine starvation, GPT2 expression was significantly upregulated in BxPC-3 and HCT-15 cells, in which also GOT1 expression was increased (statistical evaluation shown in **Supplementary Table 2**). However, qPCR experiments disclosed no relevant differences in their expression upon a combination treatment of glutamine deprivation and V-ATPase inhibition that could explain the absent therapeutic benefit, thus we did not focus on that topic in this study.

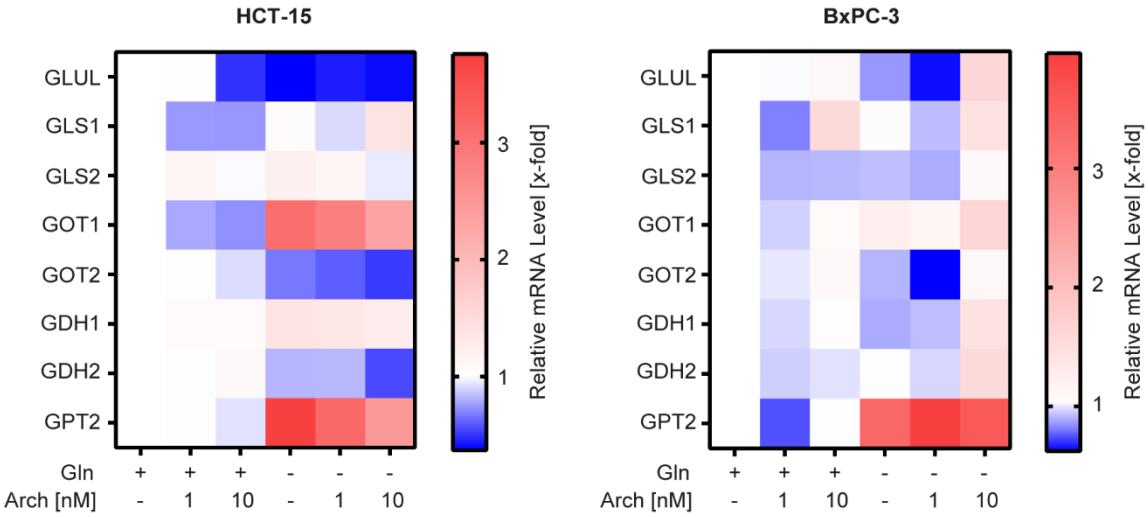

Figure 18: Glutaminolysis related enzyme expression.
mRNA levels were analyzed by qPCR after 24 h of treatment as indicated. Heat maps display median values (n=3). Statistical evaluation is shown in Supplementary Table 2.

4.1.4 Metabolic shift towards glycolysis

4.1.4.1 Upregulation of extracellular acidification rate upon combination treatment

Another option that could account for the missing therapeutic benefit of a combination treatment beyond adaption of glutamine metabolism is that cancer cells potentially reprogram their metabolism to alternative energy sources rather than glutamine to sustain proliferation and survival. Hence, we investigated potential alterations in glycolysis as alternative fuel since metabolizing glucose might substitute -at least partly- for the lack of glutamine. Very interestingly, a glycolysis stress test performed on a Seahorse™ device unraveled a significant upregulation of extracellular acidification rate (ECAR) in HCT-15 cells under low glutamine conditions and an even stronger increase together with V-ATPase inhibition (**Figure 19A**,**B**). Of note, for metabolic profiling low glutamine condition was selected instead of total glutamine starvation since minimal glutamine concentrations are required to ensure that the cells do not completely shut down their metabolism and to better determine metabolic up- or especially downregulations. Therefore, we chose 20% (117 mg/L) of glutamine concentration compared to full medium as under this condition HCT-15 cells are not impaired in proliferation and thus, we assumed a functioning metabolism (**Supplementary Figure 2**). The rate by which cells acidify the extracellular medium mirrors the glycolytic production of acidic lactate starting from neutral glucose, so ECAR is commonly used as a direct and quantitative measure of glycolytic rate and therefore serves as a readout for glycolytic activity [92, 93]. Sequential addition of glucose, ATP synthetase inhibitor oligomycin and 2-DG allows assessment of glycolytic parameters (**Figure 10**). Thereby, glucose enables glycolysis, oligomycin blocks mitochondrial respiration and thus driving cells to utilize glycolysis to its maximum capacity and 2-DG completely shuts down glycolysis. Evaluation of parameters derived from the glycolysis stress test unveiled a significantly upregulated glycolytic capacity and -reserve, which displays the capability of cells to respond to an energetic demand, after combination treatment (**Figure 19B**). Additionally, the obtained results were verified by a metabolic stress test on a Cyris® flox, which is a novel semi-automated real-time platform capable of measuring cellular metabolism parameters. More precisely, HCT-15 cells displayed an increased ECAR resulting in an elevated glycolytic capacity and glycolytic reserve upon glutamine deprivation, which were both even enhanced after concomitant treatment with Archazolid (**Figure 19C,D**). Summarized, increased ECARs in both glycolytic capacity and -reserve parameters clearly indicate that HCT-15 cells employ glycolysis for energy generation under glutamine deprivation and concomitant V-ATPase inhibition.

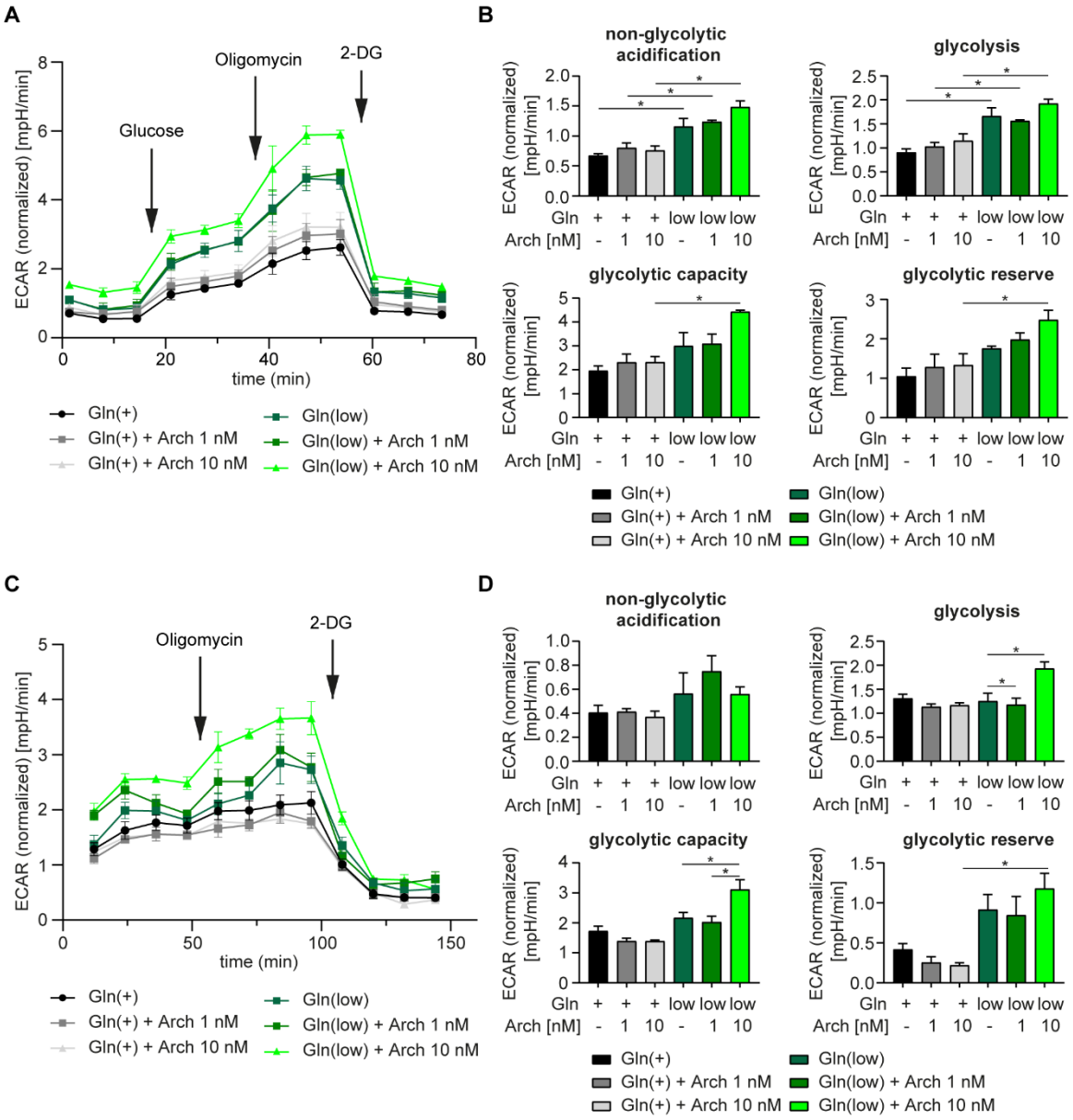

Figure 19: Concomitant glutamine deprivation and V-ATPase inhibition increases extracellular acidification rate.

(**A**) HCT-15 cells were subjected to extracellular flux analysis on a Seahorse XFe96 device. Cells were pretreated as indicated for 24 h, prior to glycolysis stress test. Metabolic profiling was performed after 1 h of glucose starvation to assess basal glycolytic activity, which was followed by sequential injection of D-glucose and oligomycin to determine glycolysis activity after injection of saturating concentrations of glucose and glycolytic reserve upon inhibition of oxidative phosphorylation, respectively. The last injection of the glycolysis inhibitor 2-DG served as control. ECAR (extracellular acidification rate) ratio is displayed over time as mean ± SEM. ECAR was normalized to cell number. (**B**) Calculation of glycolytic parameters based on results from **A**. Bar graphs display mean ± SEM (n=3), Two-way ANOVA followed by Tukey´s multiple comparison test, *p<0.05. (**C**) HCT-15 cells were subjected to extracellular flux analysis on a CYRIS® flox platform. Cells were pre-treated as indicated for 24 h, prior to metabolic stress test. Metabolic profiling was performed directly after applying measuring medium containing D-glucose. This was followed by injection of oligomycin to determine glycolytic capacity and glycolytic reserve upon inhibition of oxidative phosphorylation. The last injection of the glycolysis inhibitor 2-DG served as control. ECAR is displayed over time as mean ± SEM. ECAR was normalized to cell number. (**D**) Calculation of glycolytic parameters based on results from **C**. Bar graphs display mean ± SEM (n=3), Two-way ANOVA followed by Tukey´s multiple comparison test, *p<0.05.

4.1.4.2 Combination treatment elevates glycolytic enzyme activity

After gaining initial evidence of an upregulated glycolysis that might explain a missing therapeutic benefit of a combination treatment, we further elucidated the expression of enzymes that are responsible for the step-by-step conversion of glucose to lactate. Analysis of protein levels by Western blotting revealed no significant alterations upon any kind of treatment in both HCT-15 and BxPC-3 (**Figure 20A**) (statistical evaluation shown in **Supplementary Table 3**). However, enzymatic expression does not inevitably reflect the enzymatic activity, therefore we further assessed the combined activity of all hexokinases isoforms. Hexokinases are responsible for the catalyzation of the phosphorylation of glucose to glucose-6-phosphate, which represents the first, obligatory, and rate-limiting step of glycolysis. **Figure 20B** clearly depicts that neither glutamine deprivation nor V-ATPase inhibition alone significantly altered hexokinase activity, however, a combination treatment of both led to a significant increase of enzyme activity. This finding further supports the assumptions that glycolysis is induced to maintain cellular metabolism after challenging cancer cells with glutamine deprivation and concomitant V-ATPase inhibition.

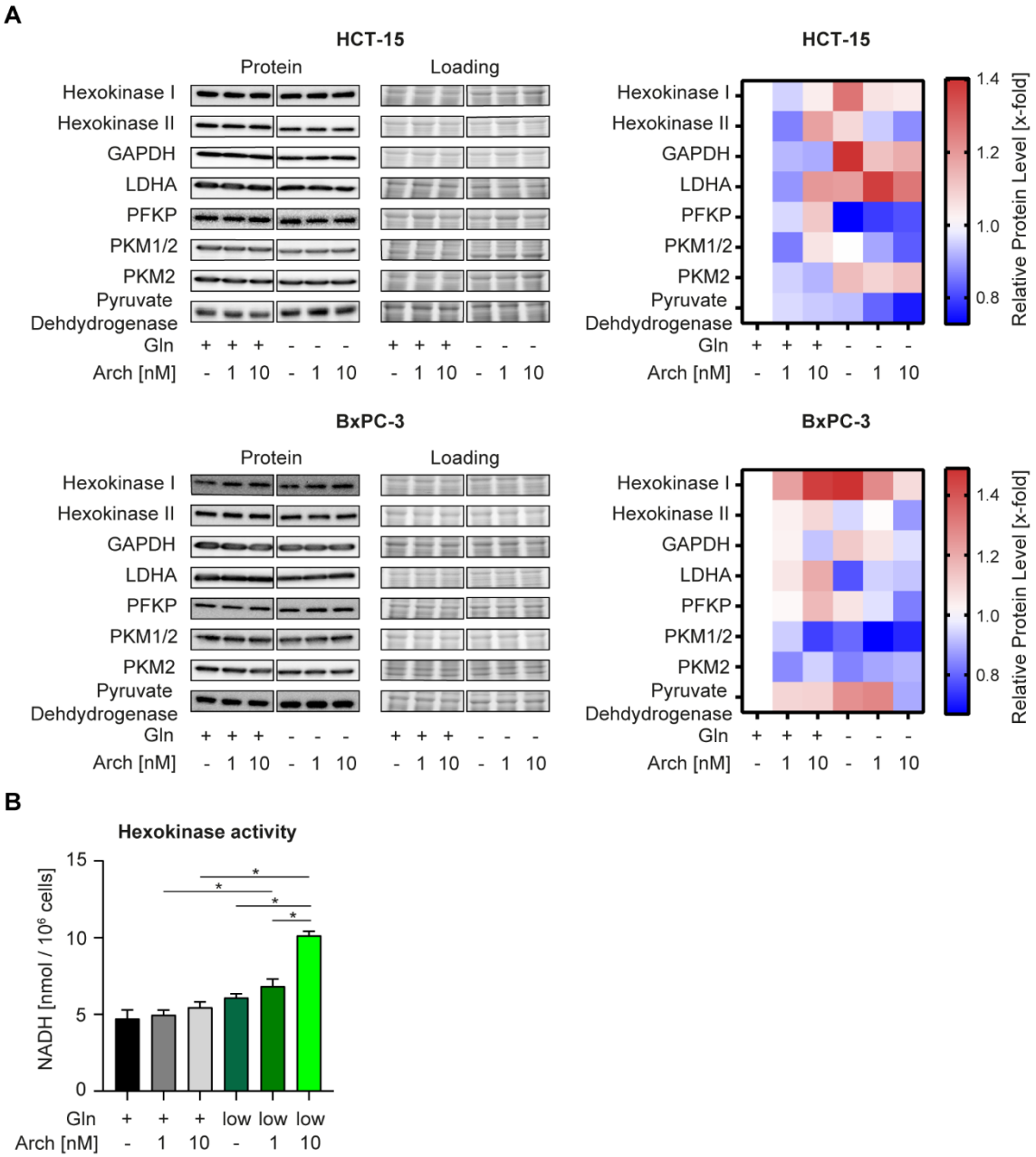

Figure 20: Concomitant glutamine deprivation and V-ATPase inhibition does not influence expression of glycolysis related enzymes but increases hexokinase activity.
(**A**) Glycolysis related enzyme protein levels in HCT-15 and BxPC-3 cells analyzed by Western blotting after 24 h of treatment as indicated. Heat maps display median values (n=3). One representative Western blot out of three independent experiments is shown. (**B**) HCT-15 cells were treated as indicated for 24 h followed by determination of hexokinase activity. Bar graphs display mean ± SEM (n=3), Two-way ANOVA followed by Tukey´s multiple comparison test, *p<0.05.

4.1.5 Part I: Summary

In sum, in this study we demonstrated a clear decrease of lysosomal pH and an autophagy induction upon glutamine deprivation, which could be reversed with concomitant V-ATPase inhibition. The resulting approach to test a combination treatment of both in the regard to anti-proliferative effects and apoptosis initiation, however, did not lead to a synergistic effect. Investigation of the underlying mechanisms revealed that neither solute carrier family transporters nor glutaminolysis related enzymes account for a potential cellular compensation that circumvents sustained cancer cell growth and survival. However, metabolic profiling disclosed a significant upregulation of glycolysis upon concomitant glutamine deprivation and V-ATPase inhibition, which is further supported by an upregulation of enzymatic hexokinase activity. Thus, we conclude that the metabolic shift to an increased reliance on glycolysis can at least partly explain why we did not observe a beneficial therapeutic effect of a combination between glutamine deprivation and V-ATPase inhibitor Archazolid, which also implies a metabolic plasticity in cancer cells.

4.2 Part II: Zephycandidine A analogs as novel anti-cancer drugs

4.2.1 Anti-cancer effects of Zephycandidine A analogs

In 2016, Zhan et al. were the first to isolate Zephycandidne A, a naturally occurring imidazo[1,2-*f*]phenanthridine alkaloid from the plant *Zephyranthes candida* and investigated its anti-tumoral potential [22]. They described a strong cytotoxic capacity in several cancer cells lines with IC_{50}-values in the lower micromolar range accompanied with tumor specificity as they claim less toxicity in a non-cancer Beas-2B cell line. Additionally, Zephycandidine A was reported to exhibit apoptosis inducing properties, further confirming its anti-cancer effects. In close cooperation with the group of Prof. Dr. Bracher (Ludwig-Maximilians-University, Munich, Germany), we tested multiple Zephycandidine A analogs (**Figure 21A**), which were synthesized by Thomas Klaßmüller, towards their potential as novel anti-cancer drugs. Firstly, the antiproliferative properties of our compound library were evaluated using the acute T-cell leukemia Jurkat and mammary gland adenocarcinoma MCF-7 cell line. Thereby, two molecules with at least equal potency as compared to the parental structure were identified, namely THK-99 (IC_{50}-values: 9.54 µM in Jurkat, 32.7 µM in MCF-7) and THK-121 (IC_{50}-values: 11.8 µM in Jurkat, 33.7 µM in MCF-7), which both led to diminished cancer cell proliferation and were determined as hit compounds (**Figure 21B,C**). Of note, parental compound Zephycandidine A displayed IC_{50}-values in the micromolar range (11.7 µM in Jurkat, 145 µM in MCF-7). On the basis of these results, we selected three compounds (THK-99, THK-115 and THK-121) for further testing in two additional cancer cell lines from leukemia type (CCRF-CEM and HL-60, respectively) as well as one from breast cancer entity (MDA-MD-231) to verify the observed effects. Both hit structures THK-99 and THK-121 showed equipotent or even enhanced antiproliferative effects compared to Zephycandidine A in all tested cancer cell lines (**Figure 21D-F**). Concluded, those two Zephycandidine A analogs were biologically active and are capable of inhibiting cancer cell proliferation. In the next step, we aimed to investigate whether Zephycandidine A and its related analogs are toxic to non-cancerous HUVECs. For that purpose, we determined cell proliferation upon treatment with our selected compounds for 72 h. Interestingly, we observed that all tested Zephycandidine A analogs compromise most cancer cell lines more than the non-cancerous cell line, which is also reflected by higher IC_{50}-values in HUVECs (**Figure 21G,H**). Accordingly, the difference of the IC_{50}-values between cancer vs. non-cancer cell lines was higher for the hit analogs than for the parental structure Zephycandidine A, indicating an enlarged therapeutic window.

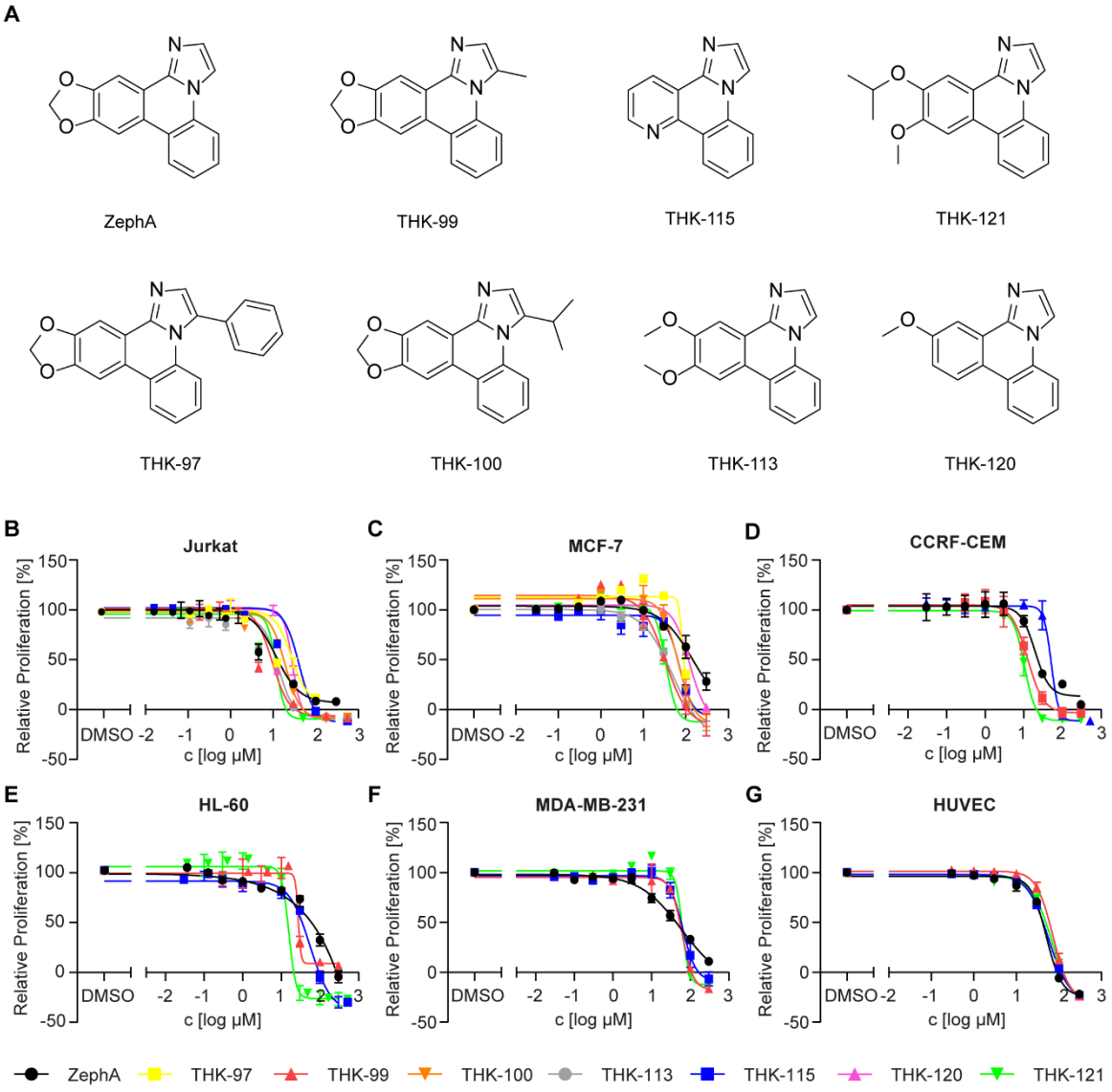

H

IC_{50}- value table [µM]

Cell Line	ZephA	THK-99	THK-115	THK-121	THK-97	THK-100	THK-113	THK-120
Jurkat	11.7	9.54	41.0	11.8	26.8	19.3	13.4	28.2
MCF-7	145	32.7	69.4	33.7	79.4	64.9	47.5	121
CCRF-CEM	19.5	12.6	51.3	10.3	-	-	-	-
HL-60	n.a.	27.3	55.8	15.6	-	-	-	-
MDA-MB-231	58.7	61.4	63.2	62.3	-	-	-	-
HUVEC	50.4	72.6	56.6	67.2	-	-	-	-

Figure 21: Zephycandidine A analogs decrease cancer cell proliferation.
(**A**) Chemical structure of Zephycandidine A and its related analogs. (**B-G**) Relative proliferation was determined in Jurkat (**B**), MCF-7 (**C**), CCRF-CEM (**D**), HL-60 (**E**), MDA-MB-231 (**F**) and HUVEC (**G**) cells by CellTiter®-Blue cell viability assay. Cells were treated as indicated for 72 h. Data are mean ± SEM (n=3). (**H**) Table of corresponding IC_{50}-values of **B-G**.

To elucidate whether a diminished cancer cell proliferation contribute to increased cell death rates, apoptosis and cell death assays, respectively, were performed. More precisely, apoptosis was determined for adherent breast cancer cell lines via propidium iodide staining according to Nicoletti et al. [69] whereas cell death was assessed in suspension leukemia cell lines via forward vs. sideward scatter (FSC vs. SSC) gating [71, 72]. Based on the determined antiproliferative activity, we chose concentrations around the respective calculated IC_{20}, IC_{50}, and IC_{80}-values for monitoring cell death. The parental structure Zephycandidine A moderately induced cell death in all tested cancer cell lines at a concentration of 100 µM with at most around 50% (**Figure 22A-E**). At a concentration level of IC_{80}-values hit compound THK-99 displays modest cell death rates of about 40% in four cancer cell lines with exception of CCRF-CEM cell line, in which the rate is over 80%. Furthermore, samples treated with THK-121 showed over 70% dead cells at the highest concentration in four cell lines, highlighting its superiority in facilitating cell death in comparison to Zephycandidine A. To further investigate the mode of cell death induction, we assessed alteration in the levels of crucial apoptosis-related proteins by Western blot analysis. Among them is active caspase-3 that plays a central role in mediating apoptosis and is considered as key effector, representing an orifice of the extrinsic and intrinsic pathway of apoptosis [94, 95]. Caspase-3 in turn is capable of cleaving and therefore inactivating PARP (poly [ADP-ribose] polymerase), which exerts its physiological role in DNA repair and maintenance of chromatin integrity [96]. Remarkably, Zephycandidine A exhibited caspase-3 activation at the same level as the control group and accordingly no significant PARP cleavage was detectable in Jurkat cells (**Figure 22F-H**). In contrast, the analog THK-121 displayed an about 30-fold increase of caspase-3, accompanied by a striking upregulation of PARP cleavage. THK-99 treatment did not lead to a significant activation of caspase-3 and accordingly the ratio of PARP cleavage was only slightly upregulated upon 25 µM. Intriguingly, leukemia cell lines seem to be more sensitive towards any kind of treatment compared to adherent breast cancer cell lines, which possibly emerges from an augmented entry surface of the cells for the compounds. Concluded, our hit structure THK-121 displayed clear cytotoxic effects in a variety of cancer cell lines, which is also associated with a strong induction of apoptosis, whereas the parental structure Zephycandidine A merely showed moderate effects. This evidently suggests a superiority of the THK-121 analog compared to the lead structure.

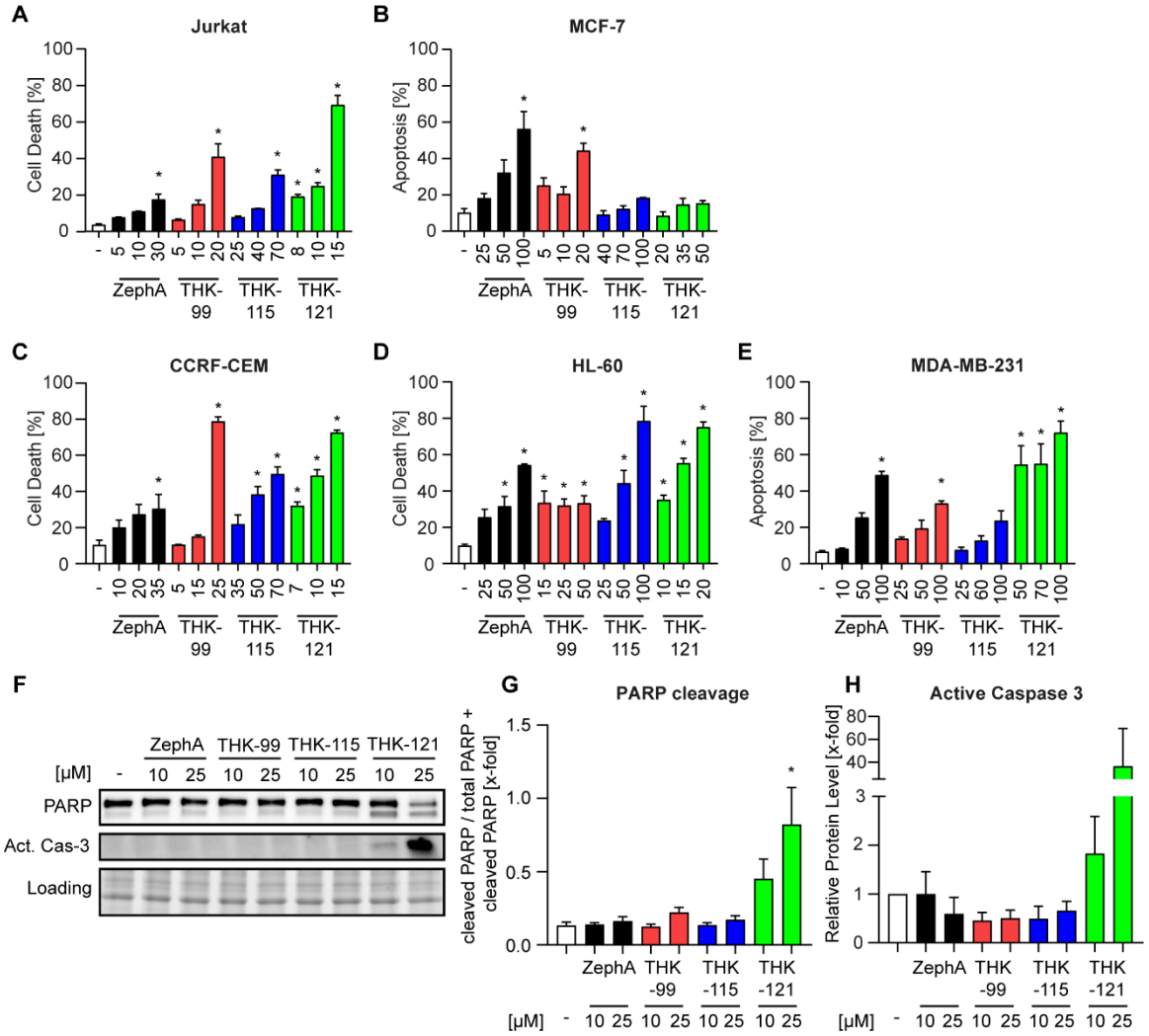

Figure 22: Zephycandidine A analogs induce cell death.
(**A-E**) Cell death was assessed after 48 h by forward versus sideward (FSC vs. SSC) scatter gating for Jurkat (**A**), CCRF-CEM (**C**), HL-60 (**D**) cells and by Nicoletti assay for MCF-7 (**B**) and MDA-MB-231 cells (**E**) followed by flow cytometry analysis. Bar graphs display mean ± SEM (n=3), One-way ANOVA followed by Dunnett´s multiple comparison test, *p<0.05. (**F**) PARP and active caspase-3 protein levels in Jurkat cells analyzed by Western blotting after 24 h of treatment as indicated. One representative Western blot out of three independent experiments is shown. (**G,H**) Quantification of **F**. Bar graphs display mean ± SEM (n=3), One-way ANOVA followed by Dunnett´s multiple comparison test, p*<0.05.

4.2.2 Zephycandidine A analogs trigger the intrinsic apoptotic pathway

Since our compounds apparently induce cell death and apoptosis, we were particularly interested in the mode of action. Apoptosis can be at least initiated via two signaling pathways: either the intrinsic or extrinsic pathway. While the extrinsic pathway is mediated by specialized death receptors that transmit signals from extracellular death ligands across the plasma membrane to engage the intracellular caspase machinery [97-99], the intrinsic apoptosis pathway is activated by internal stimuli such as oxidative stress or DNA damage [100]. Hence, to decipher which pathway is addressed we investigated the protein levels of important markers that may serve for mediation of intrinsic apoptosis by Western blot analysis. Members of the Bcl family, which can be subdivided into pro- and antiapoptotic proteins, respectively, are present on the mitochondrial membrane and known to be the key mediators for the intrinsic apoptotic pathway after transcriptional activation upon apoptotic stimuli [101]. Thereby, potential alterations of two members of the Bcl-2 family, Mcl-1 and Bax, were assessed after 24 h treatment. Mcl-1 is an anti-apoptotic member promoting cell survival by interfering at an early stage in a cascade of events leading to release of cytochrome c from mitochondria and is also rapidly downregulated during apoptosis [102]. Bax, in turn, is capable of forming a mitochondrial apoptosis induced channel (MAC) in the mitochondrial outer membrane leading again to cytochrome c release and therefore considered as pro-apoptotic [103, 104]. Regarding cellular expression of Mcl-1 in Jurkat cells, **Figure 23A,B** depicts a downregulation to 38% upon 24 h treatment by THK-121, whereas the expression after treating with Zephycandidine A remained on the same level as the control. Of note, in MCF-7 no significant changes in Mcl-1 expression were detected (**Figure 23D,E**). THK-99 showed a similar diminished expression of Mcl-1, however, to lesser extent. Additionally, THK-121 led to about 2.5-fold upregulation of Bax expression in Jurkat cells and 1.5-fold upregulation in MCF-7 cells, respectively (**Figure 23A,C,D,F**). Zephycandidine A also showed a slight increase in Bax expression in both cell lines. To sum up, we conclude that Zephycandide A analogs induced the intrinsic apoptotic pathway.

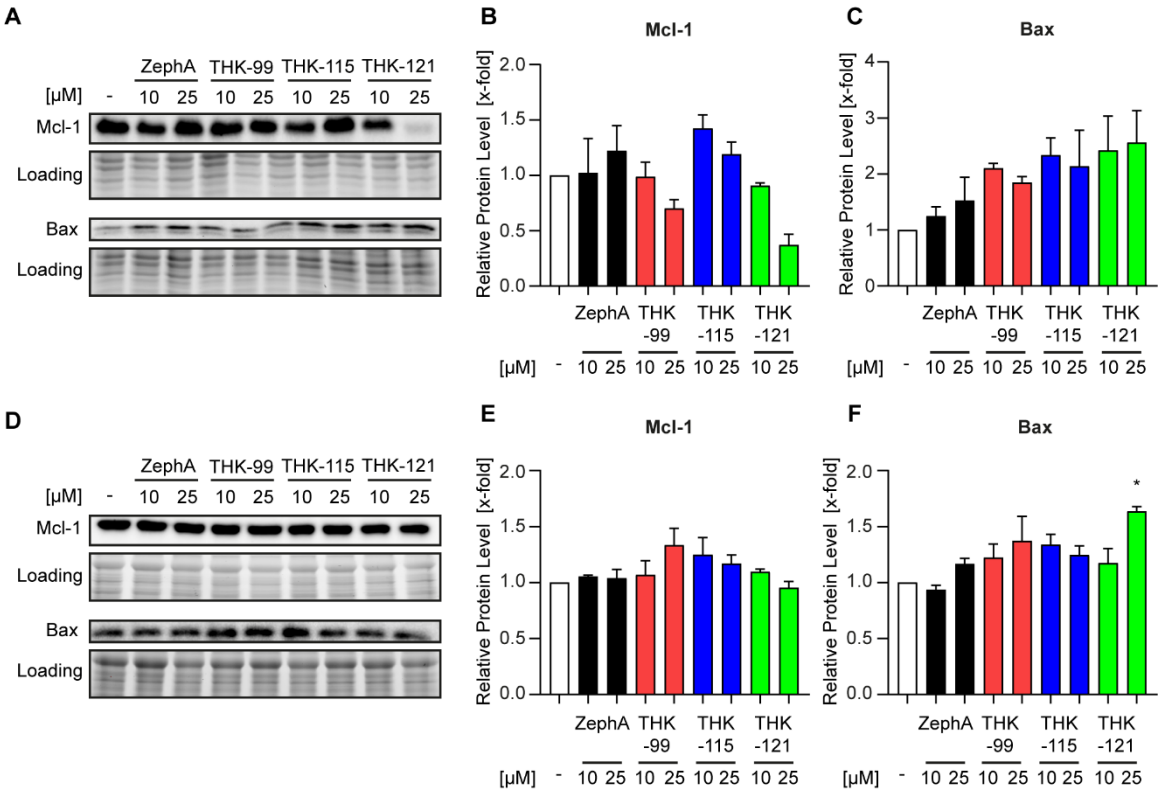

Figure 23: Zephycandidine A analogs induce intrinsic apoptosis.
(**A-F**) Mcl-1 and Bax protein levels in Jurkat (**A-C**) and MCF-7 (**D-F**) cells analyzed by Western blotting after 24 h of treatment as indicated. (**B-C**) Quantification of **A**. (**E-F**) Quantification of (**D**). One representative Western blot out of three independent experiments is shown. Bar graphs display mean ± SEM (n=3), One-way ANOVA followed by Dunnett´s multiple comparison test, p*<0.05.

4.2.3 Zephycandidine A analogs disrupt mitochondrial function

After initial evidence of the involvement of mitochondria in mediating apoptosis by alteration of Bcl-2 family members, which are associated with mitochondrial membrane integrity, we next explored whether mitochondria are affected by Zephycandidine analogs. Hence, we assessed the mitochondrial membrane potential (Δψm) and formation of mitochondrial superoxides, since apoptotic signaling executioner caspases, like for instance caspase-3, enter the mitochondria and disrupt complexes of the respiratory chain, which further results in the abrogation of mitochondrial membrane potential and generation of superoxides [63]. In terms of detection whether the mitochondrial membrane potential is abrogated upon treatment a JC-1 staining can be utilized and analyzed by flow cytometry. JC-1 is a cationic dye, which can be used to monitor mitochondrial health and mitochondrial membrane potential (Δψm). When Δψm is intact, JC-1 accumulates in the healthy mitochondria forming aggregates, which elicit a red fluorescence signal. In contrast, damaged mitochondria show mitochondrial depolarization that is indicated by a decreased red/green fluorescence intensity. **Figure 24A,B** clearly demonstrates a significantly upregulated number of dissipated mitochondria in Jurkat (53%) as well as MCF-7 (25%) cells after 24 h of treatment with 25 µM of THK-121. Contrary, the parental structure did not show a detectable loss of mitochondrial membrane potential, whereas THK-99 showed a slight upregulation of dissipated mitochondria in MCF-7, however, not statistically significant. By utilizing MitoSOX^{TM} Red staining mitochondrial superoxides were detected via flow cytometry, unveiling a slight increase upon Zephycandidine A treatment in both cell lines (**Figure 24C,D**). THK-99 displayed a small increase of mitochondrial superoxides as well, while THK-121 treatment led to a more than 4-fold upregulation of mitochondrial superoxide in Jurkat cells and about 1.5-fold upregulation in MCF-7 cells. Collectively, we suggest that treatment with Zephycandidine A and especially its analog THK-121 affected the mitochondria as not only the Δψm is abrogated but also mitochondrial superoxide production is clearly increased, which finally hints to mitochondrial dysfunction.

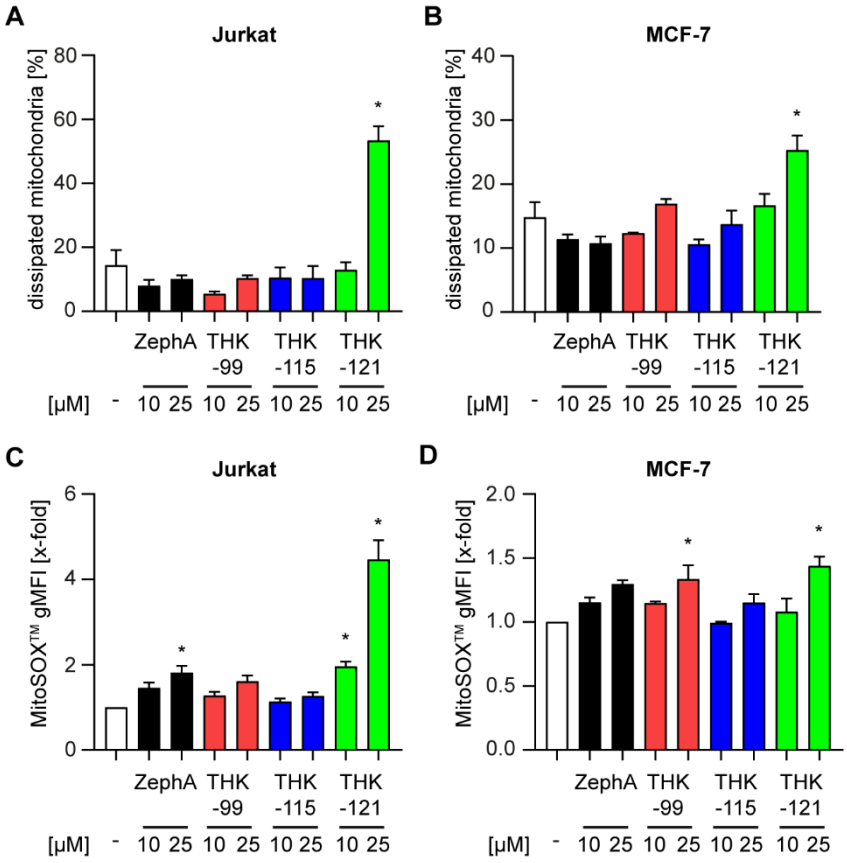

Figure 24: Zephycandidine A analogs abrogate mitochondrial membrane potential and induce mitochondrial superoxides.
(**A,B**) Jurkat (**A**) and MCF-7 (**B**) cells were treated as indicated for 24 h followed by JC-1 staining. Loss of mitochondrial membrane potential was quantified by determining the percentage of green fluorescence caused by JC-1 monomers via flow cytometry. Bar graphs display mean ± SEM (n=3), One-way ANOVA followed by Dunnett´s multiple comparison test, p*<0.05. (**C,D**) Jurkat (**C**) and MCF-7 (**D**) cells were treated as indicated for 24 h followed by MitoSOX™ Red Superoxide Indicator staining. Mitochondrial superoxide was determined by flow cytometry analysis and displayed as geometric mean of fluorescent intensity (gMFI). Bar graphs display mean ± SEM (n=3), One-way ANOVA followed by Dunnett´s multiple comparison test, p*<0.05.

Closely correlated to mitochondrial dysfunction are alterations in mitochondrial morphology as several studies reported. For instance, mitochondrial oxidative stress can cause a fragmented structure of the mitochondrial network [64, 105, 106]. Therefore, we stained MCF-7 cells with MitoTracker™ Red CMXRos followed by assessment of mitochondrial morphology via confocal imaging. Interestingly, while we observed fiber-shaped, elongated mitochondria in cells of the control group, treatment with 25 µM of THK-99 and THK-121, respectively, resulted in seemingly round-shaped nature of mitochondria that indicate dysfunctionality (**Figure 24A**). Computer-based evaluation of confocal images via the ImageJ plugin MiNA of shape descriptors confirmed this finding, since while mean branch length (length of each single mitochondrion) remained unchanged upon treatment, mean branches per network (extent of mitochondrial branching per network) and mean summed branches length (size of each individual network) were significantly

decreased (**Figure 25B-D**). Treatment with parental structure Zephycandidine A in contrast led only to a slight downregulation of mitochondrial branching and network size. This evidently demonstrates that mitochondrial dynamics are severely altered upon treatment with Zephycandidine A analogs.

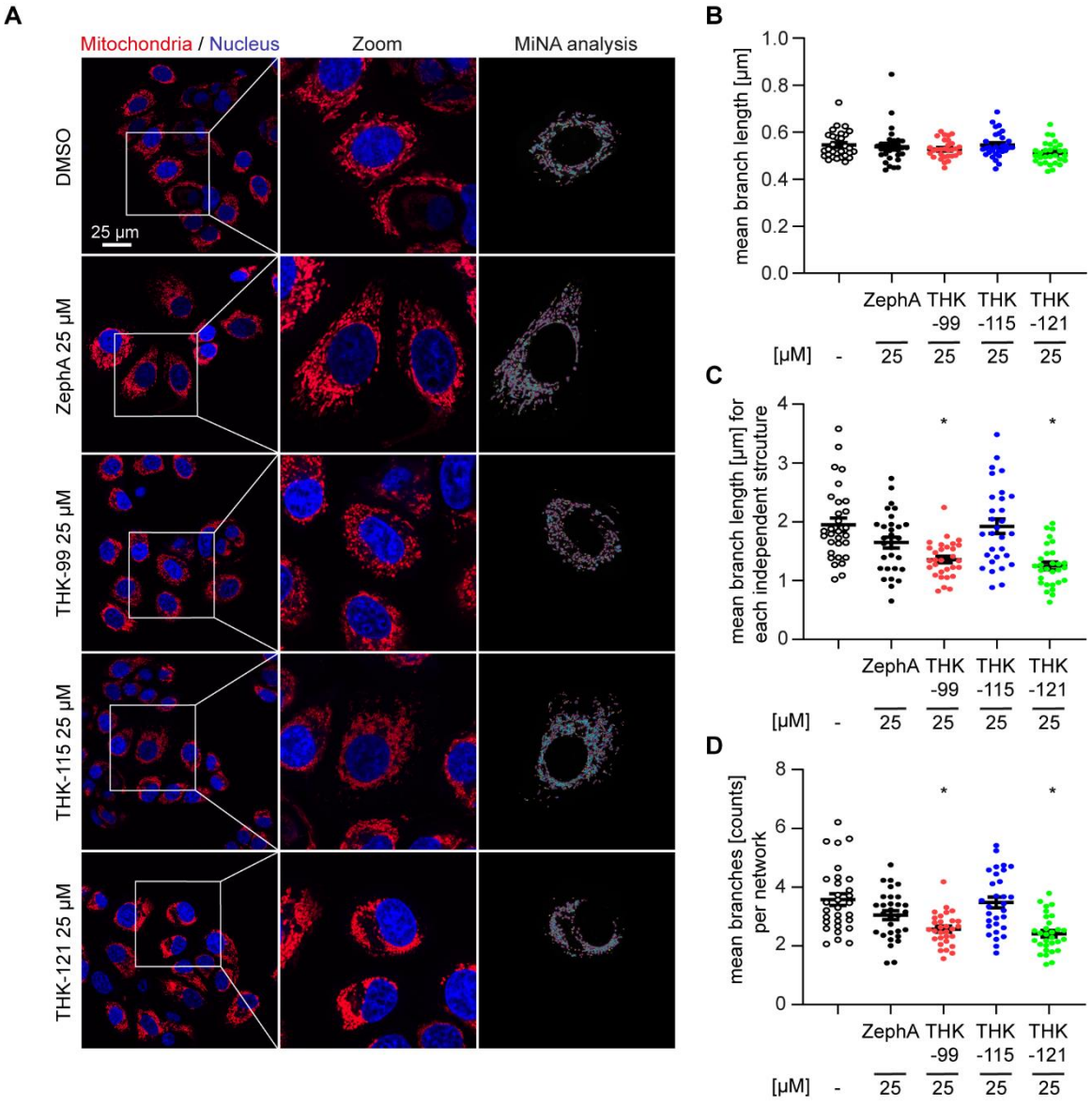

Figure 25: Zephycandidine A analogs alter mitochondrial morphology.
(**A**) MCF-7 cells were treated at the indicated concentrations for 24 h before staining with MitoTracker™ Red CMXRos (mitochondria) and Hoechst 33342 (nuclei). Mitochondrial morphology was assessed using confocal imaging. Scale bar: 25 µM. One representative image out of three independent experiments is shown. In addition, an ImageJ plugin MiNA analysis output image is depicted. Purple area represents mitochondrial signal. Green lines represent length of mitochondria. Blue dots mark connection sites between mitochondria and yellow dots mark the end of network structures. (**B-D**) Results from MiNA analysis of **A** performed on 10 cells per replicate. Scatter plot graphs display mean ± SEM (n=3), One-way ANOVA followed by Dunnett´s multiple comparison test), p*<0.05.

In response to mitochondrial dysfunction cells typically upregulate mitochondrial mass as a compensatory mechanism to restore a functional mitochondria pool through biogenesis [66]. Using MitoTracker™ Green FM staining we determined mitochondrial mass and revealed that Zephycandidine A treatment did not lead to a detectable elevation of mitochondrial mass, whereas upon THK-121 treatment Jurkat as well as MCF-7 cells displayed a significant upregulation. (**Figure 26A,B**).

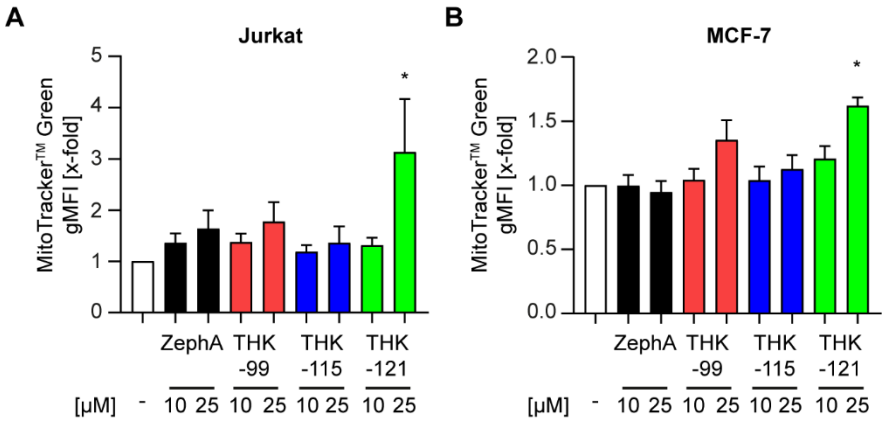

Figure 26: Zephycandidine A analogs increase mitochondrial mass.
(**A, B**) Jurkat (**A**) and MCF-7 (**B**) cells were treated as indicated for 24 h followed by MitoTracker™ Green FM staining. Mitochondrial mass was determined by flow cytometry analysis and displayed as geometric mean of fluorescent intensity (gMFI). Bar graphs display mean ± SEM (n=3), One-way ANOVA followed by Dunnett´s multiple comparison test), p*<0.05.

4.2.4 Part II: Summary

Taken together, in this study, we demonstrated that Zephycandidine A exhibits growth inhibitory potential in five different cancer cell lines and further identified two chemical analogs, named THK-99 and THK-121, with significant antiproliferative properties as hit structures. Additionally, we found a broadened therapeutic window for the hit compounds compared to the parental structure as manifested by rather insensitivity towards treatment of a non-cancer cell line, indicating a selective manner for cancer cells. Furthermore, this study revealed a strong cell death induction of THK-99 as well as THK-121. Moreover, we showed that Zephycandidine A and its related analogs trigger the intrinsic apoptotic pathway by affecting the mitochondria via abrogation of the mitochondrial membrane potential, generation of mitochondrial superoxides, increase of mitochondrial mass, and alterations in morphology. Therefore, we describe for the first time, Zephycandidine A analogs with increased potential and cancer selectivity.

DISCUSSION

5 Discussion

5.1 Discussion Part I:

Indisputably, the rising tumor burden worldwide urgently requires novel medical strategies for the improvement of cancer therapy. Over 90 years ago, Otto Warburg was the first scientist connecting metabolism to cancer, as he discovered an enhanced aerobic glycolytic flux even under non hypoxic conditions, which is commonly known as the Warburg-effect [107]. Nowadays, deregulated tumor metabolism is inevitably considered as “hallmark of cancer” as published by Hanahan and Weinberg [108]. Interestingly, the rather inefficient metabolism of glucose in tumor cells can be mirrored by a seemingly wasteful metabolism of glutamine [109, 110]. In some tumor types, the demand of glutamine outpaces the endogenous supply, meaning that glutamine has to be taken up from exogenous sources otherwise those cancer cells cannot survive [111]. In that case glutamine becomes an “conditional essential” amino acid.

5.1.1 Cellular responses to glutamine deprivation and V-ATPase inhibition

Over the last decades, targeting of the glutamine metabolism by either pharmacological inhibition of breakdown processes, glutamine uptake or especially deprivation from addicted cells came more and more into focus of current therapy approaches, whereas the underlying biological mechanisms remain to be elucidated.

Since lysosomes are the vital intracellular organelles that provide the information on amino acids availability [40, 41] and coordinate cellular adaption mechanisms to the environment [112], we investigated the impact of glutamine starvation on lysosomal properties. In our experiments we observed a clear downregulation of the lysosomal pH following glutamine deprivation, which was abolished by simultaneously inhibiting the V-ATPase, indicating that lysosomal acidification as adaption to altered glutamine supply is mediated through the V-ATPase (**Figure 13**). Accordingly, Stransky and Forgac reported that amino acid availability influences the lysosomal pH in HEK293T cells by either increased or decreased V-ATPase activity, which is facilitated through V-ATPase assembly or disassembly, respectively. In particular, amino acid starvation causes an increased V-ATPase assembly and therefore a rising rate of lysosomal protein degradation through acidification of intracellular vesicles like lysosomes in order to maintain constant intracellular levels of free amino acids. Along this line, they also showed an abolished V-ATPase assembly after treatment with inhibitor Concanamycin A, indicating that V-ATPase inhibition may prevent a decrease of lysosomal pH in response to amino acid starvation [75]. Additionally, it has

been described most recently that especially glutamine is responsible for the regulation of lysosomal pH via the release of ammonia in mouse embryonic fibroblasts. In glutamine breakdown processes ammonia molecules are generated, which -once they get into the lysosomes- are protonated through the acidic interior. Consequently, this leads to a loss of free protons meaning an elevated lysosomal pH [113, 114]. In contrast to these findings, two other studies published an elevated lysosomal pH after serum starvation [115, 116]. However, we speculate that this effect may be due to the “nonspecific” serum starvation due to the absence of growth factors, vitamins and hormones other than amino acids in the serum. With this study we support evidence that glutamine starvation leads to a significant lysosomal acidification.

Beyond adaptive elevation of lysosomal pH, there is accumulating evidence in the literature that glutamine deprivation also triggers autophagy as pro-survival mechanism majorly mediated by mTORC1. As an example, Xiong et al. observed decreased LC3 II levels in primary mouse embryonic fibroblasts upon glutamine starvation. Intriguingly, total amino acid starvation caused the same effect, therefore the authors decided to remove every single amino acids contained in the medium and observed that solely glutamine withdrawal led to LC3 II degradation [113]. Moreover, Li et al. found an activation of autophagy in colorectal SW480 cells manifested by an increased LC3 I to LC3 II conversion [117]. In line with these findings, this study clearly supports the fact that glutamine deprivation induces autophagy as we also observed downregulation of LC3 II protein levels and a reduced mTORC1 phosphorylation upon starvation (**Figure 14A,D**). Notably, simultaneous treatment with V-ATPase inhibitor Archazolid did reverse LC3 II downregulation in our experiments, showing that V-ATPase inhibition can prevent autophagy induction, which has been described for Bafilomycin A1 [77, 118, 119]. Evidently, also AMPKα is a key modulator of the response to nutrient supply and facilitates the activation of autophagy by directly phosphorylating downstream targets like mTORC1 and ULK1 (UNC-51-like kinase 1) [82]. Lately, Bodineau et al. unveiled an increased AMPKα phosphorylation upon amino acid starvation in human bone osteosarcoma epithelial U2OS cells. Interestingly, this effect was abolished after in the presence of glutamine and leucine but not any other amino acid, implying that these two amino acids are directly impacting AMPKα activation [120]. Hence, we tested whether glutamine deprivation leads to an enhanced phosphorylation in our experimental setup, which we would confirm (**Figure 14C**). In line with the previous reports of our group, V-ATPase inhibition with Archazolid did not further affect AMPKα phosphorylation [121].

Taken together, with this study we add evidence that V-ATPase inhibition is capable of blocking cellular adaption mechanisms, which are evoked by glutamine deprivation making V-ATPase inhibition an interesting approach to target glutamine metabolism.

5.1.2 Targeting glutamine metabolism - glutaminases

Historically, chemotherapeutics that specifically target metabolism pathways have been effective treatment options and were used widely with solid success. Already in 1947, Sidney Farber discovered disease remission in children diagnosed with acute lymphoblastic leukemia (ALL) by administering aminopterin. This drug is a precursor of currently used drug methotrexate and is a folate analog that finally inhibits de novo nucleotide synthesis. The early clinical success of antifolates led to the development of an entire class of drugs known as “antimetabolites” with clear clinical benefit [122, 123]. This success stems from an increased metabolic demand of cancer cells for nucleotide biosynthesis required in cell division processes. Given the excessive demand of glutamine -also referred as “glutamine addiction”- especially for aggressive tumor entities that have a poor survival rates [124-126], addressing glutamine metabolism as anti-cancer target became a promising approach in recent research.

A number of strategies can be used to influence glutamine metabolism including glutamine deprivation, restriction of glutamine uptake, the usage of glutamine analogs and the reduction of glutamine metabolic enzyme activities [127]. However, to date, most attempts to target glutaminolysis clinically have focused on the inhibition of glutaminases, due to their crucial role in a variety of cancer entities [128-130]. There are several small molecule inhibitors such as BPTES, CB-839 and compound 968 that target glutaminases that are not commonly expressed in non-cancerous cells [131], however with different specificity. Precisely, BPTES is a specific inhibitor of glutaminase isoform 1 (GLS1) with limited solubility and bioavailability, whereas CB-839 is a more selective and potent GLS1 inhibitor and entered phase II clinical trial [132, 133]. In contrast, 968 is a specific inhibitor of the shorter splice variant of GLS1 [134]. In the literature the anti-cancer properties of these compounds have been described multiple times, emphazising the potential of glutaminase inhibition as therapeutic approach in fighting cancer [135-137]. Although inhibiting glutaminases suppresses cancer cell growth, monotherapy is frequently inefficient to induce cell death in tumor cells due to metabolic compensation including autophagy [127, 138, 139].

Thus, in this study we tested a combination therapy of glutaminase inhibitors BPTES and CB-839, respectively, as well as glutamine deprivation together with V-ATPase inhibitor Archazolid, which is known to prevent autophagy. Surprisingly, combined treatment did not lead to a synergistic effect in terms of reducing cell proliferation and promoting apoptosis (**Figure 15**). Notably, BPTES led to a significantly increased sensitivity towards Archazolid in HCT-15 cells (**Figure 15C**), showing a discrepancy to the results obtained from glutamine starvation and CB-839. By revealing BPTES being an P-gp substrate (**Figure 15G**), we assume that the underlying effect derives from an increased intracellular drug concentration caused by competition for P-gp binding sites, since Archazolid has also been described to be a substrate of the multidrug efflux transporter [140], which is especially highly expressed in HCT-15 cells [141].

Interestingly, Halama et al. investigated the effects of glutaminase inhibitor 968 and simultaneous autophagy inhibition mediated by bafilomycin A and chloroquine. In contrast to our findings, they observed a significantly greater decrease in cell viability after 72 h upon combination treatment than with any single agent in two triple negative breast cancer cell lines as well as in small lung cancer cells [138]. Similarly, it has been reported that the inhibition of autophagy by chloroquine potentiated viability inhibition and apoptosis activation induced by glutamine deprivation in colorectal SW480 cancer cell line [117]. Another study showed a significant activation of caspase-3 and caspase-9 upon combination of glutamine starvation and chloroquine treatment in human pancreatic adenocarcinoma cells [142]. These studies demonstrate that glutaminase inhibition is an effective approach in not only diminishing cancer cell growth but also increasing cancer cells' sensitivity to autophagy inhibiting agents. In this study, we could not particularly verify this effect and speculate further cellular adaption mechanism are responsible for a missing therapeutic benefit of a combination treatment in our experiments.

5.1.3 Impact of SLC transporter family – more than just amino acid transporters

One possible strategy to improve metabolic fitness could be the compensatory upregulation of SLC amino acid importers located at the plasma membrane as glutamine is mainly provided by external uptake to maintain intracellular glutamine levels in cancer cells. The uptake of amino acids is mediated by a variety of transport proteins belonging to the SLC family with more than three hundred members identified by now that are categorized to their transport mode and substrate specificity [143]. Until today there are 14 membrane proteins known to be capable of transporting glutamine, which belong to

four distinct gene families: SLC1, SLC6, SLC7 and SLC38. The latter is generally considered to be the principal transporters for glutamine [144]. There is evidence in the literature that these amino acid transporters enable a switch to other nutrient sources due to their substrate specificity under diminished glutamine supply. For instance, Zhang et al. reported a genetic upregulation of amino acid transporters in autophagy-deficient atg3 and atg7 knock-out HCT-116 colon carcinoma cells upon glutamine deprivation in an ATF4 dependent manner, consequently leading to increased amino acid uptake [145]. Along this line, upregulation of amino acid transporters is known to enable cancer cell adaption to glutamine deprivation by utilizing other alternative amino acids as substrates [146]. With qPCR experiments we examined the mRNA expression of crucial amino acid transporters, but did not observe any profoundly altered expression levels, except for SLC38A7, which is significantly upregulated after concomitantly inhibiting the V-ATPase and withdrawal of glutamine (**Figure 16A**). Contrary to our results, Morotti et al. recently discovered an upregulation of SLC38A1 at mRNA and protein expression after glutamine deprivation in MCF-7 and HCC1806 cell lines, whereas levels in MDA-MB-468 and MDA-MB-231 cells remained unchanged [147].

Besides expression, localization also decides whether amino acid transporters are capable of facilitating their purposes. In this study we focused on the most prominent one, which is the SLC1A5 that is recognized as the primary transporter for glutamine [148]. SLC1A5 is a Na^+-dependent neutral amino acid transporter, hence it requires the exchange of Na^+ for glutamine influx. This leads to the coupling of SLC1A5 with other transporters like SLC38A1, which co-transport amino acids into the cell alongside Na^+ and are also overexpressed in tumors [88, 144]. Due to their important role in glutamine metabolism, we looked for significant alterations in localization pattern of these transporters. in HCT-15 cells (**Figure 16C**). Intriguingly, glutamine starvation did not change the phenotype of transporter localization, yet V-ATPase inhibition led to an intracellular accumulation. This phenomenon potentially derives from impaired intracellular trafficking, in which the V-ATPase is particularly involved: its a1-isoform facilitates synaptic vesicle fusion and -secretion at the Golgi apparatus whereas its a2-isoform functions as pH-sensor by recruiting small GTPases in an acidification dependent manner and is involved in the formation of endolysosomal carrier vesicles [33, 89]. Accordingly, it has been shown that treatment with Bafilomycin A1 and chloroquine, which is an inhibitor of lysosomes function, both resulted in an intracellular accumulation of SLC38A2 in a panel of breast cancer cell lines, however cell line specifically [147].

Taken together, our results imply that increased uptake of alternative amino acids mediated by amino acid transporters is likely not the primary escape mechanism in our cell model.

Beyond transporters facilitating the import of amino acids from extracellular environment, Verdon et al. unraveled by radioactive [^{3}H] glutamine uptake assay in lysosomes that SLC38A7 is a lysosomal glutamine transporter, which is highly selective and capable of translocating glutamine from within the lysosomes to the cytosol where it can be fed again in glutamine metabolism. In addition, they showed that SCL38A7 is required for the growth of cancer cells under scarce glutamine conditions, when macropinocytosis and lysosomal degradation of extracellular proteins are used as an alternative nutrition route of amino acids and that it is activated dependent on acidic lysosomal pH [91]. Given that we observed an increased endocytic uptake (**Figure 17A**) and lysosomal acidification (**Figure 13**) under glutamine deprivation, we hypothesized that SLC38A7 may compensate for lacking glutamine in the cellular environment by restoring the cellular glutamine pool via the abovementioned mechanisms. As already mentioned, an upregulation of SLC38A7 mRNA expression after a combination treatment of glutamine starvation and Archazolid supported this assumption (**Figure 16A**). However, genetic ablation of the SLC38A7 gene did not lead to a beneficial outcome of concomitantly inhibiting the V-ATPase and starving the cells for glutamine in terms of cancer cell growth inhibition as well as apoptosis induction (Figure 3), meaning that SLC38A7 is presumably not responsible for the cellular adaption that prevents a synergistic effect of a combination treatment. Summarized, this emphasizes that SLC transporters, independent from whether they are located at the plasma membrane or inside the lysosomes, seem not to be responsible for cellular adaptions after glutamine deprivation and V-ATPase inhibition.

5.1.4 Metabolic plasticity by shifting from glutamine to glucose – and vice versa?

We further took metabolic reprogramming towards other fuels as a possible escape mechanism into consideration since this phenomenon has already been identified several times after targeting specific metabolic pathways. In this regard, we hypothesized that glutamine deprivation in combination with V-ATPase induces a metabolic shift towards glycolysis to sustain energy supply, cancer cell proliferation and survival. Therefore, we investigated potential alterations in glycolytic function via Seahorse platform by directly measuring the ECAR in a glycolytic stress test and thus, analyzing key parameters of glycolytic flux. Interestingly, we did not observe alterations in ECAR or glycolytic

parameters with V-ATPase inhibition alone. Yet, when cells are deprived off glutamine in combination with Archazolid treatment, they showed an elevated glycolytic rate as well as increased key parameters glycolytic capacity and glycolytic reserve, respectively, which is an indicator of the capability of cell to respond to an energetic demand (**Figure 19A,C**). In line with our results, Li et al. recently described the induction of DDIT3 (DNA damage induced transcript 3) during glutamine deprivation promoting glycolysis and ATP production via the suppression of negative glycolytic regulator TIGAR (TP53-induced glycolysis and apoptosis regulator). More precisely, the authors observed an increased ECAR upon glutamine deprivation in HepG2 cells accompanied by increased lactate secretion and enhanced glucose uptake [149] . Vice versa, Pusapati et al. found in 2016 that 2-DG-resistant glycolysis-independent PC9 and OVCAR-8 cells exhibit a significantly higher oxidative phosphorylation rate compared to their sensitive parental counterparts, which is facilitated by an increased glutamine metabolism. This means glycolysis-independent cancer cells acquired the ability to increase their oxygen consumption mediated by metabolizing glutamine as manifested by enhanced incorporation of glutamine carbon into the TCA cycle [150]. Along this line, recently it has been discovered that pancreatic cancer MiaPaCa-2 cells rather utilize glutamine as energy source than pyruvate derived from glucose, since the basal oxygen consumption rate (OCR) was found the be elevated regardless of glucose levels. Furthermore, the maximal OCR was also increased by glutamine demonstrating an enhanced glutamine metabolism under glucose depletion. Interestingly, the authors reported elevated extracellular acidification rates (ECAR) under glutamine supplementation in the presence of glucose [151].
In addition to enhanced glycolysis rates, we also found a significantly elevated hexokinase activity, which represents the first, obligatory, and rate-limiting step of glycolysis (**Figure 20B**). Similarly, Qian et al. reported an enhanced acetylation of glycolytic enzyme PGK1 (phosphoglycerate kinase 1) upon glutamine starvation or hypoxia [152].

Concluded, we provide evidence that cancer cells undergo metabolic reprogramming upon glutamine starvation and concomitant V-ATPase inhibition to circumvent proliferation inhibition and enable cell survival by shifting their metabolism towards glycolysis and thereby preventing a beneficial therapeutic effect of a combination treatment. Furthermore, this implies a notable metabolic plasticity as it seems that cancer cells can adapt their metabolism arbitrary to their needs and the given limitations. Whether other fuel routes (e.g., fatty acids) also contribute to metabolic plasticity in response to diverse therapeutic strategies remains to be elucidated and is an intriguing topic for future research.

5.2 Discussion Part II:

To date, natural compounds are still an important class of drugs in cancer medicine. Despite numerous natural products already used in tumor therapy, the need for new lead structures and drug precursors is still urgent due to rising chemoresistance of currently used anti-cancer agents [153]. In this study, we elucidated the potential of Zephycandidine A and newly synthesized analogs on their biological activity, which allowed us to identify two hit structures that had at least equivpotent antiproliferative effects as the parental structure. Surprisingly, Zephycandidine A was described to have IC_{50}-values below 10 µM in multiple cancer cell lines [22], however in our experimental setup IC_{50}-values were higher (**Figure 21**). Notably, Zhan et al. described Zephycandidine A as a colorless oil isolated from *Zephyranthes candida* [22], whereas our synthesis product is a white powder with a purity of over 99% (**Supplementary Figure 3,4**). Therefore, it is conceivable that Zephycandidine A as an isolation product from Zhan et al. might has a lower purity than the chemically synthesized version of us, since in this report no purity information have been shared and NMR spectrums are partly cut off [22]. Interestingly, also structural related alkaloids isolated from the same plant species have been reported to exhibit cytotoxicity with IC_{50}-values ranging from 0.81 µM to 13 µM in five human cancer cell lines. Thus, the colorless oil may be a potential multicomponent mixture consisting of Zephycandidine A and other alkaloids that also occur in *Zephyranthes candida* [21], which is not unusual for isolation products from natural sources and could explain observed differences in biological potency.
Apart from identifying hit structures, we sought to further determine the potential as drug candidates for our compounds. Thus, we analyzed the biological activity against non-cancerous HUVECs and observed a widened therapeutic window for THK-99 and THK-121 compared to parental structure Zephycandidine A (**Figure 21G**). In line with our findings, Zephycandidine A and other alkaloids derived from *Zephyranthes candida* have been described as selective for cancer cell lines with selectivity indices as high as 10 compared to non-cancerous human bronchial epithelial Beas-2B cells [21, 22]. However, the underlying data situation is dubious, as no data was provided by the authors on this claim.

Next, we examined the capability of Zephycandidine A and its analogs to induce cell death. In the regard to the parental structure, we observed moderate induction of cell death and no caspase-3 activation and accordingly also no PARP cleavage (**Figure 22**), whereas Zhan et al. showed by an Annexin V / Propidiumiodide co-staining that treatment of

HL-60 cells with 6 µM Zephycandidine A results in an apoptosis incidence up 80.3%, which was accompanied by abnormal morphological features pointing to apoptosis like cell shrinking. Accordingly, also significant activation of caspase-3 together with increased PARP cleavage was found upon the same treatment [22]. Appearing discrepancies with our findings, in which we did not observe such pronounced capacity to induce apoptosis, potentially could be explained again by purity issues.

In addition, with this study we provide evidence that Zephycandidine A and its analogs facilitate cell death by triggering the mitochondrial intrinsic pathway. Intriguingly, Zhan et al. described that Zephycandidine A treatment of HL-60 cells led to an upregulation of Bax as well as a downregulation of anti-apoptotic Bcl-2, already implying an involvement of mitochondria in the mediating of apoptosis [22]. In our study we were able to confirm this finding as we observed an upregulation of Bax upon treatment of Zephycandidine A and its analog THK-121 (**Figure 23A,C,D,F**). However, we investigated the impact of the parental structure and the hit structures on mitochondrial apoptosis in more detail. Particularly, we observed an upregulation of mitochondrial superoxides, mitochondrial membrane potential abrogation accompanied by a morphological alteration towards dysfunctional mitochondria and distinct upregulation of mitochondrial mass (**Figure 24-26**). Interestingly, Narva et al. have shown that Zepyhcandidine A structurally related imidazo[1,2-*f*]phenanthridine derivatives not only facilitate anti-tumoral potential by inhibiting proliferation and inducing apoptosis but rather also by inhibiting cancer cell migration [154]. Since dysfunctional mitochondria have been linked to metastasis and migration [155], investigation of the impact of Zephycandidine A and its analogs on cancer cell migration is an interesting subject for future research.

In conclusion, in this study we identified biologically active Zephycandidine A analogs that exhibit superiority as drug candidates compared to its parental structure accompanied by a functional characterization of the hit structures. Furthermore, we elucidated the impact of our compounds on mitochondria and showed that the mode of cell death induction is mediated by the intrinsic apoptotic pathways.

REFERENCES

6 References

1. Sung, H., et al., *Global Cancer Statistics 2020: GLOBOCAN Estimates of Incidence and Mortality Worldwide for 36 Cancers in 185 Countries.* CA Cancer J Clin, 2021. **71**(3): p. 209-249.
2. Newman, D.J. and G.M. Cragg, *Natural Products as Sources of New Drugs over the Nearly Four Decades from 01/1981 to 09/2019.* J Nat Prod, 2020. **83**(3): p. 770-803.
3. Koehn, F.E. and G.T. Carter, *The evolving role of natural products in drug discovery.* Nat Rev Drug Discov, 2005. **4**(3): p. 206-20.
4. Weng, J.K., R.N. Philippe, and J.P. Noel, *The rise of chemodiversity in plants.* Science, 2012. **336**(6089): p. 1667-70.
5. Wani, M.C., et al., *Plant antitumor agents. VI. The isolation and structure of taxol, a novel antileukemic and antitumor agent from Taxus brevifolia.* J Am Chem Soc, 1971. **93**(9): p. 2325-7.
6. Bhat, M.A., et al., *Myxobacteria as a Source of New Bioactive Compounds: A Perspective Study.* Pharmaceutics, 2021. **13**(8).
7. Herrmann, J., A.A. Fayad, and R. Muller, *Natural products from myxobacteria: novel metabolites and bioactivities.* Nat Prod Rep, 2017. **34**(2): p. 135-160.
8. Dawid, W., *Biology and global distribution of myxobacteria in soils.* FEMS Microbiol Rev, 2000. **24**(4): p. 403-27.
9. Munoz-Dorado, J., et al., *Myxobacteria: Moving, Killing, Feeding, and Surviving Together.* Front Microbiol, 2016. **7**: p. 781.
10. Shrivastava, A. and R.K. Sharma, *Myxobacteria and their products: current trends and future perspectives in industrial applications.* Folia Microbiol (Praha), 2021. **66**(4): p. 483-507.
11. Diez, J., et al., *Myxobacteria: natural pharmaceutical factories.* Microb Cell Fact, 2012. **11**: p. 52.
12. Wenzel, S.C. and R. Muller, *Myxobacteria--'microbial factories' for the production of bioactive secondary metabolites.* Mol Biosyst, 2009. **5**(6): p. 567-74.
13. Bollag, D.M., et al., *Epothilones, a new class of microtubule-stabilizing agents with a taxol-like mechanism of action.* Cancer Res, 1995. **55**(11): p. 2325-33.
14. Forli, S., *Epothilones: From discovery to clinical trials.* Curr Top Med Chem, 2014. **14**(20): p. 2312-21.
15. Lam, E.T., et al., *Phase I dose escalation study of KOS-1584, a novel epothilone, in patients with advanced solid tumors.* Cancer Chemother Pharmacol, 2012. **69**(2): p. 523-31.
16. Ceresa, C., et al., *Characterization of and protection from neurotoxicity induced by oxaliplatin, bortezomib and epothilone-B.* Anticancer Res, 2014. **34**(1): p. 517-23.
17. Campone, M., et al., *A double-blind, randomized phase II study to evaluate the safety and efficacy of acetyl-L-carnitine in the prevention of sagopilone-induced peripheral neuropathy.* Oncologist, 2013. **18**(11): p. 1190-1.
18. Hunt, J.T., *Discovery of ixabepilone.* Mol Cancer Ther, 2009. **8**(2): p. 275-81.
19. Pettit, G.R., et al., *Antineoplastic agents, 162. Zephyranthes candida.* J Nat Prod, 1990. **53**(1): p. 176-8.
20. Jin, Z., *Amaryllidaceae and Sceletium alkaloids.* Nat Prod Rep, 2009. **26**(3): p. 363-81.
21. Luo, Z., et al., *Cytotoxic alkaloids from the whole plants of Zephyranthes candida.* J Nat Prod, 2012. **75**(12): p. 2113-20.
22. Zhan, G., et al., *Zephycandidine A, the First Naturally Occurring Imidazo[1,2-f]phenanthridine Alkaloid from Zephyranthes candida, Exhibits Significant Anti-tumor and Anti-acetylcholinesterase Activities.* Sci Rep, 2016. **6**: p. 33990.

23. Zhan, G., et al., *Flavans with potential anti-inflammatory activities from Zephyranthes candida.* Bioorg Med Chem Lett, 2016. **26**(24): p. 5967-5970.
24. Reichenbach, H. and G. Hofle, *Biologically active secondary metabolites from myxobacteria.* Biotechnol Adv, 1993. **11**(2): p. 219-77.
25. Scheeff, S., et al., *Modular Total Synthesis of iso-Archazolids and Archazologs.* J Org Chem, 2021. **86**(15): p. 10190-10223.
26. Riviere, S., et al., *Design, Synthesis and Biological Evaluation of Highly Potent Simplified Archazolids.* ChemMedChem, 2020. **15**(14): p. 1348-1363.
27. Menche, D., et al., *Total synthesis of archazolid A.* J Am Chem Soc, 2007. **129**(19): p. 6100-1.
28. Menche, D., et al., *Modular total synthesis of archazolid A and B.* J Org Chem, 2009. **74**(19): p. 7220-9.
29. Sasse, F., et al., *Archazolids, new cytotoxic macrolactones from Archangium gephyra (Myxobacteria). Production, isolation, physico-chemical and biological properties.* J Antibiot (Tokyo), 2003. **56**(6): p. 520-5.
30. Wiedmann, R.M., et al., *The V-ATPase-inhibitor archazolid abrogates tumor metastasis via inhibition of endocytic activation of the Rho-GTPase Rac1.* Cancer Res, 2012. **72**(22): p. 5976-87.
31. Kubisch, R., et al., *V-ATPase inhibition by archazolid leads to lysosomal dysfunction resulting in impaired cathepsin B activation in vivo.* Int J Cancer, 2014. **134**(10): p. 2478-88.
32. Thomas, L., et al., *Selective upregulation of TNFalpha expression in classically-activated human monocyte-derived macrophages (M1) through pharmacological interference with V-ATPase.* Biochem Pharmacol, 2017. **130**: p. 71-82.
33. Schneider, L.S., et al., *Vacuolar-ATPase Inhibition Blocks Iron Metabolism to Mediate Therapeutic Effects in Breast Cancer.* Cancer Res, 2015. **75**(14): p. 2863-74.
34. Hirata, R., et al., *VMA11 and VMA16 encode second and third proteolipid subunits of the Saccharomyces cerevisiae vacuolar membrane H+-ATPase.* J Biol Chem, 1997. **272**(8): p. 4795-803.
35. Cotter, K., et al., *Recent Insights into the Structure, Regulation, and Function of the V-ATPases.* Trends Biochem Sci, 2015. **40**(10): p. 611-622.
36. Forgac, M., *Vacuolar ATPases: rotary proton pumps in physiology and pathophysiology.* Nat Rev Mol Cell Biol, 2007. **8**(11): p. 917-29.
37. Ohkuma, S. and B. Poole, *Fluorescence probe measurement of the intralysosomal pH in living cells and the perturbation of pH by various agents.* Proc Natl Acad Sci U S A, 1978. **75**(7): p. 3327-31.
38. Bockelmann, S., et al., *Archazolid A binds to the equatorial region of the c-ring of the vacuolar H+-ATPase.* J Biol Chem, 2010. **285**(49): p. 38304-14.
39. Sun-Wada, G.H., Y. Wada, and M. Futai, *Diverse and essential roles of mammalian vacuolar-type proton pump ATPase: toward the physiological understanding of inside acidic compartments.* Biochim Biophys Acta, 2004. **1658**(1-2): p. 106-14.
40. Settembre, C. and A. Ballabio, *Lysosomal adaptation: how the lysosome responds to external cues.* Cold Spring Harb Perspect Biol, 2014. **6**(6).
41. Bar-Peled, L. and D.M. Sabatini, *SnapShot: mTORC1 signaling at the lysosomal surface.* Cell, 2012. **151**(6): p. 1390-1390 e1.
42. Inoki, K., et al., *Rheb GTPase is a direct target of TSC2 GAP activity and regulates mTOR signaling.* Genes Dev, 2003. **17**(15): p. 1829-34.
43. Tee, A.R., et al., *Tuberous sclerosis complex gene products, Tuberin and Hamartin, control mTOR signaling by acting as a GTPase-activating protein complex toward Rheb.* Curr Biol, 2003. **13**(15): p. 1259-68.

44. Sancak, Y., et al., *The Rag GTPases bind raptor and mediate amino acid signaling to mTORC1.* Science, 2008. **320**(5882): p. 1496-501.
45. Sancak, Y., et al., *Ragulator-Rag complex targets mTORC1 to the lysosomal surface and is necessary for its activation by amino acids.* Cell, 2010. **141**(2): p. 290-303.
46. Zoncu, R., et al., *mTORC1 senses lysosomal amino acids through an inside-out mechanism that requires the vacuolar H(+)-ATPase.* Science, 2011. **334**(6056): p. 678-83.
47. Laplante, M. and D.M. Sabatini, *mTOR signaling in growth control and disease.* Cell, 2012. **149**(2): p. 274-93.
48. Ma, X.M. and J. Blenis, *Molecular mechanisms of mTOR-mediated translational control.* Nat Rev Mol Cell Biol, 2009. **10**(5): p. 307-18.
49. Popova, N.V. and M. Jucker, *The Role of mTOR Signaling as a Therapeutic Target in Cancer.* Int J Mol Sci, 2021. **22**(4).
50. Kocaturk, N.M., et al., *Autophagy as a molecular target for cancer treatment.* Eur J Pharm Sci, 2019. **134**: p. 116-137.
51. Amelio, I., G. Melino, and R.A. Knight, *Cell death pathology: cross-talk with autophagy and its clinical implications.* Biochem Biophys Res Commun, 2011. **414**(2): p. 277-81.
52. Colacurcio, D.J. and R.A. Nixon, *Disorders of lysosomal acidification-The emerging role of v-ATPase in aging and neurodegenerative disease.* Ageing Res Rev, 2016. **32**: p. 75-88.
53. Cruzat, V., et al., *Glutamine: Metabolism and Immune Function, Supplementation and Clinical Translation.* Nutrients, 2018. **10**(11).
54. Bhutia, Y.D., et al., *Amino Acid transporters in cancer and their relevance to "glutamine addiction": novel targets for the design of a new class of anticancer drugs.* Cancer Res, 2015. **75**(9): p. 1782-8.
55. Duran, R.V. and M.N. Hall, *Glutaminolysis feeds mTORC1.* Cell Cycle, 2012. **11**(22): p. 4107-8.
56. Wise, D.R. and C.B. Thompson, *Glutamine addiction: a new therapeutic target in cancer.* Trends Biochem Sci, 2010. **35**(8): p. 427-33.
57. Ahluwalia, G.S., et al., *Metabolism and action of amino acid analog anti-cancer agents.* Pharmacol Ther, 1990. **46**(2): p. 243-71.
58. Weinberg, F., et al., *Mitochondrial metabolism and ROS generation are essential for Kras-mediated tumorigenicity.* Proc Natl Acad Sci U S A, 2010. **107**(19): p. 8788-93.
59. Sappington, D.R., et al., *Glutamine drives glutathione synthesis and contributes to radiation sensitivity of A549 and H460 lung cancer cell lines.* Biochim Biophys Acta, 2016. **1860**(4): p. 836-43.
60. Muir, A., et al., *Environmental cystine drives glutamine anaplerosis and sensitizes cancer cells to glutaminase inhibition.* Elife, 2017. **6**.
61. Altman, B.J., Z.E. Stine, and C.V. Dang, *From Krebs to clinic: glutamine metabolism to cancer therapy.* Nat Rev Cancer, 2016. **16**(10): p. 619-34.
62. Jeong, S.Y. and D.W. Seol, *The role of mitochondria in apoptosis.* BMB Rep, 2008. **41**(1): p. 11-22.
63. Tait, S.W. and D.R. Green, *Mitochondria and cell death: outer membrane permeabilization and beyond.* Nat Rev Mol Cell Biol, 2010. **11**(9): p. 621-32.
64. Srinivasan, S., et al., *Mitochondrial dysfunction and mitochondrial dynamics-The cancer connection.* Biochim Biophys Acta Bioenerg, 2017. **1858**(8): p. 602-614.
65. Suen, D.F., K.L. Norris, and R.J. Youle, *Mitochondrial dynamics and apoptosis.* Genes Dev, 2008. **22**(12): p. 1577-90.

66. Kogot-Levin, A., et al., *Upregulation of Mitochondrial Content in Cytochrome c Oxidase Deficient Fibroblasts.* PLoS One, 2016. **11**(10): p. e0165417.
67. von Schwarzenberg, K., et al., *Mode of cell death induction by pharmacological vacuolar H+-ATPase (V-ATPase) inhibition.* J Biol Chem, 2013. **288**(2): p. 1385-96.
68. Bartel, K., et al., *Connecting lysosomes and mitochondria - a novel role for lipid metabolism in cancer cell death.* submitted, 2019.
69. Nicoletti, I., et al., *A rapid and simple method for measuring thymocyte apoptosis by propidium iodide staining and flow cytometry.* J Immunol Methods, 1991. **139**(2): p. 271-9.
70. Robey, R.W., et al., *Inhibition of P-glycoprotein (ABCB1)- and multidrug resistance-associated protein 1 (ABCC1)-mediated transport by the orally administered inhibitor, CBT-1((R)).* Biochem Pharmacol, 2008. **75**(6): p. 1302-12.
71. Koczian, F., et al., *Targeting the endoplasmic reticulum-mitochondria interface sensitizes leukemia cells to cytostatics.* Haematologica, 2019. **104**(3): p. 546-555.
72. Ehrhardt, H., et al., *Optimized anti-tumor effects of anthracyclines plus Vinca alkaloids using a novel, mechanism-based application schedule.* Blood, 2011. **118**(23): p. 6123-31.
73. Bradford, M.M., *A rapid and sensitive method for the quantitation of microgram quantities of protein utilizing the principle of protein-dye binding.* Anal Biochem, 1976. **72**: p. 248-54.
74. Fleige, S., et al., *Comparison of relative mRNA quantification models and the impact of RNA integrity in quantitative real-time RT-PCR.* Biotechnol Lett, 2006. **28**(19): p. 1601-13.
75. Stransky, L.A. and M. Forgac, *Amino Acid Availability Modulates Vacuolar H+-ATPase Assembly.* J Biol Chem, 2015. **290**(45): p. 27360-27369.
76. Mauvezin, C. and T.P. Neufeld, *Bafilomycin A1 disrupts autophagic flux by inhibiting both V-ATPase-dependent acidification and Ca-P60A/SERCA-dependent autophagosome-lysosome fusion.* Autophagy, 2015. **11**(8): p. 1437-8.
77. Wang, R., et al., *Molecular basis of V-ATPase inhibition by bafilomycin A1.* Nat Commun, 2021. **12**(1): p. 1782.
78. Hooper, K.M., et al., *V-ATPase is a universal regulator of LC3-associated phagocytosis and non-canonical autophagy.* J Cell Biol, 2022. **221**(6).
79. Fares, H.M., et al., *Autophagy in cancer: The cornerstone during glutamine deprivation.* Eur J Pharmacol, 2022. **916**: p. 174723.
80. Tanida, I., T. Ueno, and E. Kominami, *LC3 and Autophagy.* Methods Mol Biol, 2008. **445**: p. 77-88.
81. Hardie, D.G., F.A. Ross, and S.A. Hawley, *AMPK: a nutrient and energy sensor that maintains energy homeostasis.* Nat Rev Mol Cell Biol, 2012. **13**(4): p. 251-62.
82. Li, Y. and Y. Chen, *AMPK and Autophagy.* Adv Exp Med Biol, 2019. **1206**: p. 85-108.
83. Martina, J.A., et al., *MTORC1 functions as a transcriptional regulator of autophagy by preventing nuclear transport of TFEB.* Autophagy, 2012. **8**(6): p. 903-14.
84. Schiliro, C. and B.L. Firestein, *Mechanisms of Metabolic Reprogramming in Cancer Cells Supporting Enhanced Growth and Proliferation.* Cells, 2021. **10**(5).
85. van Geldermalsen, M., et al., *ASCT2/SLC1A5 controls glutamine uptake and tumour growth in triple-negative basal-like breast cancer.* Oncogene, 2016. **35**(24): p. 3201-8.
86. Fuchs, B.C., et al., *ASCT2 silencing regulates mammalian target-of-rapamycin growth and survival signaling in human hepatoma cells.* Am J Physiol Cell Physiol, 2007. **293**(1): p. C55-63.

87. Shimizu, K., et al., *ASC amino-acid transporter 2 (ASCT2) as a novel prognostic marker in non-small cell lung cancer.* Br J Cancer, 2014. **110**(8): p. 2030-9.
88. Broer, A., F. Rahimi, and S. Broer, *Deletion of Amino Acid Transporter ASCT2 (SLC1A5) Reveals an Essential Role for Transporters SNAT1 (SLC38A1) and SNAT2 (SLC38A2) to Sustain Glutaminolysis in Cancer Cells.* J Biol Chem, 2016. **291**(25): p. 13194-205.
89. Marshansky, V. and M. Futai, *The V-type H+-ATPase in vesicular trafficking: targeting, regulation and function.* Curr Opin Cell Biol, 2008. **20**(4): p. 415-26.
90. Pavlova, N.N. and C.B. Thompson, *The Emerging Hallmarks of Cancer Metabolism.* Cell Metab, 2016. **23**(1): p. 27-47.
91. Verdon, Q., et al., *SNAT7 is the primary lysosomal glutamine exporter required for extracellular protein-dependent growth of cancer cells.* Proc Natl Acad Sci U S A, 2017. **114**(18): p. E3602-E3611.
92. Wu, M., et al., *Multiparameter metabolic analysis reveals a close link between attenuated mitochondrial bioenergetic function and enhanced glycolysis dependency in human tumor cells.* Am J Physiol Cell Physiol, 2007. **292**(1): p. C125-36.
93. Mookerjee, S.A., et al., *The contributions of respiration and glycolysis to extracellular acid production.* Biochim Biophys Acta, 2015. **1847**(2): p. 171-181.
94. Wang, C. and R.J. Youle, *The role of mitochondria in apoptosis*.* Annu Rev Genet, 2009. **43**: p. 95-118.
95. Brentnall, M., et al., *Caspase-9, caspase-3 and caspase-7 have distinct roles during intrinsic apoptosis.* BMC Cell Biol, 2013. **14**: p. 32.
96. Sairanen, T., et al., *Neuronal caspase-3 and PARP-1 correlate differentially with apoptosis and necrosis in ischemic human stroke.* Acta Neuropathol, 2009. **118**(4): p. 541-52.
97. Ashkenazi, A. and G. Salvesen, *Regulated cell death: signaling and mechanisms.* Annu Rev Cell Dev Biol, 2014. **30**: p. 337-56.
98. MacEwan, D.J., *TNF ligands and receptors--a matter of life and death.* Br J Pharmacol, 2002. **135**(4): p. 855-75.
99. Zhou, X., et al., *Virus Infection and Death Receptor-Mediated Apoptosis.* Viruses, 2017. **9**(11).
100. Fulda, S., et al., *Cellular stress responses: cell survival and cell death.* Int J Cell Biol, 2010. **2010**: p. 214074.
101. Aggarwal, V., et al., *Role of Reactive Oxygen Species in Cancer Progression: Molecular Mechanisms and Recent Advancements.* Biomolecules, 2019. **9**(11).
102. Michels, J., P.W. Johnson, and G. Packham, *Mcl-1.* Int J Biochem Cell Biol, 2005. **37**(2): p. 267-71.
103. McArthur, K., et al., *BAK/BAX macropores facilitate mitochondrial herniation and mtDNA efflux during apoptosis.* Science, 2018. **359**(6378).
104. Buytaert, E., et al., *Deficiency in apoptotic effectors Bax and Bak reveals an autophagic cell death pathway initiated by photodamage to the endoplasmic reticulum.* Autophagy, 2006. **2**(3): p. 238-40.
105. Wu, S., et al., *Mitochondrial oxidative stress causes mitochondrial fragmentation via differential modulation of mitochondrial fission-fusion proteins.* FEBS J, 2011. **278**(6): p. 941-54.
106. Picard, M., et al., *Mitochondrial morphology transitions and functions: implications for retrograde signaling?* Am J Physiol Regul Integr Comp Physiol, 2013. **304**(6): p. R393-406.
107. Warburg, O., *On the origin of cancer cells.* Science, 1956. **123**(3191): p. 309-14.
108. Hanahan, D. and R.A. Weinberg, *Hallmarks of cancer: the next generation.* Cell, 2011. **144**(5): p. 646-74.

109. DeBerardinis, R.J. and T. Cheng, *Q's next: the diverse functions of glutamine in metabolism, cell biology and cancer.* Oncogene, 2010. **29**(3): p. 313-24.
110. Kovacevic, Z., *The pathway of glutamine and glutamate oxidation in isolated mitochondria from mammalian cells.* Biochem J, 1971. **125**(3): p. 757-63.
111. Eagle, H., *Nutrition needs of mammalian cells in tissue culture.* Science, 1955. **122**(3168): p. 501-14.
112. Ballabio, A. and J.S. Bonifacino, *Lysosomes as dynamic regulators of cell and organismal homeostasis.* Nat Rev Mol Cell Biol, 2020. **21**(2): p. 101-118.
113. Xiong, J., et al., *Glutamine Produces Ammonium to Tune Lysosomal pH and Regulate Lysosomal Function.* Cells, 2022. **12**(1).
114. Hart, P.D. and M.R. Young, *Ammonium chloride, an inhibitor of phagosome-lysosome fusion in macrophages, concurrently induces phagosome-endosome fusion, and opens a novel pathway: studies of a pathogenic mycobacterium and a nonpathogenic yeast.* J Exp Med, 1991. **174**(4): p. 881-9.
115. Korolchuk, V.I., et al., *Lysosomal positioning coordinates cellular nutrient responses.* Nat Cell Biol, 2011. **13**(4): p. 453-60.
116. Mundy, D.I., et al., *Caveolin targeting to late endosome/lysosomal membranes is induced by perturbations of lysosomal pH and cholesterol content.* Mol Biol Cell, 2012. **23**(5): p. 864-80.
117. Li, J., et al., *Synthetic lethality of glutaminolysis inhibition, autophagy inactivation and asparagine depletion in colon cancer.* Oncotarget, 2017. **8**(26): p. 42664-42672.
118. Yamamoto, A., et al., *Bafilomycin A1 prevents maturation of autophagic vacuoles by inhibiting fusion between autophagosomes and lysosomes in rat hepatoma cell line, H-4-II-E cells.* Cell Struct Funct, 1998. **23**(1): p. 33-42.
119. Yuan, N., et al., *Bafilomycin A1 targets both autophagy and apoptosis pathways in pediatric B-cell acute lymphoblastic leukemia.* Haematologica, 2015. **100**(3): p. 345-56.
120. Bodineau, C., et al., *Two parallel pathways connect glutamine metabolism and mTORC1 activity to regulate glutamoptosis.* Nat Commun, 2021. **12**(1): p. 4814.
121. Bartel, K., R. Muller, and K. von Schwarzenberg, *Differential regulation of AMP-activated protein kinase in healthy and cancer cells explains why V-ATPase inhibition selectively kills cancer cells.* J Biol Chem, 2019. **294**(46): p. 17239-17248.
122. Farber, S. and L.K. Diamond, *Temporary remissions in acute leukemia in children produced by folic acid antagonist, 4-aminopteroyl-glutamic acid.* N Engl J Med, 1948. **238**(23): p. 787-93.
123. Luengo, A., D.Y. Gui, and M.G. Vander Heiden, *Targeting Metabolism for Cancer Therapy.* Cell Chem Biol, 2017. **24**(9): p. 1161-1180.
124. Vanhove, K., et al., *Glutamine Addiction and Therapeutic Strategies in Lung Cancer.* Int J Mol Sci, 2019. **20**(2).
125. Son, J., et al., *Glutamine supports pancreatic cancer growth through a KRAS-regulated metabolic pathway.* Nature, 2013. **496**(7443): p. 101-5.
126. Petronini, P.G., et al., *Cell susceptibility to apoptosis by glutamine deprivation and rescue: survival and apoptotic death in cultured lymphoma-leukemia cell lines.* J Cell Physiol, 1996. **169**(1): p. 175-85.
127. Halama, A. and K. Suhre, *Advancing Cancer Treatment by Targeting Glutamine Metabolism-A Roadmap.* Cancers (Basel), 2022. **14**(3).
128. Seltzer, M.J., et al., *Inhibition of glutaminase preferentially slows growth of glioma cells with mutant IDH1.* Cancer Res, 2010. **70**(22): p. 8981-7.

129. Yu, D., et al., *Kidney-type glutaminase (GLS1) is a biomarker for pathologic diagnosis and prognosis of hepatocellular carcinoma.* Oncotarget, 2015. **6**(10): p. 7619-31.
130. Xu, L., et al., *A glutaminase isoform switch drives therapeutic resistance and disease progression of prostate cancer.* Proc Natl Acad Sci U S A, 2021. **118**(13).
131. Xiang, Y., et al., *Targeted inhibition of tumor-specific glutaminase diminishes cell-autonomous tumorigenesis.* J Clin Invest, 2015. **125**(6): p. 2293-306.
132. Choi, Y.K. and K.G. Park, *Targeting Glutamine Metabolism for Cancer Treatment.* Biomol Ther (Seoul), 2018. **26**(1): p. 19-28.
133. Chen, L. and H. Cui, *Targeting Glutamine Induces Apoptosis: A Cancer Therapy Approach.* Int J Mol Sci, 2015. **16**(9): p. 22830-55.
134. Erickson, J.W. and R.A. Cerione, *Glutaminase: a hot spot for regulation of cancer cell metabolism?* Oncotarget, 2010. **1**(8): p. 734-40.
135. Gross, M.I., et al., *Antitumor activity of the glutaminase inhibitor CB-839 in triple-negative breast cancer.* Mol Cancer Ther, 2014. **13**(4): p. 890-901.
136. Liu, H.Y., et al., *GLS1 depletion inhibited colorectal cancer proliferation and migration via redox/Nrf2/autophagy-dependent pathway.* Arch Biochem Biophys, 2021. **708**: p. 108964.
137. Yuan, L., et al., *Glutaminase inhibitor compound 968 inhibits cell proliferation and sensitizes paclitaxel in ovarian cancer.* Am J Transl Res, 2016. **8**(10): p. 4265-4277.
138. Halama, A., et al., *Accelerated lipid catabolism and autophagy are cancer survival mechanisms under inhibited glutaminolysis.* Cancer Lett, 2018. **430**: p. 133-147.
139. Ruiz-Rodado, V., et al., *Metabolic plasticity of IDH1-mutant glioma cell lines is responsible for low sensitivity to glutaminase inhibition.* Cancer Metab, 2020. **8**: p. 23.
140. Hamm, R., et al., *Resistance mechanisms of cancer cells to the novel vacuolar H(+)-ATPase inhibitor archazolid B.* Invest New Drugs, 2014. **32**(5): p. 893-903.
141. Bradshaw-Pierce, E.L., et al., *Tumor P-Glycoprotein Correlates with Efficacy of PF-3758309 in in vitro and in vivo Models of Colorectal Cancer.* Front Pharmacol, 2013. **4**: p. 22.
142. Seo, J.W., et al., *Autophagy is required for PDAC glutamine metabolism.* Sci Rep, 2016. **6**: p. 37594.
143. Liu, X., *SLC Family Transporters.* Adv Exp Med Biol, 2019. **1141**: p. 101-202.
144. Bhutia, Y.D. and V. Ganapathy, *Glutamine transporters in mammalian cells and their functions in physiology and cancer.* Biochim Biophys Acta, 2016. **1863**(10): p. 2531-9.
145. Zhang, N., et al., *Increased Amino Acid Uptake Supports Autophagy-Deficient Cell Survival upon Glutamine Deprivation.* Cell Rep, 2018. **23**(10): p. 3006-3020.
146. Lowman, X.H., et al., *p53 Promotes Cancer Cell Adaptation to Glutamine Deprivation by Upregulating Slc7a3 to Increase Arginine Uptake.* Cell Rep, 2019. **26**(11): p. 3051-3060 e4.
147. Morotti, M., et al., *Increased expression of glutamine transporter SNAT2/SLC38A2 promotes glutamine dependence and oxidative stress resistance, and is associated with worse prognosis in triple-negative breast cancer.* Br J Cancer, 2021. **124**(2): p. 494-505.
148. Liu, Y., et al., *The role of ASCT2 in cancer: A review.* Eur J Pharmacol, 2018. **837**: p. 81-87.
149. Li, M., et al., *DDIT3 Directs a Dual Mechanism to Balance Glycolysis and Oxidative Phosphorylation during Glutamine Deprivation.* Adv Sci (Weinh), 2021. **8**(11): p. e2003732.

150. Pusapati, R.V., et al., *mTORC1-Dependent Metabolic Reprogramming Underlies Escape from Glycolysis Addiction in Cancer Cells.* Cancer Cell, 2016. **29**(4): p. 548-562.
151. Yoo, H.C., et al., *A Variant of SLC1A5 Is a Mitochondrial Glutamine Transporter for Metabolic Reprogramming in Cancer Cells.* Cell Metab, 2020. **31**(2): p. 267-283 e12.
152. Qian, X., X. Li, and Z. Lu, *Protein kinase activity of the glycolytic enzyme PGK1 regulates autophagy to promote tumorigenesis.* Autophagy, 2017. **13**(7): p. 1246-1247.
153. Emran, T.B., et al., *Multidrug Resistance in Cancer: Understanding Molecular Mechanisms, Immunoprevention and Therapeutic Approaches.* Front Oncol, 2022. **12**: p. 891652.
154. Narva, S., et al., *Synthesis of imidazo[1,2-f]phenanthridine derivatives under a metal- and base-free condition and their anticancer activity.* Tetrahedron Letters, 2021. **68**: p. 152908.
155. Poole, L.P. and K.F. Macleod, *Mitophagy in tumorigenesis and metastasis.* Cell Mol Life Sci, 2021. **78**(8): p. 3817-3851.

APPENDIX

7 Appendix

7.1 Supplementary figures

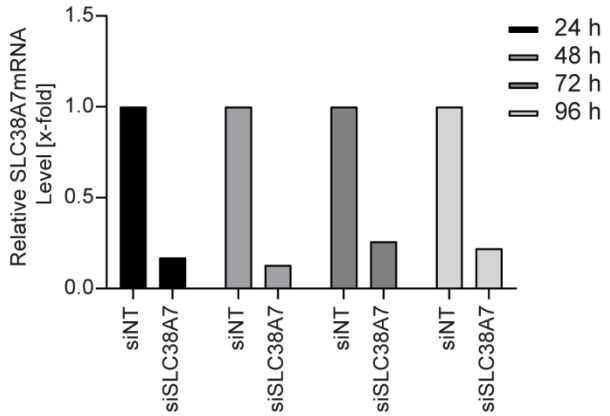

Supplementary Figure 1: Transfection control of SLC38A7 knockdown.
The expression of SLC38A7 was analyzed by qPCR after the indicated times of knockdown.

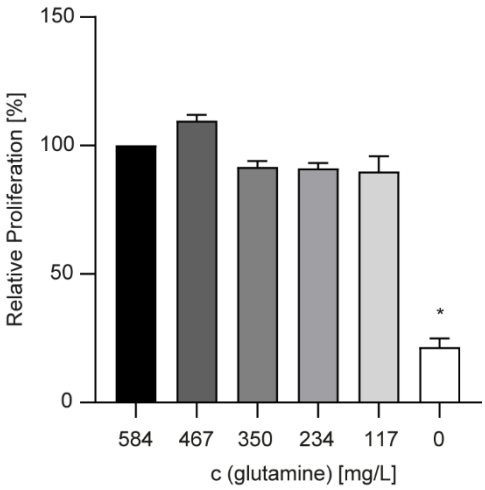

Supplementary Figure 2: Determination of glutamine(low) conditions.
Relative proliferation was determined in HCT-15 cells by crystal violet staining. Cells were treated as indicated for 72 h. Bar graphs display relative proliferation normalized to full medium control (584 mg/L), mean ± SEM (n=3), One-way ANOVA followed by Dunnett´s multiple comparison test, *p<0.05.

Chromatogram and Results

Injection Details

Injection Name:	**THK 93-1**	*Run Time (min):*	**9,99**
Vial Number:	**Vial:92**	*Injection Volume:*	**10,00 µL**
Injection Type:	**Unknown**	*Wavelength:*	**210 nm**
Instrument Method:	**Horst 50 ACN 50 Puffer 210nm**	*Flow rate:*	**1,0 ml/min**
Column:	**Zorbax Eclipse Plus C18 4,6x 150mm, 5µm**	*Column Temperatur:*	**50,0 °C**
Injection Date/Time:	**22.Jun.21 13:56**		
Pump Channel A:	**50 ACN**		
Pump Channel B:			
Pump ChannelC:	**50 Puffer pH 4**		
Pump Channel D:			

Chromatogram

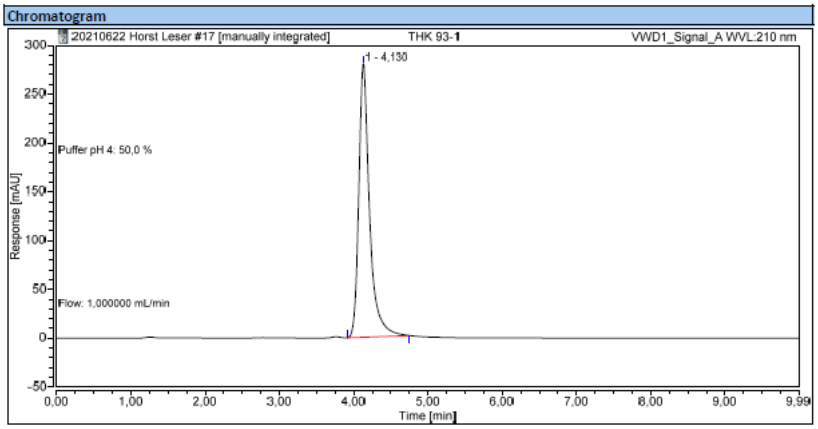

Integration Results

No.	etention Tin min	Area mAU*min	Relative Area %
1	4,130	46,846	100,00
Total:		**46,846**	**100,00**

Supplementary Figure 3: Purity testing of Zephycandidine A via HPLC at a wavelength of 210 nm. Purity test performed by Thomas Klaßmüller.

Chromatogram and Results

Injection Details

Injection Name:	**THK 93-1**	*Run Time (min):*	**9,99**
Vial Number:	**Vial:92**	*Injection Volume:*	**10,00 µL**
Injection Type:	**Unknown**	*Wavelength:*	**254 nm**
Instrument Method:	**Horst 50 ACN 50 Puffer 254nm**	*Flow rate:*	**1,0 ml/min**
Column:	**Zorbax Eclipse Plus C18 4,6x 150mm, 5µm**	*Column Temperatur:*	**50,0 °C**
Injection Date/Time:	**22.Jun.21 14:07**		
Pump Channel A:	**50 ACN**		
Pump Channel B:			
Pump ChannelC:	**50 Puffer pH 4**		
Pump Channel D:			

Chromatogram

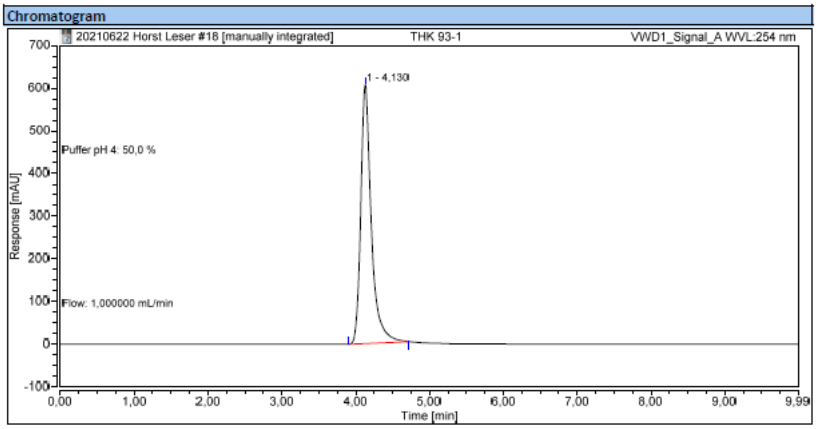

Integration Results

No.	etention Tin min	Area mAU*min	Relative Area %
1	4,130	100,039	100,00
Total:		**100,039**	**100,00**

Supplementary Figure 4: Purity testing of Zephycandidine A via HPLC at a wavelength of 254 nm. Purity test performed by Thomas Klaßmüller.

7.2 Supplementary tables

HCT-15									
Target	**Gln(+) - vs. Gln(+) Arch 1 nM**	**Gln(+) - vs. Gln(+) Arch 10 nM**	**Gln(+) Arch 1 nM vs. Gln(+) Arch 10 nM**	**Gln(-) - vs. Gln(-) Arch 1 nM**	**Gln(-) - vs. Gln(-) Arch 10 nM**	**Gln(-) Arch 1 nM vs. Gln(-) Arch 10 nM**	**Gln(+) - vs. Gln(-) -**	**Gln(+) Arch 1 nM vs. Gln(-) Arch 1 nM**	**Gln(+) Arch 10 nM vs. Gln(-) Arch 10 nM**
SLC38A1	ns	ns	ns	ns	ns	ns	ns	ns	*
SLC38A2	ns	ns	ns	ns	ns	ns	*	*	*
SLC38A5	ns	ns	ns	ns	ns	ns	ns	ns	ns
SLC38A7	ns	ns	ns	ns	*	*	ns	ns	*
SLC38A8	ns	ns	ns	ns	ns	ns	*	*	*
SLC38A9	ns	ns	ns	ns	ns	ns	ns	ns	ns
SLC38A10	ns	*	*	ns	ns	ns	*	*	ns
SLC1A5	ns	ns	ns	ns	ns	ns	*	*	ns
BxPC-3									
Target	**Gln(+) - vs. Gln(+) Arch 1 nM**	**Gln(+) - vs. Gln(+) Arch 10 nM**	**Gln(+) Arch 1 nM vs. Gln(+) Arch 10 nM**	**Gln(-) - vs. Gln(-) Arch 1 nM**	**Gln(-) - vs. Gln(-) Arch 10 nM**	**Gln(-) Arch 1 nM vs. Gln(-) Arch 10 nM**	**Gln(+) - vs. Gln(-) -**	**Gln(+) Arch 1 nM vs. Gln(-) Arch 1 nM**	**Gln(+) Arch 10 nM vs. Gln(-) Arch 10 nM**
SLC38A1	ns	ns	ns	ns	ns	ns	ns	ns	ns
SLC38A2	ns	ns	ns	ns	ns	ns	ns	ns	ns
SLC38A5	ns	*	ns	ns	ns	ns	*	ns	ns
SLC38A7	ns	ns	ns	ns	*	ns	*	ns	ns
SLC38A8	n.a.	n.a.	n.a.	n.a.	n.a.	n.a.	n.a.	n.a.	n.a.
SLC38A9	ns	ns	ns	ns	ns	ns	ns	ns	*
SLC38A10	ns	ns	ns	ns	ns	ns	*	ns	ns
SLC1A5	ns	ns	ns	ns	*	*	ns	ns	*

Supplementary Table 1: Statistical evaluation of Figure 16

HCT-15									
Target	**Gln(+) - vs. Gln(+) Arch 1 nM**	**Gln(+) - vs. Gln(+) Arch 10 nM**	**Gln(+) Arch 1 nM vs. Gln(+) Arch 10 nM**	**Gln(-) - vs. Gln(-) Arch 1 nM**	**Gln(-) - vs. Gln(-) Arch 10 nM**	**Gln(-) Arch 1 nM vs. Gln(-) Arch 10 nM**	**Gln(+) - vs. Gln(-) -**	**Gln(+) Arch 1 nM vs. Gln(-) Arch 1 nM**	**Gln(+) Arch 10 nM vs. Gln(-) Arch 10 nM**
GLUL	ns	ns	ns	ns	ns	ns	ns	*	*
GLS1	ns	ns	ns	ns	ns	*	ns	ns	*
GLS2	ns	ns	ns	ns	ns	ns	ns	ns	ns
GOT1	ns	ns	*	ns	ns	ns	*	*	*
GOT2	ns	ns	ns	ns	ns	ns	ns	ns	ns
GDH1	ns	ns	ns	ns	ns	ns	ns	ns	ns
GDH2	ns	ns	ns	ns	ns	ns	ns	ns	ns
GPT2	ns	ns	ns	ns	ns	ns	*	*	*
BxPC-3									
Target	**Gln(+) - vs. Gln(+) Arch 1 nM**	**Gln(+) - vs. Gln(+) Arch 10 nM**	**Gln(+) Arch 1 nM vs. Gln(+) Arch 10 nM**	**Gln(-) - vs. Gln(-) Arch 1 nM**	**Gln(-) - vs. Gln(-) Arch 10 nM**	**Gln(-) Arch 1 nM vs. Gln(-) Arch 10 nM**	**Gln(+) - vs. Gln(-) -**	**Gln(+) Arch 1 nM vs. Gln(-) Arch 1 nM**	**Gln(+) Arch 10 nM vs. Gln(-) Arch 10 nM**
GLUL	ns	ns	ns	ns	*	*	ns	ns	ns
GLS1	ns	ns	ns	ns	ns	ns	ns	ns	ns
GLS2	ns	ns	ns	ns	ns	ns	ns	ns	ns
GOT1	ns	ns	ns	ns	ns	*	ns	ns	ns
GOT2	ns	ns	ns	ns	ns	ns	ns	ns	ns
GDH1	ns	ns	ns	ns	*	*	ns	ns	ns
GDH2	ns	ns	ns	ns	ns	ns	ns	ns	ns
GPT2	ns	ns	ns	ns	ns	ns	*	*	*

Supplementary Table 2: Statistical evaluation of Figure 18

HCT-15									
Target	**Gln(+) - vs. Gln(+) Arch 1 nM**	**Gln(+) - vs. Gln(+) Arch 10 nM**	**Gln(+) Arch 1 nM vs. Gln(+) Arch 10 nM**	**Gln(-) - vs. Gln(-) Arch 1 nM**	**Gln(-) - vs. Gln(-) Arch 10 nM**	**Gln(-) Arch 1 nM vs. Gln(-) Arch 10 nM**	**Gln(+) - vs. Gln(-) -**	**Gln(+) Arch 1 nM vs. Gln(-) Arch 1 nM**	**Gln(+) Arch 10 nM vs. Gln(-) Arch 10 nM**
Hexo-kinase I	ns	ns	ns	ns	ns	ns	ns	ns	ns
Hexo-kinase II	ns	ns	ns	ns	ns	ns	ns	ns	ns
GAPDH	ns	ns	ns	ns	ns	ns	ns	ns	ns
LDHA	ns	ns	ns	ns	ns	ns	ns	ns	ns
PFKP	ns	ns	ns	ns	ns	ns	ns	ns	ns
PKM1/2	ns	ns	ns	ns	ns	ns	ns	ns	ns
PKM2	ns	ns	ns	ns	ns	ns	ns	ns	ns
Pyruvate Dehydro-genase	ns	ns	ns	ns	ns	ns	ns	ns	ns
BxPC-3									
Target	**Gln(+) - vs. Gln(+) Arch 1 nM**	**Gln(+) - vs. Gln(+) Arch 10 nM**	**Gln(+) Arch 1 nM vs. Gln(+) Arch 10 nM**	**Gln(-) - vs. Gln(-) Arch 1 nM**	**Gln(-) - vs. Gln(-) Arch 10 nM**	**Gln(-) Arch 1 nM vs. Gln(-) Arch 10 nM**	**Gln(+) - vs. Gln(-) -**	**Gln(+) Arch 1 nM vs. Gln(-) Arch 1 nM**	**Gln(+) Arch 10 nM vs. Gln(-) Arch 10 nM**
Hexo-kinase I	ns	ns	ns	ns	ns	ns	ns	ns	ns
Hexo-kinase II	ns	ns	ns	ns	ns	ns	ns	ns	ns
GAPDH	ns	ns	ns	ns	ns	ns	ns	ns	ns
LDHA	ns	ns	ns	ns	ns	ns	ns	ns	ns
PFKP	ns	ns	ns	ns	ns	ns	ns	ns	ns
PKM1/2	ns	ns	ns	ns	ns	ns	ns	ns	ns
PKM2	ns	ns	ns	ns	ns	ns	ns	ns	ns
Pyruvate Dehydro-genase	ns	ns	ns	ns	ns	ns	ns	ns	ns

Supplementary Table 3: Statistical evaluation of Figure 20

7.3 Abbreviations

Abbreviation	Term
ΔΨm	Mitochondrial membrane potential
2-DG	2-deoxy-D-glucose
α-KG	Alpha-ketoglutarate
AChE	Acetylcholinesterase
Act.	Active
ADP	Adenoside 5'-diphosphate
Akt	Protein kinase B
ALL	Akute lymphoblastic leukemia
AMPKα	AMP activated protein kinase alpha
ANOVA	Analysis of variance between groups
APS	Ammonium persulfate
Arch	Archazolid
ATCC	American type culture collection
atg	Autophagy related
ATP	Adenoside 5'-triphosphate
Bak	Bcl-2 homologous antagonist killer
Bax	Bcl-2-associated X protein
Bcl-2	B-cell lymphoma 2
Bcl-xl	B-cell lymphoma extra large
BH-3 only	B-cell lymphoma 2 (Bcl-2) homology 3
BPTES	bis-2-(5-phenylacetamido-1,3,4-thiadiazol-2-yl)ethyl sulfide
BSA	Bovine serum albumin
Cas-3	Caspase-3
CCCP	Carbonylcyanid-m-chlorphenylhydrazon
cDNA	Complementary DNA
CO_2	Carbon dioxide
CoA	Coenzyme A
Co. KG	Compagnie Kommanditgesellschaft
DEP	Dishevelled, Egl-10 and Pleckstrin
DEPTOR	DEP domain-containing mTOR-interacting protein
DDIT3	DNA damage induced transcript 3
DMEM	Dulbecco's Modified Eagle Medium
DMSO	Dimethyl sulfoxide
DMSZ	Deutsche Sammlung von Mikroorganismen und Zellkulturen
DNA	Deoxyribonucleic acid
DTT	1,4-dithiothreitol
ECAR	Extracellular Acidification Rate

Abbreviation	Term
ECGM	Endothelial Cell Growth Medium
ECL	Enhanced chemiluminescence
EDTA	Ethylenediaminetetraacetic acid
eIF4E	Eukaryotic translation initiation factor 4E
e.g.	Example given
FACS	Fluorescence activated cell sorting
FCS	Fetal calf serum
FDA	Federal drug agency
FITC	Fluorescein isothiocyanate
FSC	Forwards scatter
FW	Forward
GAPDH	Glyceraldehyde 3-phosphate dehydrogenase
GmbH	Gesellschaft mit beschränkter Haftung
gMFI	Geometric mean of fluorescence intensity
GDH	Glutamatedyhrogenase
GDP	Guanosin diphosphate
Gln	Glutamine
GLS	Glutaminase
Glu	Glutamate
GLUL	Glutamine synthetase
GOT	Glutamate-oxalacetate transaminase
GPT	Glutamate-pyruvate transaminase
GTP	Guanosin triphosphate
HPLC	High performance liquid chromatography
H_2O	Water
H_2O_2	Hydrogen peroxide
HBSS	Hank´s balanced salt solution
HFS	Hypotonic fluorochrome solution
H+L	Heavy and light (chain)
HRP	Horseradish peroxide
IC_{50}	Half maximal inhibitory concentration
IgG	Immunoglobulin G
JC-1	Tetraethylbenzimidazolylcarbocyanine iodide
KGaA	Kommanditgesellschaft auf Aktien
LC3	Microtubule-associated protein 1A/1B-light chain 3
LDHA	Lactate dehydrogenase A
log	Logarithm to base ten
LYNUS	Lysosomal nutrient sensing
Mcl-1	Induced myeloid leukemia cell differentiation protein

Abbreviation	Term
mLST8	Mammalian lethal with SEC13 protein 8
MOMP	Mitochondrial outer membrane permeabilization
mRNA	Messenger RNA
mTOR(C)	Mechanistic target of rapamycin (complex)
n.a.	Not available
NADH	Nicotinamide adenine dinucleotide hydrogen
NADPH	Nicotinamide adenine dinucleotide phosphate hydrogen
NEAA	Non-essential amino acids
NP-40	Octoxinol 9
ns	Not significant
NT	Non-targeting
OAA	Oxaloacetic acid
OCR	Oxygen Consumption Rate
P70S6K	Ribosomal protein S6 kinase beta-1
PAGE	polyacrylamide gel electrophoresis
PBS	Phosphate-buffered saline
PE	Phycoerythrin
PGK1	Phosphoglycerate kinase 1
PFKP	Phosphofructokinase platelet
PKM	Pyruvate kinase M
P-gp	P-glycoprotein
PI3K	Phosphoinositid-3-kinase
PMT	Photomultiplier
P	Phosphate
PCR	Polymerase chain reaction
PARP	Poly (ADP-ribose) polymerase
PFA	Paraformaldehyde
PMSF	Phenylmethylsulfonyl fluoride
PVDF	Polyvinylidene difluoride
qPCR	Quantitative real-time PCR
RAPTOR	Regulatory-associated protein of mTOR
RAS	Rat sarcoma
Rheb	RAS homolog enriched in brain
ROS	Reactive oxygen species
RNA	Ribonucleic acid
RPMI-1640	Roswell Park Memorial Institute Medium 1640
RV	Reverse
SDS	Sodium dodecyl sulfate
SEM	Standard error of mean

Abbreviation	Term
siRNA	Small interfering RNA
SLC	Solute carrier
SSC	Sideward scatter
STR	Short tandem repeat
TBS-T	Tris-buffered saline + Tween20
TCA	Tricarboxylic acid
TCE	Trichloroethanol
T/E	Trypsin/ethylenediaminetetraacetic acid
Thr	Threonine
TIGAR	TP53-induced glycolysis and apoptosis regulator
TEMED	Tetramethylethylenediamine
Tris	Tris(hydroxymethyl)aminomethane
ULK1	UNC-51-like kinase 1
USA	United States of America
V-ATPase	Vacuolar-type H^+ ATPase
XF	Extracellular Flux
ZephA	Zephycandidine A

Table 25: List of abbreviations

7.4 Symbols and units

Symbol/Unit	Term
%	Percent
% (m/m)	Mass percent
% (v/m)	Volume percent
°C	Degree Celsius
µg	Microgram [10^{-6} g]
µL	Microliter [10^{-6} L]
µm	Micrometer [10^{-6} m]
µM	Micromolar [10^{-6} M]
cm^2	Square centimeter
g	Gravity
h	Hour(s)
kDa	Kilodalton
M	Molar concentration
min	Minute(s)
mL	Milliliter [10^{-3} L]
mm	Millimeter [10^{-3} m]
mM	Millimolar [10^{-3} M]
nm	Nanometer [10^{-9} m]
nM	Nanomolar [10^{-9} M]
nmol	Nanomoles
pmol	Picomoles
V	Volt
®	Registered Trademark
™	Trademark
α	Alpha

Table 26: Symbols and units

7.5 Index of figures

7.6 Index of tables

7.7 List of publications and conference contributions

7.7.1 Research articles

i. A metabolic shift toward glycolysis enables cancer cells to maintain survival upon concomitant glutamine deprivation and V-ATPase inhibition

Florian Lengauer, Franz Geisslinger, Antje Gabriel, Karin von Schwarzenberg, Angelika M. Vollmar, Karin Bartel (2022), Frontiers in Nutrition, submitted.

ii. Connecting lysosomes and mitochondria – a novel role for lipid metabolism in cancer cell death

Karin Bartel, Helmut Pein, Bastian Popper, Sabine Schmitt, Sudha Janaki-Raman, Almu Schulze, Florian Lengauer, Andread Koeberle, Oliver Werz, Hans Zischka, Rolf Müller, Angelika M. Vollmar, Karin von Schwarzenberg (2019), Cell Communication and Signaling.

7.7.2 Conference contributions

i. Impact of the V-ATPase on glutamine metabolism in cancer – more than just a proton pump?

Florian Lengauer, Karin von Schwarzenberg, Angelika M. Vollmar, Karin Bartel

Virtual V-ATPase summit
June 2021

ii. Implication of myxobacterial V-ATPase inhibitor Archazolid on glutamine metabolism in cancer

Florian Lengauer, Christina Heichler, Martin Strehle, Angelika M. Vollmar, Karin Bartel

HIPS Symposium
May 2022

7.8 Acknowledgements

Mein erster und größter Dank gilt meiner Doktormutter Frau Prof. Dr. Vollmar dafür, dass Sie mir die Möglichkeit gaben nach meiner Masterarbeit auch meine Promotion in ihrem Arbeitskreis anfertigen zu dürfen. Außerdem bedanke ich mich für Ihre hervorragende Betreuung und die wertvollen Ratschläge und Diskussionen. Ich bewundere Sie für Ihre ansteckende Begeisterung für die Wissenschaft sowie für Ihren motivierenden und herzlichen Umgang mit welchem Sie Ihren Arbeitskreis führen.

Besonders möchte ich mich bei Dr. Karin Bartel für die tolle Betreuung bedanken. Danke Karin, für deine Geduld und Ausdauer mich auch während deiner Elternzeit weiterhin zu betreuen. Danke, dass du immer ein offenes Ohr hattest und mir jederzeit mit Rat zur Seite standest. Zusätzlich bedanke ich mich bei Dr. Karin von Schwarzenberg für die Betreuung zu Beginn meiner Promotion. Eine große Wertschätzung gilt auch meinen Kooperationspartnern Prof. Dr. Bracher und Thomas Klaßmüller für die herausragende Zusammenarbeit. Lieber Thomas, ich hätte mir keinen besseren Kooperationspartner als dich wünschen können und bedanke mich für den konstruktiven und interessanten Austausch. Ich wünsche dir für deine Dissertation und Zukunft nur das Beste. Ebenso bedanke ich mich bei Christina Heichler, Márton Nagy, Dr. Peter Wolf und Dr. Martin Strehle von Incyton® GmbH für die tolle Zusammenarbeit. Bedanken möchte ich mich auch ich bei Prof. Dr. Theurich und Martin Kirmaier für die Einführung in die Seahorse Experimente und das Benutzen des Geräts.

Des Weiteren möchte ich mich herzlichst bei Prof. Dr. Zahler für die Beurteilung meiner Arbeit als Zweitgutachter bedanken. Meinem Prüfungskomitee bestehend aus Prof. Dr. Vollmar, Prof. Dr. Zahler, Prof. Dr. Bracher, Prof. Dr. Winter, Prof. Dr. Wagner und Prof. Dr. Frieß danke ich besonders für damit verbundene die Zeit und Mühe meine Arbeit zu bewerten.

Ausdrücklich bedanke ich mich für die tatkräftige Unterstützung bei meinen Projekten bei den technischen Assistentinnen Frau Schnegg, Julia Blenninger, Rita Socher und vor allem Bernadette Grohs, ihr wart mir eine sehr große Hilfe. Für die hervorragenden Leistungen haben sich auch Mark Kudady und Nina Heinrichs, die ich als StudentInnen betreuen durfte, ein großes Dankeschön verdient.

Ein großer Dank geht an den gesamten AK Vollmar für die großartige fachliche und emotionale Unterstützung, insbesondere von meinem Team. Ich erinnere mich auch immer gerne an die Mittags- und Kaffeepausen sowie auch die Aktivitäten abseits der Arbeit. Ganz besonders möchte ich mich bei euch Lucas, Patricia, Conny und vor allem Maibritt und Adrian bedanken. Egal, was es war, ob fachliche Fragen oder einfach nur so mal zum Reden, eure Tür stand stets offen und ich konnte mich immer an euch wenden. In diesem Zusammenhang danke ich auch herzlichst dir Jana, für deinen liebevollen und ständigen Beistand. Für die Zeit mit euch bin ich sehr dankbar.

Bedanken möchte ich mich auch bei meinem privaten Umfeld. Vielen Dank an meine Jungs Luca, Lorenz, Kevin und Marvin für eure mentale Unterstützung ohne die ich diese stressige und schwere Zeit nicht hätte meistern können. Außerdem danke ich der gesamten Fortnite-Crew mit denen ich den Alltag vergessen und unzählige Dubs holen durfte. Darüber hinaus danke ich auch meinem gesamten Football- und Fußball Umfeld, mit denen ich so viele schöne Momente erleben durfte und durch die ich den Stress hinter mir lassen konnte.

Mein letzter und wichtigster Dank geht aber an meine Familie. Danke an dich Maxi (und Josi), du stehst an meiner Seite seit ich denken kann und auf dich kann ich mich immer verlassen. Du hast mich nicht nur aufgebaut wenn es nicht so gut lief, sondern auch mit mir Errungenschaften gefeiert wenn es Höhepunkte gab. Du hilfst mir, wo du nur kannst, bereitest Lösungen für Probleme und hast immer ein offenes Ohr für mich. Du bist für mich nicht nur mein Bruder, sondern auch mein bester Freund. Meinen Eltern gebührt aber das größte Dankeschön. Danke Mama, Danke Papa. Für alles. Ich kann euch gar nicht sagen wie sehr ich euch dankbar bin. Ich durfte bei euch zu Hause in einem Umfeld aufwachsen und leben das ich mir nicht besser hätte wünschen können. Ihr unterstützt mich, wo ihr nur könnt, steht immer hinter mir und macht es überhaupt erst möglich, dass ich diesen außergewöhnlichen Lebensstil von Sport und Promotion leben darf. Ihr seid der Grund dafür, dass ich überhaupt da bin, wo ich jetzt stehe.
Euch ist diese Arbeit gewidmet.